arXiv:0803.1154v1 [hep-ph] 7 Mar 2008

Higgs Working Group Summary Report

Convenors: *S. Dawson*[1], *M. Grazzini*[2], *A. Nikitenko*[3,a], *M. Schumacher*[4]

Contributers: *N. E. Adam*[5], *T. Aziz*[6], *J.R. Andersen*[7], *A. Belyaev*[8], *T Binoth*[9], *S. Catani*[2], *M. Ciccolini*[10], *J.E. Cole*[11], *S. Dawson*[1], *A. Denner*[10], *S. Dittmaier*[12], *A. Djouadi*[8,13,14], *M. Drees*[14], *U. Ellwanger*[13], *C. Englert*[15], *T. Figy*[16], *E. Gabrielli*[17], *D. Giordano*[18], *S. Gleyzer*[19], *R. Godbole*[20], *M. Grazzini*[2], *S. Greder*[3], *V. Halyo*[5], *M. Hashemi*[21], *S. Heinemeyer*[22], *G. Heinrich*[16], *M. Herquet*[23], *S. Hesselbach*[16], *C. Hugonie*[24], *C.B. Jackson*[1], *N. Kauer*[25], *R. Kinnunen*[17], *S.F. King*[8], *S. Lehti*[17], *F. Maltoni*[23], *B. Mele*[26], *P. Mertsch*[27], *M. Moretti*[28], *S. Moretti*[8,29], *M. Mühlleitner*[30], *A.K. Nayak*[6], *A. Nikitenko*[3,a], *C. Oleari*[31], *F. Piccinini*[32], *R. Pittau*[33,34], *J. Rathsman*[35], *I. Rottländer*[14], *C.H. Shepherd-Themistocleous*[11], *M. Schumacher*[4], *J.M. Smillie*[16], *A. Sopczak*[36], *M. Spira*[10], *M. Takahashi*[3], *A. M. Teixeira*[13], *I.R. Tomalin*[11], *M. Vázquez Acosta*[7], *G. Weiglein*[16], *C.D. White*[37] *D. Zeppenfeld*[15]

[1] Brookhaven National Laboratory, Upton, NY 11973, USA
[2] INFN, Sezione di Firenze, Via Sansone 1, I-50019 Sesto Fiorentino, Florence, Italy
[3] Imperial College, London, UK
[a] On leave from ITEP, Moscow
[4] Fachbereich Physik, University of Siegen, Walter-Flex-Straße 3, 57068 Siegen, Germany
[5] Department of Physics, Princeton University, Princeton, NJ 08544, USA
[6]Tata Institute of Fundamental Research, Mumbai,India
[7] CERN, CH 1211 Geneva 23, Switzerland
[8]School of Physics & Astronomy, Southampton University, Southampton SO17 1BJ, UK
[9] School of Physics, The University of Edinburgh, Edinburgh EH9 3JZ, UK
[10] Paul Scherrer Institut, Würenlingen und Villigen, 5232 Villigen, Switzerland
[11] Rutherford Appleton Laboratory, Didcot, OX11 0QX, UK
[12] Max-Planck-Institut für Physik (Werner-Heisenberg-Institut), 80805 München, Germany
[13] Laboratoire de Physique Théorique, Université Paris–Sud, F–91405 Orsay Cedex, France.
[14] Physikalisches Institut, University of Bonn, Nussallee 12, 53115 Bonn, Germany
[15] Institut für Theoretische Physik, Universität Karlsruhe, P.O.Box 6980, 76128 Karlsruhe, Germany
[16] IPPP, University of Durham, Durham DH1 3LE, UK
[17] Helsinki Institute of Physics, Helsinki, Finland
[18]Università degli Studi di Bari, INFN Sezione di Bari, Italy
[19] Department of Physics, Florida State University, Tallahassee, Florida 32306, USA
[20] Center for High Energy Physics, Indian Institute of Science, Bangalore 560 012, India.
[21] Universiteit Antwerpen, G.U.238, Groenenborgerlaan 171, 2020 Antwerpen, Belgium
[22] Instituto de Fisica de Cantabria (CSIC-UC), Santander, Spain
[23] Centre for Particle Physics and Phenomenology (CP3), Université Catholique de Louvain, Louvain-la-Neuve, Belgium
[24] LPTA, Université de Montpellier II, 34095 Montpellier, France.
[25] Institut für Theoretische Physik, Universität Würzburg, D-97074 Würzburg, Germany
[26] University of Rome La Sapienza and INFN, Sezione di Roma, Rome, Italy
[27] Rudolf Peierls Centre for Theoretical Physics, University of Oxford, Oxford OX1 3NP, UK,
[28] Dipartimento di Fisica Università di Ferrara, and INFN, Sezione di Ferrara, Ferrara, Italy
[29]Laboratoire de Physique Théorique, Paris XI, 91405 Orsay, France
[30] LAPTH, 9 Chemin de Bellevue, Annecy-le-Vieux 74951, France
[31] Università di Milano-Bicocca and INFN Sezione di Milano-Bicocca, 20126 Milano, Italy
[32] INFN, Sezione di Pavia, via A. Bassi 6, I 27100, Pavia, Italy
[33] Dipartimento di Fisica Teorica, Università di Torino, and INFN sezione di Torino, via P. Giuria 1,

Torino, Italy
[34] Departamento de Física Teórica y del Cosmos, Centro Andaluz de Física de Partículas Elementales (CAFPE), Universidad de Granada, E-18071, Granada, Spain
[35] High Energy Physics, Uppsala University, Box 535, S-75121 Uppsala, Sweden
[36] Department of Physics, Lancaster University, Lancaster LA1 4YW, UK
[37] NIKHEF, Kruislaan 409, 1098 SJ Amsterdam, The Netherlands

Report of the Working Group on Higgs Bosons for the Workshop "Physics at TeV Colliders", Les Houches, France, 11–29 June, 2007.

Contents

I INTRODUCTION **4**

1. Foreword **4**

II STANDARD MODEL HIGGS BOSONS **8**

2. HNNLO: A Monte Carlo Program for Higgs Boson Production at the LHC **9**

3. Tuned Comparison of QCD Corrections to SM Higgs Boson Production via Vector Boson Fusion at the LHC **11**

4. Loop Induced Interference Effects in Higgs Plus Two Jet Production at the LHC **15**

5. Higgs Boson Production in Association With Multiple Hard Jets **19**

6. Gluon-Induced Z-boson Pair Production at the LHC: Parton Level Results **23**

7. Gluon-Induced Z^*Z^* Background Simulation for Higgs Boson Search **26**

8. The Methods for the Central Rapidity Gap Selection in the Vector Boson Fusion Searches in CMS **28**

9. Production of a Higgs Boson and a Photon in Vector Boson Fusion at the LHC **32**

10. The Z Plus Multi-Jet Background From the Double Parton Interaction in the Vector Boson Fusion $H \to \tau^+\tau^-$ Search **36**

III MSSM HIGGS BOSONS **39**

11. SUSY–QCD Corrections to Squark Loops in Gluon Fusion to Higgs Bosons **40**

12. Higgs Boson Production in Association with b Quarks: SUSY QCD Contributions **43**

13. Charged Higgs Bosons in the MSSM at CMS: Discovery Potential **45**

14. Studies of Spin Effects in Charged Higgs Boson Production with an Iterative Discriminant Analysis at the Tevatron and LHC **50**

IV CP VIOLATING HIGGS BOSONS **56**

15. Jet Assignment Studies in the Search for the Decay $t \to bH^+$, $H^+ \to H_1^0W^+$, $H_1^0 \to b\bar{b}$ in the CPX MSSM Scenario **56**

16. Search for the $t \to bH^+$, $H^+ \to H_1 W$, $H_1 \to b\bar{b}$ channel in CPX MSSM scenario in CMS 61

V NMSSM HIGGS BOSONS 66

17. Les Houches Benchmark Scenarios for the NMSSM 66

18. Parameter Scans in Two Interesting NMSSM Scenarios 71

19. The NMSSM No-Lose Theorem at the LHC: The Scope of the 4τ Channel In Higgs-strahlung and Vector Boson Fusion 76

20. Investigation of the LHC Discovery Potential for Higgs Bosons in the NMSSM 81

21. The $h^0 \to A^0 A^0 \to b\bar{b}\tau^+\tau^-$ Signal in Vector Boson Fusion Production at the LHC 85

Part I

INTRODUCTION

1. FOREWORD [1]

The elucidation of the mechanism of electroweak symmetry breaking is one of the main goals of the LHC physics program. In the Standard Model (SM), mass generation is triggered by the Higgs mechanism, which predicts the existence of one scalar state, the Higgs boson [1, 2]. The Higgs boson couplings to fermions and gauge bosons are a prediction of the model and the only unknown parameter is the Higgs boson mass.

The Minimal Supersymmetric extension of the Standard Model (MSSM) requires the introduction of two Higgs doublets, in order to preserve supersymmetry and give mass to the fermions, and after spontaneous symmetry breaking five Higgs particles remain in the spectrum: two CP-even (h,H), one CP-odd (A) and two charged ($H^\pm$) Higgs bosons. At lowest order the MSSM Higgs sector can be described by two parameters, generally chosen to be m_A, the mass of the pseudoscalar Higgs boson, and $\tan\beta = v_2/v_1$, the ratio of the two vacuum expectation values. The lowest order predictions receive large radiative corrections which must be included when calculating Higgs couplings or masses. At tree level, the lightest neutral Higgs boson has an upper bound of M_Z, which is increased to $m_h \lesssim \mathcal{O}(130 - 140)$ GeV when radiative corrections are included [3].

The search for the Higgs at collider experiments has now being on-going for two decades. The present direct lower limit of the Higgs mass in the SM is 114.4 GeV (at 95% CL) [4], while precision measurements point to a rather light Higgs, $m_h \lesssim 180$ GeV [5, 6]. The Tevatron has a chance to find evidence for a Higgs boson if enough integrated luminosity can be accumulated. At present, the Tevatron is performing well, and it is approaching the sensitivity limit required to exclude the existence of the SM Higgs for $m_h \sim 160$ GeV [7].

If it exists, the Higgs boson will be seen at the LHC, which can provide a measurement of the Higgs mass at the per-mille level and of the Higgs boson couplings at the 5-20 % level [8]. These tasks, however, require accurate theoretical predictions for both signal and background cross sections and distributions, and this is true in particular for an accurate determination of the properties of the discovered particle, such as spin, CP, and couplings.

[1] Contributed by: S. Dawson and M. Grazzini

In the following we review the status of theoretical predictions for both signal and background at the LHC, with emphasis on recent developments for the Standard Model Higgs boson.

1.1 Gluon-Gluon Fusion

The gluon fusion mechanism, mediated by a (heavy)-quark loop, provides the dominant production mechanism of Higgs bosons at the LHC in the full mass range.

QCD corrections to this process at next-to-leading order (NLO) have been known for some time [9–11] and their effect increases the leading order (LO) cross section by about 80–100%. This calculation is very well approximated by the large-m_{top} limit. When the exact Born cross section (with full dependence on the masses of top and bottom quarks) is used to normalize the result, the difference between the exact and the approximated NLO cross sections ranges from 1 to 4% when $m_h < 200$ GeV. In recent years, the next-to-next-to-leading order (NNLO) corrections have been computed in this limit [12–17], leading to an additional increase of the cross section of about $10 - 15\%$. Soft-gluon resummation leads to a further increase of about 6% [18]. The latter result is nicely confirmed by the more recent evaluation of the leading soft contributions at N^{3}LO [19–21]. Two loop EW effects are also known [22–24].

In the MSSM, for large $\tan\beta$, the contribution from bottom quark loops becomes important and the large-m_{top} limit is not applicable. The full SUSY-QCD corrections are known in the limit of heavy squark and gluino masses at NLO [25–27]. Recently, the exact contribution of squark loops has been evaluated at NLO [28] and is discussed in Sect. 11. The massive virtual corrections to the squark loops are given in Ref. [29, 30].

The higher order calculations mentioned above are certainly important but they refer to total cross sections, i.e., the experimental cuts are largely ignored. The impact of higher order corrections on the rate and the shape of the corresponding distributions may be strongly dependent on the choice of cuts. In the case in which one [31] or two [32] jets are tagged at large p_T the NLO corrections for Higgs production from gluon fusion are known and implemented in parton level Monte Carlo programs. These predictions are obtained in the large m_{top} limit, which is a good approximation for small transverse momentum of the accompanying jet. For Higgs plus one jet production, there is a rather flat dependence of the K factor on p_T and rapidity for moderate p_T and y. In the MSSM, the Higgs plus 1 jet rate is known at lowest order only [33, 34]. The Higgs plus 2 jet process from gluon fusion is a background for vector boson fusion, as discussed below. Interference effects in the Higgs plus 2 jet channel are discussed in Sect. 4.

The NNLO inclusive cross section when a jet veto is applied [35] has been known for some time. The first NNLO calculation that fully takes into account experimental cuts was reported in Ref. [36], in the case of the decay mode $h \to \gamma\gamma$ which is implemented in the FEHIP Monte Carlo program. In Ref. [37] the calculation was extended to the decay mode $h \to W^+W^- \to l^+l^-\nu\overline{\nu}$. Recently, an independent NNLO calculation has been performed [38, 39], including all the relevant decay modes of the Higgs boson: $h \to \gamma\gamma$, $h \to W^+W^- \to l^+l^-\nu\overline{\nu}$ and $h \to ZZ \to 4$ leptons. Such a calculation is implemented in a Monte Carlo program and is documented in this report in Sect. 2.

Among the possible differential distributions, an important role is played by the transverse momentum (p_T) spectrum of the Higgs boson [40]. When $p_T \sim m_h$ the standard fixed order expansion is applicable. When $p_T \ll m_h$, large logarithmic contributions appear that may invalidate the customary fixed order expansion. The resummation of such contributions has been performed at different levels of theoretical accuracy [41–46]. In Refs. [44–46] the resummed result up to next-to-next-to-leading logarithmic accuracy is matched to the fixed order NLO result [31, 47, 48] valid at large transverse momenta. It is important to note that transverse-momentum resummation is approximately performed by standard Monte Carlo event generators. A comparison of results obtained with different tools was presented in Ref. [49].

For Higgs boson masses below about 140 GeV the dominant decay mode $h \to b\bar{b}$ is swamped by

the huge QCD background and the Higgs boson can be found by looking at the rare $h \to \gamma\gamma$ decay mode. The $\gamma\gamma$ background can be measured precisely from the data using sideband interpolation, but accurate theoretical predictions are useful to estimate the expected accuracies and to better understand detector performances. The $h \to \gamma\gamma$ decay width is known including full two loop QCD and EW effects [50–52]. The NNLO QCD effects are known in the large-m_{top} limit [53]. The $\gamma\gamma$ irreducible background has been computed up to NLO including the fragmentation effects [54]. The $gg \to \gamma\gamma$ contribution, which is formally NNLO, is enhanced by the large gluon luminosity and is known up to N^{3}LO (i.e. $\mathcal{O}(\alpha_s^3)$) [55].

For Higgs masses between 140 and 180 GeV the $W^+W^- \to l^+l^-\nu\overline{\nu}$ decay mode is the most important. Despite the absence of a mass peak, there are strong angular correlations between the charged leptons [56]. To suppress the $t\bar{t}$ background, a jet veto has to be applied to cut events with high-p_T b-jets from the decay of the top quark. The impact of higher-order corrections on the Higgs signal is strongly reduced by the selection cuts [37, 39, 57]. This channel appears to be one of the most promising for an early discovery [58], but at the same time it is the most challenging as far as the background is concerned. Because of the missing energy, the Higgs mass cannot be directly reconstructed, and a straightforward background extrapolation from sidebands is not possible. The background has to be extrapolated from regions where the signal is absent and this requires a precise knowledge of the background distributions. The W^+W^- irreducible background is known up to NLO [59, 60] including spin correlations, and the effects of multiple soft-gluon emissions has been included up to NLL [61]. Spin correlations in the W decay are crucial for a correct prediction of angular distributions and are now implemented in the MC@NLO event generator [62, 63]. The potentially large $gg \to W^+W^-$ contribution, formally NNLO, has also been computed [64, 65]. The $t\bar{t}$ background, including the effect of spin correlations [66], is known up to NLO and is also included in MC@NLO. A complete calculation including finite width effects (and thus W^+W^-bb, Wtb) is available at LO only [67].

When the Higgs mass is larger than about 180 GeV, the decay $h \to ZZ \to 4$ leptons becomes dominant. This channel is much easier to observe than the W^+W^- channel because the invariant mass of the leptons can be reconstructed and thus the background can be measured from the data. Accurate predictions become important when the nature of the Higgs particles is studied. The irreducible ZZ background is known up to NLO including spin correlations [59, 60]. The impact of soft-gluon effects on signal and background has been studied recently [68]. The calculation of the $gg \to ZZ$ contribution is accounted for in this report in Sects. 6. and 7. We finally note that the full QCD+EW corrections to the decay modes $h \to W^+W^-(ZZ) \to 4$ leptons have been recently computed [69, 70].

1.2 Vector-Boson Fusion

The vector boson fusion (VBF) process plays an important role for a wide range of Higgs masses. The VBF cross section is typically one order of magnitude smaller than the one from gluon fusion, and it becomes competitive with the latter for very large Higgs masses.

VBF occurs through the scattering of two valence quarks that exchange a W or a Z boson. Since valence quark distributions in the proton are peaked at relatively large Bjorken x ($x \sim 0.1 - 0.2$), the scattered quarks emerge with very large longitudinal momentum and transverse momentum of the order of a fraction of the boson mass. As a consequence, the typical signature of a VBF event is given by two hard jets with a large rapidity interval between them, and since the exchanged boson is colourless, there is no hadronic activity between them. Although this channel has a smaller cross section with respect to gluon fusion, it is very attractive both for discovery and for the measurement of the Higgs couplings.

The NLO QCD corrections to the total rate were computed some time ago and found to be of the order of $5-10\%$ [71]. In recent years, these corrections have been implemented for distributions [72–74]. Recently, the full EW+QCD corrections to this process have been computed [75, 76]. A comparison of the different calculations is presented in this report in Sect. 3.

The h+2 jets final state can be produced also by gluon-gluon fusion. This signature, although

part of the inclusive Higgs boson signal, represents a background when trying to isolate the hWW and hZZ couplings through VBF. The gluon fusion contribution is known at LO with full top mass dependence [77]. The kinematical distributions of the tagging jets show remarkable differences in the two production mechanisms. The $\Delta\phi$ distribution of the tagging jets is rather flat for the VBF signal. By contrast, the loop induced hgg coupling leads to a pronounced dip at $\Delta\phi = 90^o$. Another significant difference is found in the rapidity distribution of the third hardest jet with respect to the rapidity average of the other two. The VBF signal has a dip in the central region, where the gluon fusion background is peaked. As such, a cut on jets with $p_T > p_T^{\rm veto}$ in the central rapidity region (central jet veto) enhances the relevance of the VBF signal. Recently, NLO QCD corrections to the $h + 2$ jets process in the large m_{top}-limit have been computed [32], and also parton shower effects on the relevant distributions have been evaluated [78]. These studies show that the discriminating power of previous LO results is not significantly changed. We note, however, that when the $p_T^{\rm veto}$ is much smaller than the Higgs boson mass the coefficients of the perturbative series are enhanced by large logarithmic contributions that may invalidate the fixed order expansion. The latter point deserves more detailed investigation. An experimental study of central jet veto efficiencies is presented in this report in Sect. 8.

The most important decay channels of the Higgs boson in VBF are $h \to \tau^+\tau^-$ and $h \to W^+W^- \to l^+l^-\nu\overline{\nu}$. The $h \to \tau^+\tau^-$ decay mode provides an important discovery channel in the MSSM. The $\tau^+\tau^-$ invariant mass can be reconstructed at the LHC with an accuracy of a few GeV. This is possible because VBF typically produces Higgs bosons with large transverse momentum. As a consequence, a sideband analysis can in principle be used to measure the background from the data. The most important backgrounds are QCD Zjj and EW Zjj from VBF. Both are known up to NLO [79, 80].

The $h \to W^+W^- \to l^+l^-\nu\overline{\nu}$ decay mode is the most challenging, because, as for gluon fusion, it does not allow a direct Higgs mass reconstruction. The irreducible W^+W^- background is known up to NLO [81]. The other important background is $t\bar{t} + \text{jets}$, and has the largest uncertainty. Recently, the NLO corrections to $t\bar{t}+$ jet have been computed [82]. It will be essential to include the decay of the top quark with full spin correlations. In addition, finite width effects could be relevant.

1.3 Associated Production With a $b\bar{b}$ Pair

In the Standard Model, Higgs production in association with b quarks is never important, since this rate is suppressed by m_b/v. This channel is important in MSSM scenarios at large $\tan\beta$, since the Higgs coupling to bottom quarks is enhanced in this regime. For $\tan\beta \gtrsim 7$, Higgs production in association with a b quark is the dominant production mechanism at the LHC. The cross section for b- Higgs production can be computed using two different formalisms, which represent different orderings of perturbation theory. In the four-flavour scheme the cross section starts with $gg \to b\bar{b}h$ at LO. The cross section for the associated production of the Higgs boson with zero, one or two high-transverse momentum b-jets is known up NLO [83–86]. In the five flavour scheme, the LO process is $b\bar{b} \to h$ and bottom quark parton distributions are introduced to sum the potentially large logarithms, $\log(m_h/m_b)$. The inclusive cross section has been computed up to NNLO [87], and the cross section for the associated production with one high-p_T b jet is known at NLO [88]. In recent years, a detailed comparison between the results of the two approaches has been performed with the conclusion that the two approaches lead to similar results. For a discussion see Ref. [89, 90]. In addition, the electroweak corrections to $b\bar{b} \to h$ [91], the dominant top quark contributions to the NNLO rate for the exclusive $b\bar{b}h$ process [92] and the SUSY QCD corrections to $b\bar{b} \to h$, $bg \to bh$ are known [93]. The effects of SUSY-QCD on b-Higgs production is discussed in Sect. 12.

1.4 Associated Production With a $t\bar{t}$ Pair

The $ht\bar{t}$ channel offers the possibility of a clean measurement of the top quark Yukawa coupling. The NLO corrections to the $ht\bar{t}$ signal were independently computed by two groups [94–97], and found to increase the signal cross section by $20 - 40\%$. The $ht\bar{t}$ channel was initially thought to be an important

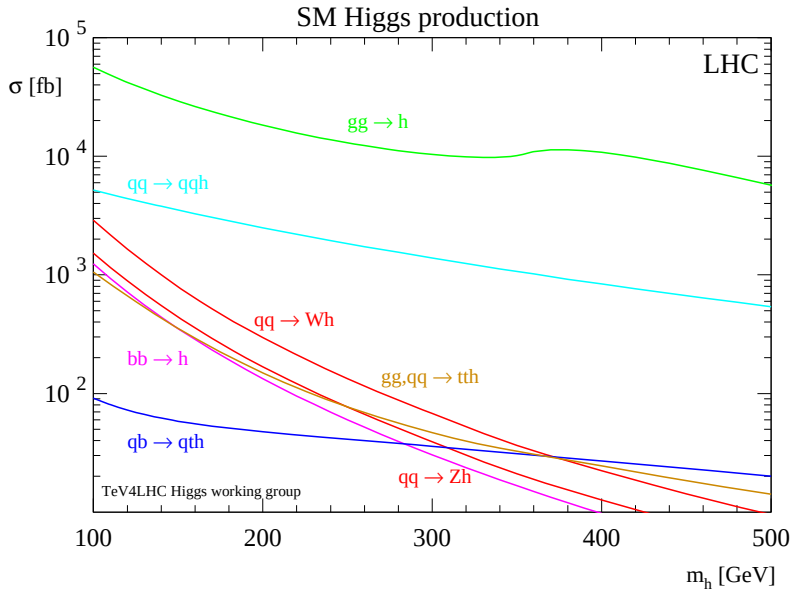

Fig. 1: Total cross sections for Higgs production at the LHC. The gluon fusion result is NNLO QCD with soft gluon resummation effects included at NNLL and uses MRST2002 PDFs with renormalization/factorization scales equal to m_h. The vector boson fusion curve is shown at NLO QCD with CTEQ6M PDFs and renormalization/factorization scales equal to m_h. The Vh results ($V = W, Z$) include NNLO QCD corrections and NLO EW corrections and use MRST2002 PDFs with the renormalization /factorization scales equal to the $m_h - M_V$ invariant mass. The $b\bar{b} \to h$ result is NNLO QCD, with MRST2002 PDFs, renormalization scale equal to m_h and factorization scale equal to $m_h/4$. The results for $t\bar{t}h$ production are NLO QCD, use CTEQ6M PDFs and set the renormalization/factorization scale to $m_t + m_h/2$ [100].

discovery channel in the low Higgs mass region, looking at the $h \to b\bar{b}$ decay mode and triggering on the leptonic decay of one of the top. The main backgrounds are $t\bar{t}b\bar{b}$ and $t\bar{t}bjj$. Recently, more detailed investigations based on a more careful background evaluation and full detector simulation lead to a more pessimistic view on the possibility of observing the Higgs signal in this channel [98]. This channel could be important for measuring the top quark Yukawa coupling [8, 99].

1.5 Associated production with a W or a Z boson

This channel is essential for the Higgs search at the Tevatron for Higgs masses below 130 GeV. The leptonic decay of the vector boson provides the necessary background rejection to allow for looking at the $h \to b\bar{b}$ decay mode. The signal cross section is known up to NNLO in QCD, the corrections being about $+30\%$ [101, 102]. These corrections are identical to those of Drell-Yan, but in the case of Zh an additional contribution from the gg initial state must be included [103]. Full EW corrections are known and decrease the cross section by $5 - 10\%$ [104].

1.6 Conclusions

The important Higgs production channels are known at NLO QCD and in a few cases to NNLO and progress is being made in implementing these results in Monte Carlo programs. A summary of the total rates for the most important Higgs production channels is shown in Fig. 1 [100].

Part II

STANDARD MODEL HIGGS BOSONS

2. HNNLO: A MONTE CARLO PROGRAM FOR HIGGS BOSON PRODUCTION AT THE LHC [2]

2.1 Introduction

Gluon-gluon fusion is the main production channel of the Standard Model Higgs boson at the LHC. At leading order (LO) in QCD perturbation theory, the cross section is proportional to $\alpha_{\rm S}^2$, $\alpha_{\rm S}$ being the QCD coupling. The QCD radiative corrections to the total cross section are known at the next-to-leading order (NLO) [9–11] and at the next-to-next-to-leading order (NNLO) [12–17]. The effects of a jet veto on the total cross section has been studied up to NNLO [35]. We recall that all the results at NNLO have been obtained by using the large-M_t approximation, M_t being the mass of the top quark.

These NNLO calculations are certainly important but they refer to situations where the experimental cuts are either ignored (as in the case of the total cross section) or taken into account only in simplified cases (as in the case of the jet vetoed cross section). The impact of higher-order corrections may be strongly dependent on the details of the applied cuts and also the shape of the distributions is typically affected by these details.

The first NNLO calculation that fully takes into account experimental cuts was reported in Ref. [36], in the case of the decay mode $H \to \gamma\gamma$. In Ref. [37] the calculation is extended to the decay mode $H \to WW \to l\nu l\nu$.

In Ref. [38] we have presented an independent NNLO calculation of the Higgs production cross section. The method is completely different from that used in Refs. [36, 37]. Our calculation is implemented in a fully-exclusive parton level event generator. This feature makes it particularly suitable for practical applications to the computation of distributions in the form of bin histograms. Our numerical program can be downloaded from [105]. The decay modes that are currently implemented are $H \to \gamma\gamma$, $H \to WW \to l\nu l\nu$ and $H \to ZZ \to 4$ leptons [39].

In the following we present a brief selection of results that can be obtained by our program. We consider Higgs boson production at the LHC and use the MRST2004 parton distributions [106], with parton densities and $\alpha_{\rm S}$ evaluated at each corresponding order (i.e., we use $(n+1)$-loop $\alpha_{\rm S}$ at N^{n}LO, with $n = 0, 1, 2$). The renormalization and factorization scales are fixed to the value $\mu_R = \mu_F = M_H$, where M_H is the mass of the Higgs boson.

2.2 Results For the Decay Mode $H \to \gamma\gamma$

We consider the production of a Higgs boson of mass $M_H = 125$ GeV in the $H \to \gamma\gamma$ decay mode and follow Ref. [98] to apply cuts on the photons. For each event, we classify the photon transverse momenta according to their minimum and maximum value, $p_{T\rm min}$ and $p_{T\rm max}$. The photons are required to be in the central rapidity region, $|\eta| < 2.5$, with $p_{T\rm min} > 35$ GeV and $p_{T\rm max} > 40$ GeV. We also require the photons to be isolated: the hadronic (partonic) transverse energy in a cone of radius $R = 0.3$ along the photon direction has to be smaller than 6 GeV. By applying these cuts the impact of the NNLO corrections on the NLO total cross section is reduced from 19% to 11%.

In Fig. 2 we plot the distributions in $p_{T\rm min}$ and $p_{T\rm max}$ of the signal process $gg \to H \to \gamma\gamma$. We note that the shape of these distributions sizeably differs when going from LO to NLO and to NNLO. The origin of these perturbative instabilities is well known [107]. Since the LO spectra are kinematically bounded by $p_T \leq M_H/2$, each higher-order perturbative contribution produces (integrable) logarithmic singularities in the vicinity of that boundary. More detailed studies are necessary to assess the theoretical

[2] Contributed by: S. Catani and M. Grazzini

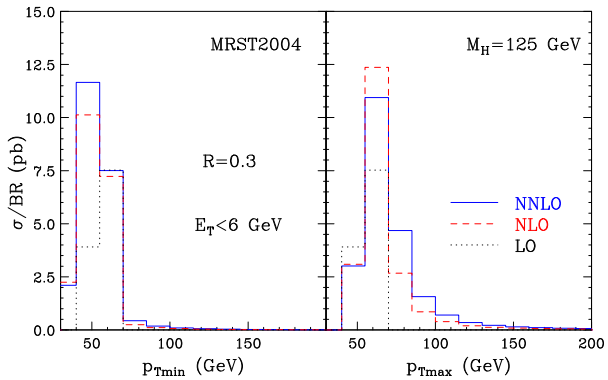

Fig. 2: Distributions in $p_{T\min}$ and $p_{T\max}$ for the diphoton signal at the LHC. The cross section is divided by the branching ratio in two photons.

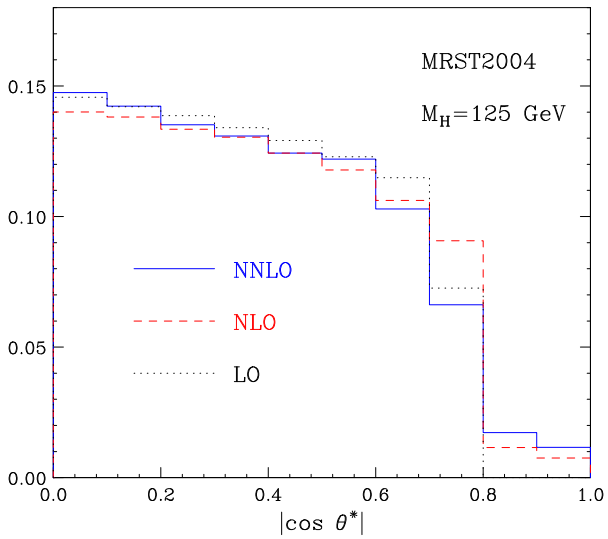

Fig. 3: Normalized distribution in the variable $\cos\theta^*$.

uncertainties of these fixed-order results and the relevance of all-order resummed calculations.

In Fig. 3 we consider the (normalized) distribution in the variable $\cos\theta^*$, where θ^* is the polar angle of one of the photons in the rest frame of the Higgs boson [3]. At small values of $\cos\theta^*$ the distribution is quite stable with respect to higher order QCD corrections. We also note that the LO distribution vanishes beyond the value $\cos\theta^*_{\max} < 1$. The upper bound $\cos\theta^*_{\max}$ is due to the fact that the photons are required to have a minimum p_T of 35 GeV. As in the case of Fig. 2, in the vicinity of this LO kinematical boundary there is an instability of the perturbative results beyond LO.

2.3 Results for the Decay Mode $H \to l\nu l\nu$

We now consider the production of a Higgs boson with mass $M_H = 165$ GeV in the decay mode $H \to l\nu l\nu$. We apply a set of preselection cuts taken from the study of Ref. [58]. The charged leptons have p_T larger than 20 GeV, and $|\eta| < 2$. The missing p_T is larger than 20 GeV and the invariant mass of the charged leptons is smaller than 80 GeV. Finally, the azimuthal separation of the charged leptons in the

[3] We thank Suzanne Gascon and Markus Schumacher for suggesting the use of this variable.

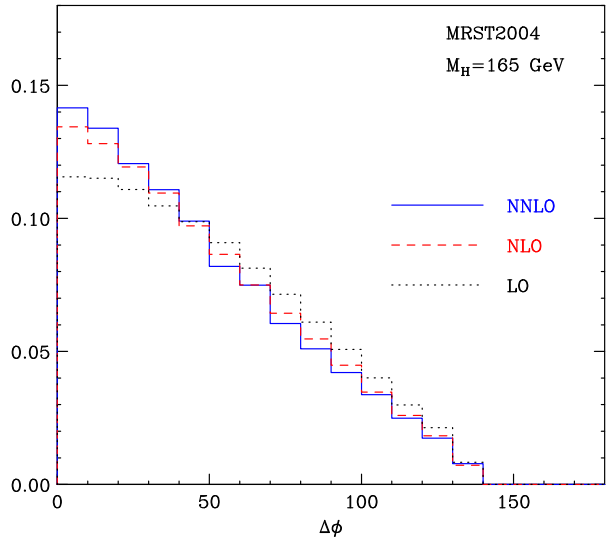

Fig. 4: Normalized $\Delta\phi$ distribution at LO, NLO, NNLO.

transverse plane ($\Delta\phi$) is smaller than 135°. By applying these cuts the impact of the NNLO corrections on the NLO result does not change and is of about 20%.

In Fig.4 we plot the $\Delta\phi$ distribution at LO, NLO and NNLO. As is well known [56], the charged leptons from the Higgs boson signal tend to be close in angle, and thus the distribution is peaked at small $\Delta\phi$. We notice that the effect of the QCD corrections is to increase the steepness of the distribution, from LO to NLO and from NLO to NNLO.

2.4 Conclusions

We have illustrated a calculation of the Higgs boson production cross section at the LHC up to NNLO in QCD perturbation theory. The calculation is implemented in the numerical program `HNNLO`, which at present includes the decay modes $H \to \gamma\gamma$ and $H \to WW \to l\nu l\nu$ and $H \to ZZ \to 4$ leptons. The program allows the user to apply arbitrary cuts on the momenta of the partons and leptons (photons) produced in the final state, and to obtain the required distributions in the form of bin histograms. We have presented a brief selection of numerical results that can be obtained by our program. More detailed results for the decay modes $H \to WW$ and $H \to ZZ$ can be found in Ref. [39]. The fortran code `HNNLO` can be downloaded from [105].

3. TUNED COMPARISON OF QCD CORRECTIONS TO SM HIGGS-BOSON PRODUCTION VIA VECTOR BOSON FUSION AT THE LHC [4]

3.1 Introduction

The electroweak (EW) production of a Standard Model Higgs boson in association with two hard jets in the forward and backward regions of the detector—frequently quoted as the "vector-boson fusion" (VBF) channel—is a cornerstone in the Higgs search both in the ATLAS [108] and CMS [109] experiments at the LHC. Higgs production in the VBF channel also plays an important role in the determination of Higgs couplings at the LHC (see e.g. Ref. [8]). Even bounds on non-standard couplings between Higgs and EW gauge bosons can be imposed from precision studies in this channel [110].

Higgs+2jets production in pp collisions proceeds through two different channels. The first channel corresponds to a pure EW process where the Higgs boson couples to a weak boson. It comprises the

[4]Contributed by: M. Ciccolini, A. Denner, S. Dittmaier, C. Englert, T. Figy, C. Oleari, M. Spira, and D. Zeppenfeld

scattering of two (anti-)quarks mediated by t- and u-channel W- or Z-boson exchange, with the Higgs boson radiated off the weak-boson propagator. It also involves Higgs-boson radiation off a W- or Z-boson produced in s-channel quark–antiquark annihilation (Higgs-strahlung process), with the weak boson decaying hadronically. The second channel proceeds mainly through strong interactions, the Higgs boson being radiated off a heavy-quark loop that couples to any parton of the incoming hadrons via gluons [32, 77].

In the weak-boson-mediated processes, the two scattered quarks are usually visible as two hard forward jets, in contrast to other jet production mechanisms, offering a good background suppression (transverse-momentum and rapidity cuts on jets, jet rapidity gap, central-jet veto, etc.). Applying appropriate event selection criteria (see e.g. Refs. [78, 111–114] and references in Refs. [2, 115]) it is possible to sufficiently suppress background and to enhance the VBF channel over the hadronic Higgs+2jets production mechanism.

In order to match the required precision for theoretical predictions at the LHC, QCD and EW corrections are needed. When VBF cuts are imposed, the cross section can be approximated by the contribution of squared t- and u-channel diagrams only, which reduces the QCD corrections to vertex corrections to the weak-boson–quark coupling. Explicit next-to-leading-order (NLO) QCD calculations in this approximation exist since more than a decade [71, 115], while corrections to distributions have been calculated in the last few years [72–74]. Recently, the full NLO EW and QCD corrections to this process have become available [75, 76]. This calculation includes, for the first time, the complete set of EW and QCD diagrams, namely the t-, u-, and s-channel contributions, as well as all interferences.

In this short note we compare the NLO QCD corrected cross-section results obtained by three different calculations using a common set of input parameters and a uniformly tuned setup. We also present, in order to better understand the different approximations, the full NLO QCD and EW corrected results as obtained in Refs. [75, 76].

In the next section, the different approaches that we compare are briefly summarized. The precise setup is described in Section 3.3, and Section 3.4 contains the numerical results.

3.2 Different Approaches and Codes

The following collaborations have contributed to the tuned comparison of NLO QCD corrected results for Higgs-boson production via weak-boson fusion at the LHC:

- `CDD`: References [75, 76] present a detailed description of the calculation of the complete NLO EW and QCD corrections to Higgs-boson production in the VBF channel at the LHC. The NLO $\mathcal{O}(\alpha_s)$ corrections include the complete set of QCD diagrams, namely the t-, u-, and s-channel contributions, as well as all interferences. The integrated cross section (with and without dedicated VBF selection cuts) was calculated, as well as different Higgs-boson and tagging-jet observables. In the EW corrections, real corrections induced by photons in the initial state and QED corrections implicitly contained in the DGLAP evolution of PDFs were also taken into account. All EW contributions have been switched off for this comparison.
- `VBFNLO` [116] is a NLO parton-level Monte Carlo program which implements one-loop QCD corrections for a collection of relevant VBF processes, of which Higgs-boson production, in the narrow resonance approximation, is the simplest example. Higgs-boson production in weak-boson fusion is implemented following the results of Ref. [72]. `VBFNLO` generates an isotropic Higgs-boson decay into two massless "leptons" (which represent $\tau^+\tau^-$ or $\gamma\gamma$ or $b\bar{b}$ final states), and imposes a cut on the invariant mass of the Higgs boson. This feature has been disabled during this comparison, and only a non-decaying Higgs boson has been considered. We have employed `VBFNLO-v.1.0`, and included only four flavours of the external quarks.
- `VV2H` [117] calculates the production cross section of Higgs bosons via $\mathrm{WW/ZZ} \to \mathrm{h, H}$ at hadron colliders at NLO QCD according to the formulae presented in Refs. [71, 115]. Interference

effects between W- and Z-boson fusion are neglected. The program allows to calculate the total production cross section for the scalar Higgs bosons of the SM and MSSM. For the present study we employed the VV2H version dated July 23, 2007, which was modified in order to switch off the contributions from b quarks in the final and/or initial states.

3.3 Common Setup for the Calculation

3.31 Input parameters and scheme definitions

We choose the following set of input parameters [118], which have also been used in Refs. [75, 76]:

$$\begin{aligned}
G_\mu &= 1.16637 \times 10^{-5}\,\mathrm{GeV}^{-2}, & \alpha(0) &= 1/137.03599911, & & \\
M_\mathrm{W}^\mathrm{LEP} &= 80.425\,\mathrm{GeV}, & \Gamma_\mathrm{W}^\mathrm{LEP} &= 2.124\,\mathrm{GeV}, & & \\
M_\mathrm{Z}^\mathrm{LEP} &= 91.1876\,\mathrm{GeV}, & \Gamma_\mathrm{Z}^\mathrm{LEP} &= 2.4952\,\mathrm{GeV}, & & \\
m_\mathrm{e} &= 0.51099892\,\mathrm{MeV}, & m_\mu &= 105.658369\,\mathrm{MeV}, & m_\tau &= 1.77699\,\mathrm{GeV}, \\
m_u &= 66\,\mathrm{MeV}, & m_c &= 1.2\,\mathrm{GeV}, & m_t &= 174.3\,\mathrm{GeV}, \\
m_d &= 66\,\mathrm{MeV}, & m_s &= 150\,\mathrm{MeV}, & m_b &= 4.3\,\mathrm{GeV}.
\end{aligned} \tag{1}$$

CDD uses the complex-mass scheme [119]. This requires a fixed width in the W- and Z-boson propagators in contrast to the approach used at LEP to fit the W and Z resonances, where running widths are taken. Following Ref. [120] to convert the "on-shell" values of M_V^LEP and Γ_V^LEP ($V = \mathrm{W}, \mathrm{Z}$) to the "pole values" denoted by M_V and Γ_V, leads to

$$\begin{aligned}
M_\mathrm{W} &= 80.397\ldots\ \mathrm{GeV}, & \Gamma_\mathrm{W} &= 2.123\ldots\ \mathrm{GeV}, \\
M_\mathrm{Z} &= 91.1535\ldots\ \mathrm{GeV}, & \Gamma_\mathrm{Z} &= 2.4943\ldots\ \mathrm{GeV}.
\end{aligned} \tag{2}$$

In VV2H and VBFNLO the W- and Z-boson masses are fixed according to Eq. (2) and the vector-bosons widths are set to zero.

The masses of the light quarks are adjusted to reproduce the hadronic contribution to the photonic vacuum polarization of Ref. [121]. Since quark mixing effects are suppressed we neglect quark mixing and use a unit CKM matrix. All quark masses are set to zero in VBFNLO. We use the G_μ scheme, i.e. we derive the electromagnetic coupling constant from the Fermi constant according to

$$\alpha_{G_\mu} = \sqrt{2} G_\mu M_\mathrm{W}^2 (1 - M_\mathrm{W}^2/M_\mathrm{Z}^2)/\pi. \tag{3}$$

CTEQ6 parton distributions [122] are used. Processes with external bottom quarks are not included in this comparison. As discussed in Section 3.4 of Ref. [76] these contribute at the level of a few per cent. We use M_W as factorization scale both for QCD and QED collinear contributions. For the calculation of the strong coupling constant we employ M_W as the default renormalization scale, include 5 flavours in the two-loop running of α_s, and fix $\alpha_\mathrm{s}(M_\mathrm{Z}) = 0.118$, consistent with the CTEQ6M distribution.

3.32 Phase-space cuts and event selection

We employ the same jet definition parameters, phase-space and event selection cuts as described in Refs. [73, 75, 76]. Jet reconstruction from final-state partons is performed using the k_T-algorithm [123] as described in Ref. [124]. Jets are reconstructed from partons of pseudorapidity $|\eta| < 5$ using a jet resolution parameter $D = 0.8$. In the EW corrections, real photons are recombined with jets according to the same algorithm. Thus, in real photon radiation events, final states may consist of jets plus a real identifiable photon, or of jets only.

We study total cross sections and cross sections for the set of experimental "VBF cuts". These cuts significantly suppress backgrounds to VBF processes, enhancing the signal-to-background ratio. We require at least two hard jets with

$$p_\mathrm{Tj} > 20\,\mathrm{GeV}, \qquad |y_\mathrm{j}| < 4.5, \tag{4}$$

$M_{\rm H}$ [GeV]	120	150	170	200	400	700
$\sigma_{\rm LO}^{\rm CDD}$ [fb]	4226.3(6)	3357.8(5)	2910.7(4)	2381.6(3)	817.6(1)	257.49(4)
$\sigma_{\rm LO}^{\rm VBFNLO}$ [fb]	4227.1(1)	3358.0(1)	2910.8(1)	2380.79(8)	817.48(3)	257.444(9)
$\sigma_{\rm LO}^{\rm VV2H}$ [fb]	4226.2(4)	3357.3(3)	2910.2(3)	2380.4(2)	817.33(8)	257.40(3)
$\sigma_{\rm LO}^{\rm QCD+EW}$ [fb]	5404.8(9)	3933.7(6)	3290.4(5)	2597.9(4)	834.5(1)	259.26(4)
$\sigma_{\rm NLO}^{\rm CDD}$ [fb]	4424(4)	3520(3)	3052(3)	2505(2)	858.4(7)	268.2(2)
$\sigma_{\rm NLO}^{\rm VBFNLO}$ [fb]	4414.8(2)	3519.8(2)	3055.9(2)	2503.3(1)	858.73(4)	268.02(1)
$\sigma_{\rm NLO}^{\rm VV2H}$ [fb]	4415(1)	3519.7(8)	3055.8(7)	2503.4(6)	858.8(2)	268.03(6)
$\sigma_{\rm NLO}^{\rm full\ QCD}$ [fb]	6030(4)	4313(3)	3579(2)	2802(2)	878.9(6)	269.9(2)
$\sigma_{\rm NLO}^{\rm QCD+EW}$ [fb]	5694(4)	4063(3)	3400(3)	2666(2)	839.0(7)	285.9(3)

Table 1: Total integrated cross section for $\rm pp \to H{+}2jets{+}X$ in LO and NLO without any cuts, calculated by CDD, $\sigma_{\rm LO/NLO}^{\rm CDD}$, with VV2H, $\sigma_{\rm LO/NLO}^{\rm VV2H}$, and with VBFNLO, $\sigma_{\rm LO/NLO}^{\rm VBFNLO}$, for the setup defined in the text.

where $p_{\rm Tj}$ is the transverse momentum of the jet and $y_{\rm j}$ its rapidity. Two tagging jets $\rm j_1$ and $\rm j_2$ are defined as the two jets passing the cuts (4) with highest $p_{\rm T}$ such that $p_{\rm T j_1} > p_{\rm T j_2}$. Furthermore, we require that the tagging jets have a large rapidity separation and reside in opposite detector hemispheres:

$$\Delta y_{\rm jj} \equiv |y_{\rm j_1} - y_{\rm j_2}| > 4, \qquad y_{\rm j_1} \cdot y_{\rm j_2} < 0. \tag{5}$$

3.4 Numerical Results

In this section we present, for a range of Higgs-boson masses, LO and NLO QCD corrected results obtained by CDD, $\sigma_{\rm LO/NLO}^{\rm CDD}$, with VV2H, $\sigma_{\rm LO/NLO}^{\rm VV2H}$, and with VBFNLO, $\sigma_{\rm LO/NLO}^{\rm VBFNLO}$. These results were calculated approximating the cross section by the contribution of squared t- and u-channel diagrams only, without any interferences. We also present the QCD corrected results, including all diagrams and interference contributions, $\sigma_{\rm LO/NLO}^{\rm full\ QCD}$, together with the results including both QCD and EW corrections, $\sigma_{\rm LO/NLO}^{\rm QCD+EW}$, as obtained by CDD.

Table 1 contains results for the total integrated cross section without any cuts. The small difference between the results obtained by VV2H and VBFNLO is due to the different treatment of vector-boson widths. We observe that the approximate LO cross sections agree within 5×10^{-4}, and the NLO corrected results within 2×10^{-3}, a difference which is of the order of the statistical error. The complete predictions $\sigma^{\rm QCD+EW}$ differ from the results of VV2H and VBFNLO by up to 30% for low Higgs-boson masses and by a few per cent for high Higgs-boson masses. The bulk of this big difference for small values of $M_{\rm H}$ is due to the s-channel contributions, which are only considered by CDD.

Table 2 shows results for the integrated cross section after imposing VBF selection cuts. We observe that the approximate LO cross sections agree within 8×10^{-4}, and the NLO corrected results within 1×10^{-3}, a difference which is of the order of the statistical error. The difference between the complete predictions $\sigma^{\rm QCD+EW}$ and the results of VBFNLO is half a per mille or less in LO, and 6–8%, the size of the EW corrections, in NLO. This shows that, in this configuration, s-channel and interference contributions can be safely neglected, but EW corrections are as large as QCD corrections.

3.5 Conclusions

We have presented results for NLO cross sections of Standard Model Higgs-boson production via weak-boson fusion at the LHC. A tuned comparison of QCD corrected results obtained by three different calculations has been performed. Taking into account only t- and u-channel diagrams we found good agreement. We have also presented full NLO EW and QCD corrected results to gain some insight into the nature of this approximation. We found agreement between the approximate and full $\mathcal{O}(\alpha_s)$ results when VBF cuts are applied. On the other hand, for the total integrated cross section, there is a

$M_{\rm H}$ [GeV]	120	150	170	200	400	700
$\sigma_{\rm LO}^{\rm CDD}$ [fb]	1686.2(3)	1433.4(2)	1290.3(2)	1106.8(1)	451.27(5)	153.68(2)
$\sigma_{\rm LO}^{\rm VBFNLO}$ [fb]	1686.90(5)	1433.79(4)	1290.42(4)	1106.97(3)	451.31(1)	153.689(4)
$\sigma_{\rm LO}^{\rm QCD+EW}$ [fb]	1686.5(3)	1432.7(2)	1289.8(2)	1106.4(1)	451.16(5)	153.66(2)
$\sigma_{\rm NLO}^{\rm CDD}$ [fb]	1728(2)	1463(1)	1313(2)	1121(1)	444.8(3)	147.2(1)
$\sigma_{\rm NLO}^{\rm VBFNLO}$ [fb]	1728.8(2)	1461.7(2)	1311.7(1)	1119.8(1)	444.71(3)	147.14(1)
$\sigma_{\rm NLO}^{\rm full\ QCD}$ [fb]	1738(2)	1468(2)	1318(1)	1122(1)	445.0(4)	147.23(9)
$\sigma_{\rm NLO}^{\rm QCD+EW}$ [fb]	1599(2)	1354(2)	1230(1)	1048(1)	419.2(4)	155.8(1)

Table 2: Integrated cross section for $\rm pp \to H + 2jets + X$ in LO and NLO, including VBF selection cuts, calculated by `CDD`, $\sigma_{\rm LO/NLO}^{\rm CDD}$, and with `VBFNLO`, $\sigma_{\rm LO/NLO}^{\rm VBFNLO}$, for the setup defined in the text.

sizeable difference between those results, which arises almost exclusively from s-channel contributions. Furthermore, EW corrections are in general as large as QCD corrections.

Acknowledgements

This work is supported in part by the European Community's Marie-Curie Research Training Network under contract MRTN-CT-2006-035505 "Tools and Precision Calculations for Physics Discoveries at Colliders".

4. LOOP INDUCED INTERFERENCE EFFECTS IN HIGGS PLUS TWO JET PRODUCTION AT THE LHC [5]

4.1 Introduction

Understanding the mechanism of electro-weak symmetry breaking is one of the primary goals at the CERN Large Hadron Collider. Central to this study is the measurement of the couplings of any observed Higgs scalar to the electro-weak bosons. A useful production process in this context is $pp \to Hjj$ [125–127] through weak boson fusion (WBF) [128], as shown in Fig. 5(a), with contributions from all identifiable decay channels. The Higgs plus two jet signature also receives contributions from Higgs boson production through gluon-fusion mediated through a top-loop, as illustrated in Fig. 5 (b). However, the Higgs plus dijet-sample can be biased towards WBF by suppressing the gluon-fusion chan-

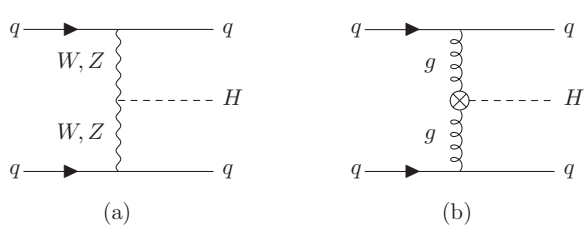

Fig. 5: (a) The WBF process for Higgs production in the Standard Model and (b) the equivalent gluon-fusion diagram mediated through a top-loop.

nel through a combination of cuts.

The next-to-leading order corrections to Higgs plus two jet production are considered to be well under control. For WBF, both the radiative corrections within QCD [10, 71, 72, 129] and the electro-weak sector [75, 76] have been calculated; for the gluon fusion process, the first radiative corrections have been calculated within QCD [32, 130] using the heavy top mass effective Lagrangian [9, 10, 131]. The radiative corrections to the WBF channel are small, $3\% - 6\%$, and there is even partial numerical

[5] Contributed by J. R. Andersen, T. Binoth, G. Heinrich, J. M. Smillie

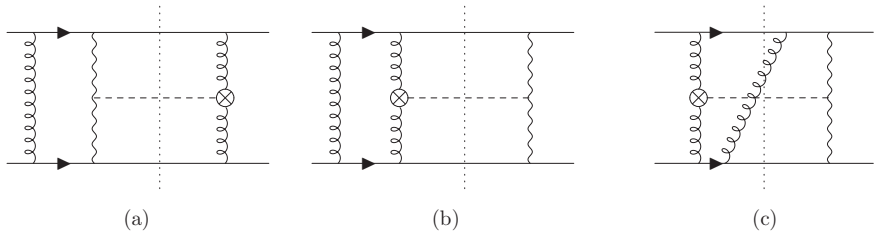

Fig. 6: Example of contributing one-loop interference terms: (a) $\mathcal{M}_{gZ}\mathcal{M}_g^*$ and (b) $\mathcal{M}_{gg}\mathcal{M}_Z^*$. There are four contributing topologies for each gluon-fusion and Z-fusion process. (c) shows a real emission processes at matrix element squared level.

cancellation between the QCD and electro-weak contributions. It would therefore seem that the Higgs coupling to electro-weak bosons can be very cleanly studied with a Hjj-sample.

However, there is an irreducible (i.e. unaffected by the WBF cuts) contamination in the extraction of the ZZH-coupling from interference between the gluon fusion and WBF processes, which was ignored in the literature until recently. At tree level, such interference is only allowed in amplitudes where there is a $t \leftrightarrow u$-channel crossing which leads to a high level of kinematic suppression [132]. These and other crossing-suppressed one-loop amplitudes were later calculated together with the electro-weak corrections [75, 76].

Here we will report on the calculation of the processes allowed at the one-loop level which do not suffer from the kinematic suppression stemming from the requirement of a $t \leftrightarrow u$-crossing [133]. At order $\mathcal{O}(\alpha^2\alpha_s^3)$, one finds an interference term between the gluon- and Z-induced amplitude which is not allowed at $\mathcal{O}(\alpha^2\alpha_s^2)$ by colour conservation. The W-induced amplitudes are crossing-suppressed and therefore not taken into account. The diagrams where the vector boson is in the s-channel can also be safely neglected because they are strongly suppressed by the WBF cuts. As discussed in Ref. [132], for identical quark flavours the loop amplitudes are the first order which does not require a kinematically disfavoured crossing.

In the following section we will briefly sketch the calculation before discussing our results in section 4.3, which are summarized in the conclusions.

4.2 The Calculation

Our calculation of the loop interference terms and the real emission contributions is based on helicity amplitudes. The leading order amplitudes, denoted by $\mathcal{M}_Z$ and $\mathcal{M}_g$ (Fig. 5(a) and (b)), are proportional to a colour singlet and a colour octet term. The colour singlet is formally of order $\mathcal{O}(\alpha^2)$ whereas the octet is of order $\mathcal{O}(\alpha_s^2)$. The one-loop amplitudes, which we call $\mathcal{M}_{gZ}$ and $\mathcal{M}_{gg}$ respectively, are mixtures of octet and singlet terms. For the interference term we need to consider only the octet part of $\mathcal{M}_{gZ}$ and the singlet part of $\mathcal{M}_{gg}$. One finds that only four one-loop five-point topologies for each amplitude survive this colour projection. Sample diagrams are shown in Fig. 6.

The loop amplitudes require the evaluation of one-loop five-point tensor integrals with a mixture of massless and massive configurations in both propagators and external legs. We apply the reduction algorithm outlined in Ref. [134, 135] to express each Feynman diagram as a linear combination of 1-, 2-, and 3-point functions in $D = 4 - 2\epsilon$ dimensions and 4-point functions in D=6. The same algorithm has been successfully applied to a number of one-loop computations [64, 136–138], where further details can be found. The algebraic expressions were checked by independent implementations, both amongst the authors and with another group [139].

After the algebraic reduction, all helicity amplitudes are obtained as linear combinations of scalar integrals. No one-point functions appear in the reduction, and also two-point functions are absent in the amplitudes of $\mathcal{M}_{gZ}$. Furthermore, coefficients of some of the integrals which arise in several topologies sum to zero. If the tree resulting from a certain cut of a master integral corresponds to a helicity forbidden

p_{a_T}, p_{b_T}	> 20 GeV	$\eta_a \cdot \eta_b$	< 0
η_j	< 5	$\lvert\eta_a - \eta_b\rvert$	> 4.2
s_{ab}	$> (600\text{ GeV})^2$		

Table 3: The cuts used in the following analysis which bias the Higgs Boson plus dijet sample towards WBF. The indices a, b label the tagged jets.

tree level process, one can immediately infer the vanishing of the corresponding coefficient. In our algebraic tensor reduction approach we verify and use such cancellations before the numerical evaluation of the cross section.

As most of the required scalar integrals are not provided in the literature, we have evaluated representations in terms of analytic functions valid in all kinematic regions. These can be found in [133] for use in other calculations.

We used dimensional regularisation to extract the IR singularities from the divergent integrals. The leading $1/\varepsilon^2$ poles cancel, but there remains a $1/\varepsilon$ pole which is cancelled when the virtual corrections are combined with the real emission part shown in Fig. 6(c). As to be expected, the collinear IR divergences from the three-parton final states integrate to zero, leaving only a soft divergence proportional to $1/\varepsilon$, which we isolated using the phase space slicing method [140, 141]. The phase space integration and the numerical evaluation of integrals and coefficients is coded in a `C++` program allowing for a flexible implementation of cuts and observables.

4.3 Results

As the aim of our study was to investigate a possible pollution of the clean extraction of the ZZH vertex structure by the interference terms, we apply the cuts summarised in Table 3. These are generally used to single out the WBF events from the gluon fusion "background" [77]. Our input parameters for the numerical studies are taken from [106] and [142]. In addition, we use a Higgs boson mass of 115 GeV and the NLO parton distribution set from Ref. [106]. We use 2-loop running for α_s, in accordance with the chosen pdfs.

We observe that in all the flavour and helicity channels, the contribution from the 3-parton final state is numerically negligible. The only rôle of this real emission is to cancel the divergences which arise from the one-loop diagrams.

As the interference effect is proportional to $2\mathrm{Re}(\mathcal{M}_{gg}\mathcal{M}_Z^* + \mathcal{M}_{gZ}\mathcal{M}_g^*)$, the result is not necessarily positive definite. In fact, the sign of the interference contribution depends on the azimuthal angle between the two tagging jets, $\Delta\phi_{jj}$. As the event topology has two well separated jets, it becomes possible to define an orientation of the azimuthal angle which allows observability in the whole range of $[-\pi, \pi]$, as pioneered in Ref. [110, 128]. $\Delta\phi_{jj}$ is then defined through

$$\begin{aligned} |p_{+_T}||p_{-_T}|\cos\Delta\phi_{jj} &= p_{+_T}\cdot p_{-_T}, \\ 2|p_{+_T}||p_{-_T}|\sin\Delta\phi_{jj} &= \varepsilon_{\mu\nu\rho\sigma} b_+^\mu p_+^\nu b_-^\rho p_-^\sigma, \end{aligned} \tag{6}$$

where b_+ (b_-) are unit vectors in positive (negative) beam direction, and likewise for the jet momenta $p_\pm$. The cuts ensure that the two tagging jets lie in opposite hemispheres. Defined in this way, the observable $\Delta\phi_{jj}$ becomes a powerful discriminator for different CP-structures of the Higgs Boson production vertex [110].

Figure 7 displays the contribution to the distribution in $\Delta\phi_{jj}$ from the interference terms for various helicity and flavour configurations. There is an accidental cancellation of sea and valence quark contributions which leads to the fact that the sum over all flavour and helicity assignments peaks at around 2 ab/rad only, with an integrated effect of 1.19 ± 0.07 ab, where the error is due to the numerical integration.

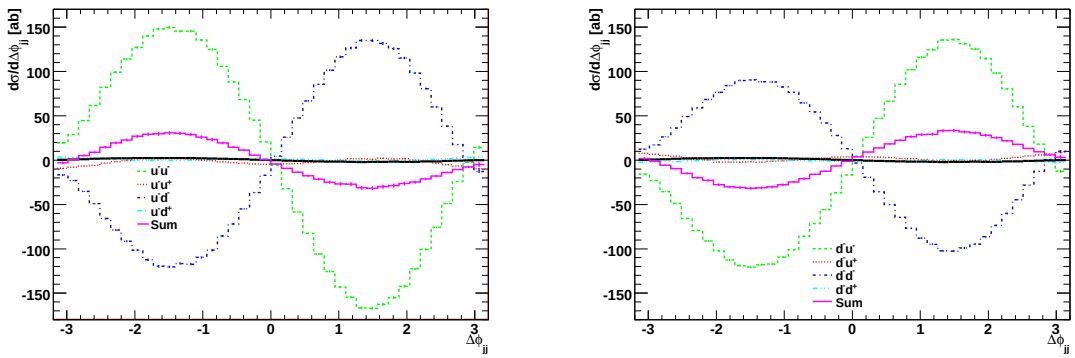

Fig. 7: The $\Delta\phi_{jj}$-distribution for various flavour and helicity-configurations. The purple histogram labelled "Sum" indicates the sum over the four contributions shown. The sum over *all* flavour and helicity assignments including all sea flavours is shown in the black histogram.

Due to the oscillatory behaviour, the total integrated cross section does not represent the impact on the $\Delta\phi_{jj}$ distribution. The integral of the absolute value of the $\Delta\phi_{jj}$ distribution, $\int_{-\pi}^{\pi} d\Delta\phi_{jj} \left| \frac{d\sigma}{d\Delta\phi_{jj}} \right|$, is a more useful measure of the impact of the interference effect on the extraction of the ZZH-vertex. This integral evaluates to 9.1 ± 0.1 ab, an order of magnitude larger than the integral over the oscillating distribution. The total integral over the the absolute value of the fully differential cross section leads to 29.59 ± 0.07 ab.

Using the same cuts and value for the mass of the Higgs boson as in the present study, we have checked that the total contribution to the $\Delta\phi_{jj}$-distribution from the leading order WBF process (both Z and $W^{+/-}$ included) is relatively flat at around 240 fb/rad. Therefore, the result of the interference effect reported here is unlikely to be measurable.

As can be readily seen in Fig. 7, there is also a cancellation between the contribution from each flavour and helicity assignment, as has also been pointed out in [143]; this is because the sign of quark couplings to the Z-boson becomes relevant as it is not squared for the interference. The flavour- and helicity sum for each quark line therefore leads to some cancellation, which amounts to roughly 20% in the most relevant regions of the pdfs [133].

The complex phases arising from the full one-loop calculation of the amplitudes also give rise to some suppression. We find that the relevant products and sums for the interference effect project out only about 20% of the full complex loop amplitudes.

We chose the factorisation and renormalisation scales as in accordance with the natural scales in the relevant high energy limit (as explained in Ref. [78]), i.e. the factorisation scales are set equal to the transverse momenta of the relevant jet, and the renormalisation scale for the strong couplings are chosen correspondingly, i.e. one α_s evaluated at each value of the transverse momentum of the jets, and one at the Higgs mass. However, we find that varying the choice of factorisation and renormalisation scales, the exact numerical values of the cuts or the parameters, or the choice of pdf set has no impact on the conclusions: the numerical importance of the interference is basically unchanged.

4.4 Conclusions

We have outlined the calculation of the loop-induced $\mathcal{O}(\alpha^2\alpha_s^3)$ interference effect between the gluon fusion and weak boson fusion processes in Higgs boson plus two jet production at the LHC.

We find by explicit calculation that this contribution is too small to contaminate the extraction of the ZZH-coupling from WBF processes. Interestingly the effect which survives comes dominantly from the virtual corrections. We have analysed in detail why this contribution is so small, and instead of

$p_{c_\perp}, p_{d_\perp}, p_{j_\perp}$	> 40 GeV	$y_c \cdot y_d$	< 0
y_j	< 5	$\lvert y_c - y_d \rvert$	> 4.2
s_{cd}	$> (600\text{ GeV})^2$	$y_c \leq y_h \leq y_d$	

Table 4: The cuts used in the following analysis which bias the Higgs boson plus dijet sample towards WBF. The suffices c, d label the tagged jets, j any (possibly further) jet in the event.

a single effect we rather find a conspiracy of several mechanisms:

- accidental cancellations between the sea quark and valence quark contributions
- compensations between different weak isospin components of the valence quarks due to their $SU(2) \times U(1)$ couplings, in combination with their weights from the (valence) quark content of the proton
- cancellations due to destructive interference of the phases from the different contributions.

The exact impact of these partly accidental effects, in particular the latter, could not be assessed without an explicit calculation.

Finally we would like to point out that anomalous couplings which affect the phases could change the interference pattern substantially. However, the first two cancellation mechanisms still being present, we still expect the overall contribution to be experimentally insignificant. Please see Ref. [144] for more details.

Acknowledgements

We would like to thank Lance Dixon for enlightening and encouraging discussions and important comments. The authors were all supported by the UK Science and Technology Facilities Council. In addition, the work of TB was supported by the Deutsche Forschungsgemeinschaft (DFG) under contract number BI 1050/2 and the Scottish Universities Physics Alliance (SUPA).

5. HIGGS BOSON PRODUCTION IN ASSOCIATION WITH MULTIPLE HARD JETS [6]

5.1 Introduction

It is widely hoped that the LHC will discover the source of electro-weak symmetry breaking, mediated by the Higgs scalar within the context of the Standard Model. In order to determine whether any observed fundamental scalar is the Higgs Boson of the Standard Model, it is imperative to determine its couplings, especially to the weak gauge bosons. This is possible both by measuring the decay of the Higgs boson through the weak bosons, but also by isolating the Higgs Boson production through weak boson fusion (WBF). This process contributes to the signal for the production of a Higgs boson in association with two jets. This channel also receives a significant contribution from higher order corrections to Higgs boson production through gluon fusion. In fact, it has recently been suggested [145] that the increased significance of the signal over the background obtained by requiring at least two hard jets in association with a Higgs boson may decrease the necessary integrated luminosity required for a discovery of the Higgs boson through gluon fusion processes. However, in order to measure the Higgs boson couplings to the weak bosons, it is necessary to suppress the gluon fusion contribution to the production of a Higgs boson in association with two jets. This is achieved [77] by applying the so-called *weak boson fusion*-cuts: It is expected that the contribution from the gluon fusion process will be further suppressed relative to WBF by vetoing further jet activity [146]. The efficiency of such cuts can only be assessed by calculating the higher order corrections to the gluon fusion contribution to the hjj-channel. The first radiative corrections have recently been calculated [32]. While this fixed order approach certainly is the best tested and understood approach for predicting the first few perturbative corrections, the calculational

[6] Contributed by: J.R. Andersen and C.D. White

complexity means that currently the production of hjj through gluon fusion has only been calculated at next-to-leading order.

It is possible to estimate final state jet emission in this process [78] using parton shower algorithms. In this contribution we examine a different approach, and consider how to best estimate hard jet emission in Higgs production via gluon fusion. We take as a starting point a factorised form for the scattering amplitudes, which formally applies in a certain kinematic limit (that of multi-Regge-kinematics (MRK)). We extend the domain of applicability of the amplitudes from Asymptotia into the region of relevance for the LHC by using known all-order constraints of scattering amplitudes. We validate the approach by checking the approximations in a comparison with fixed order results, where these are available. Furthermore, the resulting estimate for the n-parton final state (which includes some virtual corrections) is then matched to the known tree level results for hjj and hjjj. Finally, we implement the description in a Monte Carlo event generator for Higgs + multiparton production, and present a sample of results.

5.2 Estimating Multijet Rates

5.21 The FKL Amplitude

Our starting point is the FKL factorised $(2 \to n+2)$-gluon amplitudes [147] adapted to include also a Higgs boson

$$\begin{aligned} i\mathcal{M}_{\rm HE}^{ab\to p_0\ldots p_j h p_{j+1} p_n} &= 2i\hat{s}\left(ig_s f^{ad_0c_1} g_{\mu_a\mu_0}\right) \\ &\cdot \prod_{i=1}^{j}\left(\frac{1}{q_i^2}\exp[\hat{\alpha}(q_i^2)(y_{i-1}-y_i)]\left(ig_s f^{c_i d_i c_{i+1}}\right) C_{\mu_i}(q_i,q_{i+1})\right) \\ &\cdot \left(\frac{1}{q_h^2}\exp[\hat{\alpha}(q_i^2)(y_j-y_h)] C_H(q_{j+1},q_h)\right) \\ &\cdot \prod_{i=j+1}^{n}\left(\frac{1}{q_i^2}\exp[\hat{\alpha}(q_i^2)(y'_{i-1}-y'_i)]\left(ig_s f^{c_i d_i c_{i+1}}\right) C_{\mu_i}(q_i,q_{i+1})\right) \\ &\cdot \frac{1}{q_{n+1}^2}\exp[\hat{\alpha}(q_{n+1}^2)(y'_n-y_b)]\left(ig_s f^{bd_{n+1}c_{n+1}} g_{\mu_b\mu_{n+1}}\right) \end{aligned} \tag{7}$$

where g_s is the strong coupling constant, and q_i, q_h are the 4-momentum of gluon propagators (e.g. $q_i = p_a - \sum_{k=0}^{i-1} p_k$ for $i < j$), C_{μ_i} is the *Lipatov effective vertex* for gluon emission, and C_H is the effective vertex for the production of a Higgs boson, as calculated in Ref. [148]. Furthermore, $\hat{\alpha}(q_i^2)$ occurs from the Reggeisation of the gluon propagator, and encodes virtual corrections (see e.g. [149]). This approximation formally applies in the MRK limit, which can be expressed in terms of the rapidities $\{y_i\}$ of the outgoing partons and their transverse momenta $\{p_{i\perp}\}$:

$$y_0 \gg y_1 \gg \ldots \gg y_{n+1}; \quad p_{i\perp} \simeq p_{i+1\perp}; \quad q_i^2 \simeq q_j^2. \tag{8}$$

This limit is particularly well suited for studies within the WBF cuts of Table 4, since a large rapidity span of the event is then guaranteed.

In the true limit of MRK, the squared 4-momenta $q_i^2 \to -q_{\perp i}^2$, and the square of the Lipatov vertices fulfil $-C_{\mu_i}C^{\mu_i} \to 4\frac{q_{\perp i}q_{\perp i+1}}{k_{\perp i}}$. Applying these limits, the sum over n to infinity of the amplitudes in Eq. (7), integrated over the full phase space of emitted gluons can be obtained by solving two coupled BFKL equations. This result would then apply to the phase space of

$$y_0 \gg y_1 \gg \ldots \gg y_{n+1}; \quad p_{i\perp} \simeq p_{i+1\perp}; \quad q_{\perp i}^2 \simeq q_{\perp j}^2. \tag{9}$$

While both expressions are equally valid in the region of Asymptotia, we extend the applicability of the results obtained in the High Energy Limit to the region of interest for particle physics phenomenology by adhering to the following guidelines:

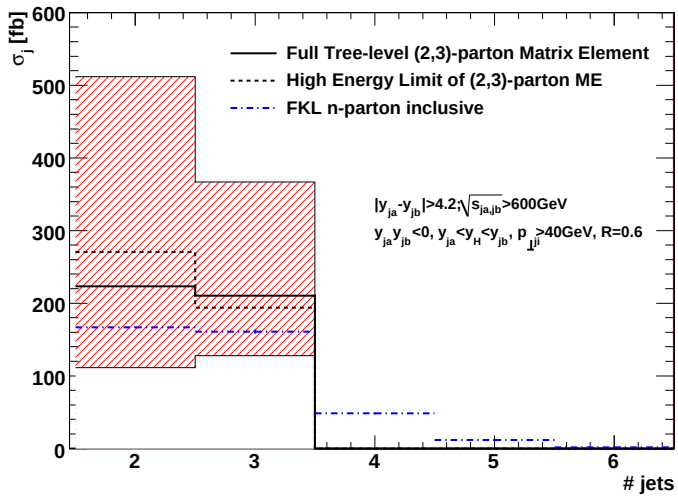

Fig. 8: The 2 and 3 parton cross-sections calculated using the known LO matrix elements (solid), and the estimate gained from the modified high energy limit (dashed). One sees that the estimate is well within the scale variation of the LO result, obtained by varying the common renormalisation and factorisation scales in the range $0.5 \leq \mu/\mu_0 \leq 2$, where μ_0 is the default choice (indicated by the shaded regions). Also shown is the result obtained from the fully inclusive n-parton sample of Eq. (7).

1. DO NOT INTRODUCE NEW DIVERGENCES: Using the expression in Eq. (7) corresponds to *removing* some divergences from the full scattering amplitude (the collinear divergences), but not *moving* any divergences. The expression in Eq. (7) is divergent only for momentum configurations for which the full scattering amplitude is also divergent. This is different to the case where the MRK limit of invariants has been substituted (resulting from the use of the BFKL equation), which displaces divergences within the phase space region of interest for the LHC.
2. DO NOT APPLY THE FORMALISM WHERE IT FAILS: We choose minimal interception by only removing the *small* region on phase space where the expression of Eq. (7) results in unphysical (negative) differential cross sections. This happens when the effective Lipatov vertex is applied to momentum configurations very far from the MRK, where it is possible to obtain $-C_{\mu_i}C^{\mu_i} < 0$. It is perhaps interesting to note that restricting the region of phase space where the formalism is applied is similar to the *kinematic constraint* of Ref. [150–152], although in fact the latter fails to exclude all of the region where the formalism underpinning the BFKL equation fails.

In figure 8 we compare the prediction for the production of a Higgs boson in association with two and three partons (in a hard two-jet and three-jet configuration respectively) within the WBF cuts of table 4, obtained using both the full matrix element (extracted from `MADEvent/MADGraph` [153]) and the relevant expression of Eq. (7) for two and three parton production, with the virtual corrections set to zero ($\hat{\alpha} = 0$). We choose renormalisation and factorisation scale in accordance with the study of Ref. [78]. One notes two things. Firstly, the approximation to the jet rates is well within the scale uncertainty of the known tree level results. We have therefore explicitly shown that the terms taken into account in this approach indeed dominate . Secondly, the cross section for the production of a Higgs boson in association with 3 jets is similar to the one for the production of a Higgs boson in association with two jets. The large size of the three-jet rate was already reported in Ref. [130], and clearly demonstrates the necessity of considering hard multi-parton final states in order to describe correctly the expected event topology and to answer questions on e.g. the effectiveness of a central jet veto in suppressing the gluon fusion channel.

	A_ϕ
LO 2-jet	0.504 ± 0.0013
$\sum_n n$-parton, $=$ 2-jet	0.267 ± 0.0034
LO 3-jet	0.228 ± 0.0018
$\sum_n n$-parton, $\geq$ 2-jet	0.161 ± 0.0087

Table 5: The angular decorrelation parameter given by equation (10), subject to the cuts of table 4. Note that the 2 and 3-jet values are obtained from matrix elements matched to the known tree level results.

5.3 All Order Results and Matching

The divergence in Eq. (7) obtained when any $p_i \to 0$ is regulated by the divergence of the virtual corrections encoded in $\hat{\alpha}$. By implementing the regularisation through phase space slicing it becomes possible to obtain the fully inclusive any-parton sample by summing Eq. (7) over all j, n. This is very efficiently implemented by following the method for phase space generation outlined in Ref. [154]. Furthermore, since we can trivially expand the expressions to any order in α_s, it is possible to check the performance of the formalism against the available tree-level results, and to implement matching to these. We choose to implement $\ln R$-matching at the amplitude-level for channels which have a contribution in the high-energy limit (e.g. $ug \to hug$ and $gg \to hggg$), and R-matching for those which do not (e.g. $gg \to hu\bar{u}$ and $u\bar{u} \to hggg$).

It is now possible to cluster each event in the inclusive sample of a Higgs boson plus n partons into jets according to a given algorithm. As an example, we choose KtJet [155]. We use the parton distribution functions of Ref. [106]. The distribution of final state jets subject to the cuts of table 4 is shown with the dashed histogram in Figure 8. One sees a significant number of events with more than 3 hard ($p_\perp > 40$GeV) jets. More importantly though, the method outlined in this paper allows for an estimate of the emissions of partons not quite hard enough to be classified as jets, but still causing sufficient decorrelation. The azimuthal angular correlation between the tagging jets has been suggested previously as a good observable for differentiating between the GGF and WBF production modes. Furthermore, the nature of the distribution of the azimuthal angle ϕ between the two tagging jets can potentially be used to determine the nature of the Higgs coupling to fermions [145]. However, the usefulness of this observable is threatened by hard jet emission which acts to decorrelate the tagging jets. As suggested in Ref. [156] the structure of the distribution $d\sigma/d\phi_{j_a j_b}$ can be distilled into a single number A_ϕ given by:

$$A_\phi = \frac{\sigma(\phi_{j_a j_b} < \pi/4) - \sigma(\pi/4 < \phi_{j_a j_b} < 3\pi/4) + \sigma(\phi_{j_a j_b} > 3\pi/4)}{\sigma(\phi_{j_a j_b} < \pi/4) + \sigma(\pi/4 < \phi_{j_a j_b} < 3\pi/4) + \sigma(\phi_{j_a j_b} > 3\pi/4)} \tag{10}$$

The results using our approach are collected in Table 5. Of particular interest is the difference between the first two numbers. The first ($A_\phi = 0.504 \pm 0.0013$) describes the result obtained in the two-jet tree-level calculation. The second ($A_\phi = 0.267 \pm 0.0034$) is the result obtained for events classified as containing only two hard jets, but completely inclusive in the number of final state partons. The difference is mostly due to the decorrelation caused by the additional radiation not classified as hard jets. As expected, the further hard emissions have a stronger effect than estimated using a parton shower approach [78].

5.4 Conclusions

We have outlined a new technique for estimating multiple hard parton emission, and demonstrated its application to Higgs boson production (via GGF) in association with two jets. Our starting point is the FKL factorised form of Higgs+multijet amplitudes, which formally applies in multi-Regge kinematics (MRK). We extend the region of applicability of the formalism by adhering to two simple rules. We compare the results obtained order by order to those obtained in a fixed order approach and find very good agreement. The approximations are well within the uncertainty estimated by varying the renormalisation and factorisation scale by a factor of two in the tree level results.

We have presented example results for the distribution of final state jets, and for the azimuthal decorrelation parameter A_ϕ. We find significant decorrelation arising from additional hard final state radiation not captured by present NLO calculations; significantly more than previously estimated using parton shower algorithms.

The technique outlined here can be extended to e.g. W+jet emission, as well as pure multijet final states. It would be very interesting to interface the final states found here with parton shower algorithms, thus resumming in principle both the number of jets (hard partons) and the structure of each (soft collinear radiation). Furthermore, the results presented here are based upon effective vertices correct to leading logarithmic order. Work is in progress towards extending the accuracy to next-to-leading logarithmic order.

Acknowledgements

CDW is funded by the Dutch Organisation for Fundamental Matter Research (FOM). He thanks Eric Laenen and Jos Vermaseren for helpful discussions. We are also grateful to Vittorio Del Duca and Gavin Salam for encouraging conversations.

6. GLUON- INDUCED Z-BOSON PAIR PRODUCTION AT THE LHC: PARTON LEVEL RESULTS [7]

6.1 Introduction

The hadronic production of Z boson pairs provides an important background for Higgs boson searches in the $H \to ZZ$ channel at the LHC. It has been studied extensively in the literature including higher order corrections [59, 60, 157, 158]. Production of Z boson pairs through gluon fusion contributes at $\mathcal{O}(\alpha_s^2)$ relative to $q\bar{q}$ annihilation, but its importance is enhanced by the large gluon flux at the LHC. It was analyzed in Refs. [159, 160]. Leptonic Z decays were subsequently studied for on-shell [161] and off-shell [162] vector bosons. In this note we present the first complete calculation of the gluon-induced loop process $gg \to Z(\gamma)Z(\gamma) \to \ell\bar{\ell}\ell'\bar{\ell}'$, allowing for arbitrary invariant masses of the Z bosons and including the γ contributions. Our calculation employs the same methods as Refs. [64, 136]. The tensor reduction scheme of Refs. [134, 135] has been applied to obtain the amplitude representation implemented in our program. We compared it numerically with an amplitude representation based on FeynArts/FormCalc [163, 164] and found agreement. Note that single resonant diagrams (in the case of massless leptons) and the corresponding photon exchange diagrams give a vanishing contribution. A combination of the multi-channel [165] and phase-space-decomposition [67, 166] Monte Carlo integration techniques was used with appropriate mappings to compensate peaks in the amplitude. A more detailed description of our calculation can be found in a forthcoming article.

6.2 Results

In this section we present numerical results for the process $pp \to Z(\gamma)Z(\gamma) \to \ell\bar{\ell}\ell'\bar{\ell}'$ at the LHC, i.e. for the production of two charged lepton pairs with different flavor. Note that no flavor summation is applied. First, we give the cross section when standard LHC cuts for Z boson production [60] are applied. More precisely, we require 75 GeV $< M_{\ell\ell} <$ 105 GeV for the invariant masses of $\ell\bar{\ell}$ and $\ell'\bar{\ell}'$, which suppresses the photon contribution to less than 1%. Motivated by the finite acceptance and resolution of the detectors we further require $p_{T\ell} > 20$ GeV and $|\eta_\ell| < 2.5$ for all produced leptons. To obtain numerical results we use the following set of input parameters: $M_W = 80.419$ GeV, $M_Z = 91.188$ GeV, $G_\mu = 1.16639 \times 10^{-5}$ GeV^{-2}, $\Gamma_Z = 2.44$ GeV. The weak mixing angle is given by $c_\mathrm{w} = M_W/M_Z,\ s_\mathrm{w}^2 = 1 - c_\mathrm{w}^2$. The electromagnetic coupling is defined in the G_μ scheme as $\alpha_{G_\mu} = \sqrt{2}G_\mu M_W^2 s_\mathrm{w}^2/\pi$. The masses of external fermions are neglected. The values of the heavy quark masses in the intermediate loop are set to

[7] Contributed by: T. Binoth, N. Kauer, and P. Mertsch

	$\sigma(pp \to Z^*(\gamma^*)Z^*(\gamma^*) \to \ell\bar{\ell}\ell'\bar{\ell}')$ [fb]				
	gg	$q\bar{q}$		$\frac{\sigma_{\rm NLO}}{\sigma_{\rm LO}}$	$\frac{\sigma_{\rm NLO+gg}}{\sigma_{\rm NLO}}$
		LO	NLO		
$\sigma_{\rm std}$	$1.492(2)$	$7.343(1)$	$10.953(2)$	1.49	1.14

Table 6: Cross sections for the gluon and quark scattering contributions to $pp \to Z^*(\gamma^*)Z^*(\gamma^*) \to \ell\bar{\ell}\ell'\bar{\ell}'$ at the LHC ($\sqrt{s} = 14$ TeV) where standard LHC cuts (75 GeV $< M_{\ell\ell} <$ 105 GeV, $p_{T\ell} >$ 20 GeV, $|\eta_\ell| < 2.5$) are applied. The integration error is given in brackets. We also show the ratio of the NLO to LO cross sections and the ratio of the combined NLO+gg contribution to the NLO cross section.

$M_t = 170.9$ GeV and $M_b = 4.7$ GeV. The pp cross sections are calculated at $\sqrt{s} = 14$ TeV employing the CTEQ6L1 and CTEQ6M [122] parton distribution functions at tree- and loop-level, corresponding to $\Lambda_5^{\rm LO} = 165$ MeV and $\Lambda_5^{\overline{\rm MS}} = 226$ MeV with one- and two-loop running for $\alpha_s(\mu)$, respectively. The renormalization and factorization scales are set to M_Z.

We compare results for $\ell\bar{\ell}\ell'\bar{\ell}'$ production in gluon scattering with LO and NLO results for the quark scattering processes. Since we are interested in $Z(\gamma)Z(\gamma)$ production as a background, the $gg \to H \to ZZ$ signal amplitude is not included. The LO and NLO quark scattering processes are computed with MCFM [60], which implements helicity amplitudes with full spin correlations [167] and includes finite-width effects and single-resonant corrections. Table 6 shows gluon and quark scattering cross sections for the LHC. We find a NLO K-factor for $q\bar{q} \to ZZ$ of 1.5. Enhanced by the large gluon flux at the LHC, the gg process yields a 14% correction to the total ZZ cross section calculated from quark scattering at NLO QCD. This is substantially higher than the corresponding 6% increase for WW production [136], where no right-handed Vff coupling contributes. Relative to the LO $q\bar{q} \to ZZ$ prediction the gg contribution is about 20% in agreement with the finding in Ref. [162]. Without top and bottom quark contribution the gg cross section is $0.885(1)$ fb. The massive bottom and top loops increase the result based on intermediate light quarks by about 70%. This is much more than the corresponding 15% for $gg \to WW$ [136], where all quark loops are suppressed by at least one top propagator. In the $gg \to ZZ$ case on the other hand a pure b quark loop occurs and gives rise to a contribution that is similar to the massless first or second generation down quark loop. We estimate the remaining theoretical uncertainty introduced by the QCD scale by varying the renormalization and factorization scales independently between $M_Z/2$ and $2M_Z$. For the $gg \to ZZ$ process we find a renormalization and factorization scale uncertainty of approximately 20%. The scale uncertainty of the $q\bar{q} \to ZZ$ process at NLO is approximately 4%. The scale uncertainties are thus similar for $gg \to ZZ$ and $gg \to WW$.

Selected differential distributions for $pp \to Z(\gamma)Z(\gamma) \to \ell\bar{\ell}\ell'\bar{\ell}'$ at the LHC are shown in Fig. 9, where the standard set of cuts defined above is applied. Fig. 9a) shows the distribution in the invariant mass M_{4l} of the four produced leptons. We compare the gluon-gluon induced contribution with the quark scattering processes in LO and NLO. We observe that the invariant mass distribution of the gluon-gluon induced process is similar in shape to the quark scattering contributions and suppressed by about one order of magnitude in normalization. Z boson pairs produced in quark-antiquark scattering at the LHC are in general strongly boosted along the beam axis. Gluon-induced processes on the other hand result in ZZ events at more central rapidities. This feature is born out by the distribution in the pseudorapidity of the negatively charged lepton shown in Fig. 9b). In order to distinguish the shapes of the various contributions we have chosen a linear vertical scale and plot the gluon-gluon contribution multiplied by a factor 10. Compared to LO quark-antiquark scattering, the lepton distribution of the gluon-gluon process shows a more pronounced peak at central rapidities. We also observe an enhancement of the NLO corrections at central rapidities which is due to the substantial contribution of gluon-quark processes at NLO. To demonstrate the impact of the photon contribution, we show in Fig. 10 distributions for the

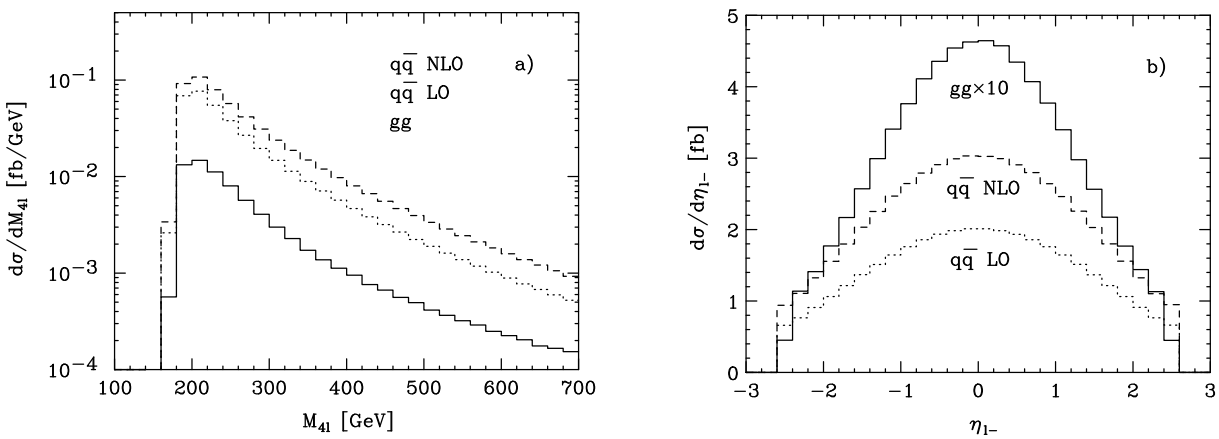

Fig. 9: Distributions in the $\ell\bar{\ell}\ell'\bar{\ell}'$ invariant mass M_{4l} (a) and the pseudorapidity η_{ℓ^-} of the negatively charged lepton (b) for the gluon scattering process (solid) and the quark scattering processes in LO (dotted) and NLO QCD (dashed) of $pp \to Z^*(\gamma^*)Z^*(\gamma^*) \to \ell\bar{\ell}\ell'\bar{\ell}'$ at the LHC. Input parameters as defined in the main text. Standard LHC cuts are applied (see main text and Table 6). The gg distribution of η_{ℓ^-} is displayed after multiplication with a factor 10.

gluon-gluon induced process that include only ZZ, only $\gamma\gamma$ and all contributions. Here, a minimal set of cuts is applied, i.e. only $M_{\ell\ell} > 5$ GeV in order to exclude the photon singularity.[8] With this minimal set of cuts the LHC cross section for $gg \to Z(\gamma)Z(\gamma) \to \ell\bar{\ell}\ell'\bar{\ell}'$ increases to $7.874(5)$ fb. In Fig. 10a) the Z and γ contributions to the distribution in the invariant mass M_{4l} are displayed. We observe that for Higgs masses below the Z-pair threshold, where one Z boson is produced off-shell, the photon contribution to the background is important. In Fig. 10b) the contributions are shown for the distribution of the transverse momentum $p_{T\ell^-}$ of the negatively charged lepton. For this observable, the photon contribution becomes non-negligible for values below 70 GeV.

6.3 Conclusions

We have calculated the loop-induced gluon-fusion process $gg \to Z^*(\gamma^*)Z^*(\gamma^*) \to \ell\bar{\ell}\ell'\bar{\ell}'$, which provides an important background for Higgs boson searches in the $H \to ZZ$ channel at the LHC. Our calculation demonstrates that the gluon-fusion contribution to the ZZ background yields a correction of about 15% to the $q\bar{q}$ prediction at NLO QCD and that the photon contribution is important for Higgs masses below the Z-pair threshold. We conclude that the gluon-gluon induced background process should be taken into account for an accurate determination of the discovery potential of Higgs boson searches in the $pp \to H \to ZZ \to$ leptons channel. Our public program, named `GG2ZZ`, includes the ZZ, $Z\gamma$ and $\gamma\gamma$ contributions with full spin and polarization correlations, off-shell and interference effects, as well as finite top and bottom quark mass effects. It is available on the Web [168] and can be used as Monte Carlo integrator or to generate unweighted parton-level events in Les Houches standard format [169, 170]. ATLAS and CMS are currently using our program to study the hadron-level impact of the $gg \to ZZ$ background on $H \to ZZ$ searches at the LHC.

Acknowledgements

T. Binoth and N. Kauer would like to thank the Ecole de Physique des Houches and the Galileo Galilei Institute for Theoretical Physics for the hospitality and the INFN for partial support during the completion

[8] As in Ref. [162], a technical cut $p_{TZ} > 2$ GeV is employed with standard cuts to exclude critical configurations. With minimal cuts, $p_{TZ} > 4$ GeV is applied, except for $M_{\ell\ell} < 0.4M_Z$, where $p_{TZ} > 7$ GeV is used. An update of `GG2ZZ` that requires no technical cuts is in preparation.

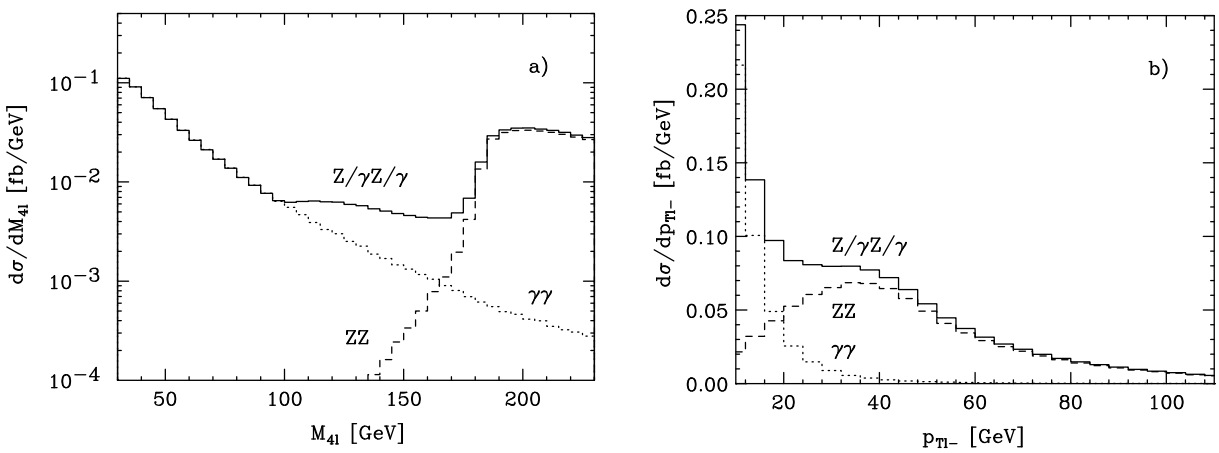

Fig. 10: Distributions in the $\ell\bar{\ell}\ell'\bar{\ell}'$ invariant mass M_{4l} (a) and the transverse momentum $p_{T\ell^-}$ of the negatively charged lepton (b) for the gluon scattering process $gg \to Z^*(\gamma^*)Z^*(\gamma^*) \to \ell\bar{\ell}\ell'\bar{\ell}'$ at the LHC with ZZ contributions only (dashed), $\gamma\gamma$ contributions only (dotted) and all contributions (solid). Input parameters and minimal set of cuts as defined in the main text.

of this work. This work was supported by the BMBF and DFG, Germany (contracts 05HT1WWA2 and BI 1050/2).

7. GLUON- INDUCED Z^*Z^* BACKGROUND SIMULATION FOR HIGGS BOSON SEARCH [9]

The contribution of the $gg \to Z^*(\gamma^*)Z^*(\gamma^*) \to \ell\bar{\ell}\ell'\bar{\ell}'$ process to the total $pp \to Z^*(\gamma^*)Z^*(\gamma^*) \to \ell\bar{\ell}\ell'\bar{\ell}'$ production cross section has been evaluated after the application of the selection cuts adopted for the Higgs boson search through the $H \to ZZ \to 2e2\mu$ decay channel in the CMS experiment [171]. The minimal set of kinematical cuts needed to maximize the discovery significance has been used: upper thresholds for the transverse momenta ($p_{T\ell}$) of the four produced leptons; upper threshold on the highest reconstructed $M_{\ell\bar{\ell}}$; lower threshold on the lowest reconstructed $M_{\ell\bar{\ell}}$; upper and lower thresholds on the $M_{4\ell}$. The values of the selection cuts are mass dependent, optimized for different Higgs boson mass scenarios, from 120 GeV to 500 GeV. The selection procedure and the cut values are described in details in Ref. [171]. A sample of 9k $gg \to Z^*(\gamma^*)Z^*(\gamma^*) \to \ell\bar{\ell}\ell'\bar{\ell}'$ events has been generated at parton level using the generator program `GG2ZZ` here presented. For the simulation of the shower evolution we have interfaced the generated parton-level events to the PYTHIA Monte Carlo generator [172]. In order to increase the event statistics in the kinematical region of interest the following set of pre-selection cuts has been used: $p_{T\ell} > 5$ GeV, $|\eta_\ell| < 2.5$, $\mathrm{M}_{\ell\bar{\ell}} > 5$ GeV. The cross section for the selected events is 2.8 fb. We compare the gluon induced contribution with 70k $q\bar{q} \to Z^*(\gamma^*)Z^*(\gamma^*) \to \ell\bar{\ell}\ell'\bar{\ell}'$ events generated with the MadGraph LO Monte Carlo generator [173]. The LO cross section of this process is 27.67 fb, where the same set of pre-selection cuts has been applied. In Fig 11 we compare the distribution of the invariant mass (M_{4l}) of the four leptons produced in the gluon-gluon and in the quark scattering processes respectively. The peak at $M_{4l} \sim M_Z$ in the $q\bar{q}$ distribution is due to the s-channel production process, that gives the main contribution to the cross section in the M_{4l} mass region below and near M_Z. Since the Higgs mass region below 114.4 GeV has been excluded by the LEP data [4], almost all the events produced by the s-channel process are removed by the selection cuts adopted in the Higgs boson search analyses. The effect of the mass dependent selection cuts on the M_{4l} distribution is shown in Fig 12. The different curves correspond to the $gg \to Z^*(\gamma^*)Z^*(\gamma^*) \to \ell\bar{\ell}\ell'\bar{\ell}'$ events selected after the pre-selection cuts (solid curve) and for a few Higgs boson mass scenarios (dashed curves), when only

[9] Contributed by: D. Giordano

the cuts on the four leptons transverse momenta and on the di-lepton invariant masses ($M_{\ell\bar{\ell}}$, $M_{\ell'\bar{\ell}'}$) have been applied. The photon contribution is strongly suppressed for the Higgs boson search above $2M_Z$.

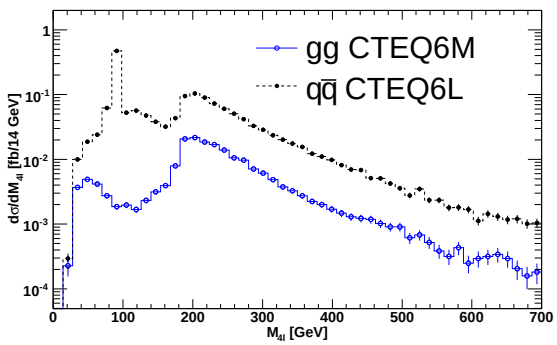

Fig. 11: Distribution in the $\ell\bar{\ell}\ell'\bar{\ell}'$ invariant mass, $M_{4\ell}$, for the gluon scattering process (solid) and the quark scattering process (dashed) of $pp \to ZZ \to \ell\bar{\ell}\ell'\bar{\ell}'$ at the LHC, after applying pre-selection cuts.

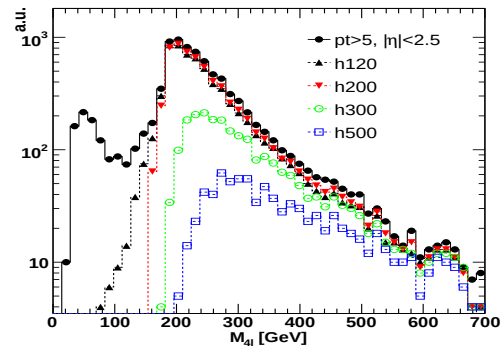

Fig. 12: Selected distributions in the $\ell\bar{\ell}\ell'\bar{\ell}'$ invariant mass, $M_{4\ell}$, for the gluon scattering process at the LHC, obteined applying the pre-selection cuts (solid) and the set of selection cuts optimized for the Higgs boson search in different mass scenarios from 120 GeV to 500 GeV.

The contribution of the gluon scattering to the ZZ cross section is reported in Fig 13, in terms of the ratio of the selected $gg \to Z^*(\gamma^*)Z^*(\gamma^*) \to \ell\bar{\ell}\ell'\bar{\ell}'$ events respect to the LO $q\bar{q} \to Z^*(\gamma^*)Z^*(\gamma^*) \to \ell\bar{\ell}\ell'\bar{\ell}'$ selected events (solid square markers). The correction increases approximately linearly from 3% to 24% in the M_{4l} region between 120 GeV and 200 GeV, and it is quite uniform, around $\sim 24\%$, in the M_{4l} region above 200 GeV. Superimposing to the graphic the ratio of the distributions shown in Fig 11 (dashed curve), where only the pre-selection cuts were applied, we observe that the gluon induced contibution is enhanced by the selection cuts, especially in the mass region above 200 GeV. The empty round markers in Fig 13 show the gg contribution respect to the $q\bar{q}$ process calculated at the NLO. The mass dependent NLO k-factor evaluated in Ref [174] has been used to rescale the quark scattering cross section at the NLO. The gluon-gluon contribution is reduced to 18% in the M_{4l} region above 200 GeV, a value compatible with our previous evaluation.

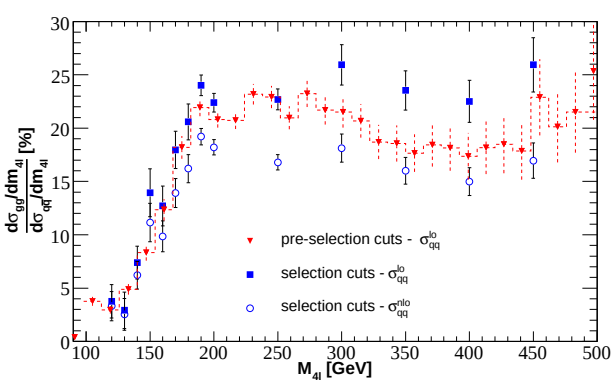

Fig. 13: Contribution of the gluon-induced background $gg \to Z^*(\gamma^*)Z^*(\gamma^*) \to \ell\bar{\ell}\ell'\bar{\ell}'$ respect to the $q\bar{q} \to Z^*(\gamma^*)Z^*(\gamma^*) \to \ell\bar{\ell}\ell'\bar{\ell}'$ process, as a function of the four leptons invariant mass $M_{4\ell}$, after application of the pre-selection cuts only (dashed) and all selection cuts (other two curves). The reference cross section of the $q\bar{q}$ scattering is evaluated at the LO (solid markers) and at the NLO (empty markers).

8. THE METHODS FOR THE CENTRAL RAPIDITY GAP SELECTION IN THE VECTOR BOSON FUSION SEARCHES IN CMS [10]

8.1 Introduction

In the VBF Higgs boson searches at LHC a selection of the events with the central rapidity gap between the two tagging jets is aimed to reduce the QCD Z+jets and other backgrounds like W+jets and $t\bar{t}$ while keep a high efficiency for the Higgs boson signal from the VBF production, $VV \to H$. The central jet veto was proposed and used in the first VBF Higgs boson analyses [113, 175] (see also references in it) and exploited in the recent, published ATLAS and CMS analyses [108, 176]. The central calorimeter jet veto technique is suffering from the pile-up and the electronic noise in the calorimeters which could create the fake jets. The method of the reduction of the fake calorimeter jets using the information from the event vertex and the tracks was proposed in [177] and successfully used in the CMS analyses [176, 178].

We consider three methods to perform the hadron activity veto in the central rapidity region: the (traditional) central calorimeter jet veto (CJV), the track counting veto (TCV) and the veto on jets made from the tracks only (TJV). The idea of the track counting veto is inspired by the paper [179] where it was proposed to distinguish between the gluon and vector boson fusion processes for the Higgs boson production. The performance of methods is compared in terms of the signal efficiency and the QCD Z+jets background rejection.

8.2 Studies at generator level

The QCD Z+jets events were generated using the ALPGEN [180] generator with the MLM prescription for jet-parton matching [181, 182] in the PYTHIA6.4 shower generation [183]. The details on the ALPGEN generation and soft VBF preselections at the generator level can be found in [176].

The final VBF selections similar to the ones used in the full simulation analysis [176] were applied to the PYTHIA particle level jets. An event must have at least two leading E_T jets reconstructed with a cone algorithm (cone size 0.5) that satisfy the following requirements:

1. $E_T^j > 20$ GeV
2. $|\eta^j| < 4.5$
3. $M_{j1j2} > 1000$ GeV
4. $|\Delta\eta^{j1j2}| > 4.2$
5. $\eta^{j1} \times \eta^{j2} < 0$.

where j1 and j2 are two leading E_T jets ordered in E_T.

The performance of the two methods, CJV and TCV was compared. The CJV requires to reject events with a third jet that satisfies

- $E_T^{j3} > 20$ GeV
- $\eta^{j\ min} + 0.5 < \eta^{j3} < \eta^{j\ max} - 0.5$,

where $\eta^{j\ min}$ and $\eta^{j\ max}$ are the minimum and maximum η of the two leading jets (j1 and j2). The TCV requires to reject events with a certain number of "tracks" (charged particles) within the tracker acceptance region, $|\eta|$ <2.4 that satisfies

- $p_T^{track} > p_T^{cut}$ GeV/c
- $\eta^{j\ min} + 0.5 < \eta^{track} < \eta^{j\ max} - 0.5$,

The effect of multiple parton interactions generated with Tune DWT [184] on the track counting veto was studied.

Fig. 14 shows the number of charged particles within the tracker acceptance and between the two tagging jets ($\eta^{j\ min} + 0.5 < \eta^{track} < \eta^{j\ max} - 0.5$) with $p_T > 0$ GeV/c (left plot), > 1 GeV/c (middle

[10] Contributed by: M. Vázquez Acosta, S. Greder, A. Nikitenko, and M. Takahashi

plot) and $>$ 2 GeV/c (right plot) for the signal (solid line) and the QCD Z+jets background (dashed line). The multiple parton interactions were switched off in PYTHIA. One can see a clear difference

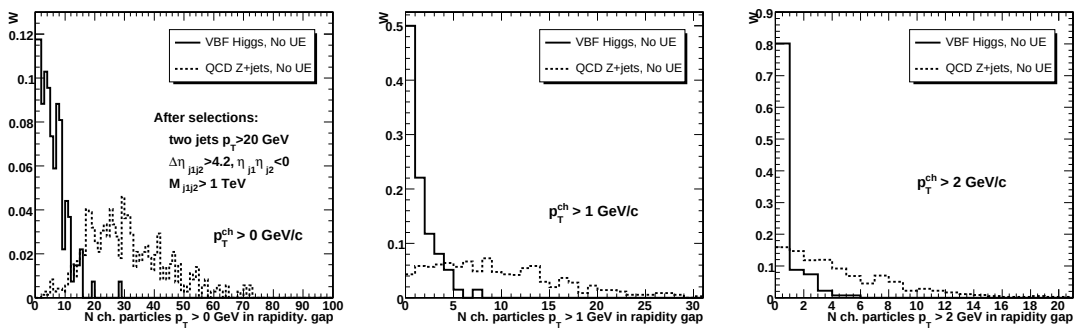

Fig. 14: The number of charged particles within the tracker acceptance and between two tagging jets ($\eta^{j\ min} + 0.5 < \eta^{track} < \eta^{j\ max} - 0.5$) with $p_T > 0$ GeV/c (left plot), > 1 GeV/c (middle plot) and > 2 GeV/c (right plot) for the signal (solid line) and the QCD Z+jets background (dashed line). The multiple parton interactions are switched off in PYTHIA.

between the signal and the QCD Z+jets background distributions. This difference, however is spoiled when the multiple parton interactions are switched on. Fig. 15 shows the same distributions as in Fig. 14 but with the multiple parton interactions included in the generation. With no cut of the charged particle p_T applied, it is not possible to distinguish between the signal and the background. The cut on the "track" p_T removes charged particles from the underlying event, thus giving the selection power for the TCV method. With the cut p_T^{cut}=2 GeV/c the efficiency for the signal $VV \rightarrow H$ (M_H=120 GeV) is $\simeq$ 0.8 and for the QCD Z+jets background is 0.54. For the same $\simeq$ 80 % signal efficiency, the central

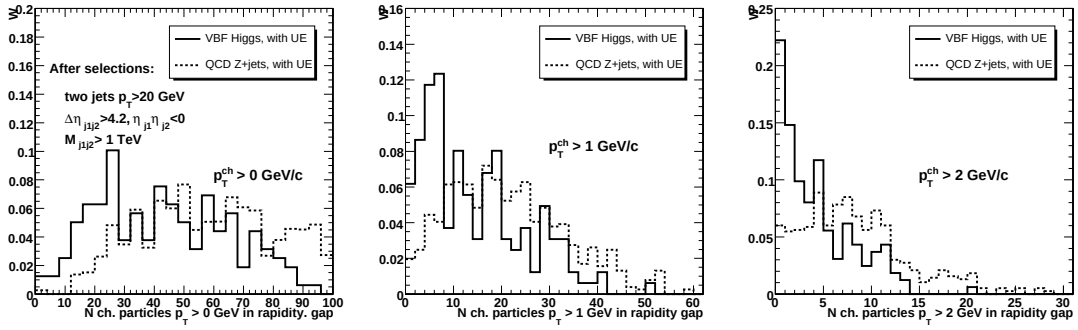

Fig. 15: The number of charged particles within the tracker acceptance and between two tagging jets ($\eta^{j\ min} + 0.5 < \eta^{track} < \eta^{j\ max} - 0.5$) with $p_T > 0$ GeV/c (left plot), > 1 GeV/c (middle plot) and > 2 GeV/c (right plot) for the signal (solid line) and the QCD Z+jets background (dashed line). The multiple parton interactions generated with Tune DWT are switched on in PYTHIA.

jet veto efficiency for the background is smaller, 0.44, thus leading to the conclusion that at the particle level simulation the central jet veto provides the better performance than the track counting veto. The final conclusion, however should be resulting from the full detector simulation including the detector and reconstruction effects, like fake jet contribution from the pile up and the electronic noise, the track and jet reconstruction inefficiency.

8.3 Studies with the full detector simulation

The fully simulated datasets from the VBF Higgs boson analysis ($H \rightarrow \tau\tau \rightarrow \ell + \text{jet}$) [176] at an instantaneous luminosity $L = 2 \times 10^{33}\text{cm}^{-2}\text{s}^{-1}$ are used. The pile-up events (4.3 events per crossing) were included in the simulation. At the reconstruction level the same VBF selections 2-4 on tagging jets as described in the section 8.2 were used and the tagging jets were required to have E_T^j >40 GeV. The CJV requires to reject events with a third jet that satisfies

- $E_T^{j3} > 10$ GeV, where E_T is a raw, non calibrated energy.
- fake jet rejection parameter $\alpha^{j_3} = \sum p_T^{track}/E_T^{j_3} > 0.1$ (see [176] for details)

The TCV requires, on top of the selections mentioned in the previous section, the quality selections on the tracks: ≥ 8 hits, $\Delta Z(\text{track, vertex})$ <2 mm, $\Delta R(\text{track, jet})$ >0.5. The lepton and tracks from τ jet are not counted.

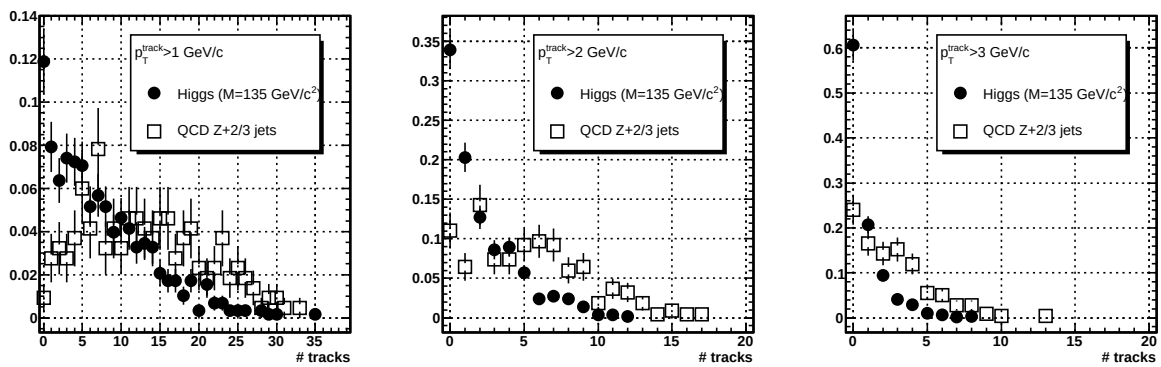

Fig. 16: Track multiplicity between the two forward tagging jets ($\eta^{j\ min} + 0.5 < \eta^{track} < \eta^{j\ max} - 0.5$) with $p_T > 1$ GeV/c (left plot), > 2 GeV/c (middle plot) and > 3 GeV/c (right plot) for the signal (full circles) and the QCD Z+jets background (open squares).

Fig. 16 shows the number of reconstructed tracks between the two forward tagging jets with $p_T >$ 1 GeV/c (left plot), > 2 GeV/c (middle plot) and > 3 GeV/c (right plot). Both the Higgs boson signal (circles) and the QCD Z+jets background (squares) can be clearly separated when applying a cut on the track multiplicity and for different track p_T thresholds. The left plot of Fig. 17 shows the performance of the algorithm, i.e the efficiency of selecting the signal versus the background. Starting from the bin 0 on the left bottom corner, the points correspond to an increasing cut on the track multiplicity and p_T up to the right top corner where 100% of events are selected. The black star indicates the performance of the central jet veto (CJV) based on calorimeter jets. One can notice that this latter achieves a good performance: 80.0$\pm$ 3.3% efficiency for the signal and 39.7$\pm$ 5.% efficiency for the backgrouind. The TCV algorithm can reach this discrimination power rejecting events with more that one track of $p_T > 3$ GeV/c. The right plot of Fig. 17 shows the ratio of the signal and the background selection efficiencies as a function of the signal efficiency. It shows that the better ratio can be achieved with the TCV at the price of losing a bit of signal. This would obviously depend on the overall tuning of the analysis. The third algorithm, the track-jet counting veto (TJV) is very similar to the TCV. Tracks are first clustered along the beam axis (Z) starting from the track with the highest p_T following the condition: $\Delta Z(\text{cluster, track})$ <2 mm. Once a z-cluster is formed, the same procedure applies again with the remaining tracks. In a second step a traditional cone jet finding method is applied with $\Delta R = 0.5$ around seed tracks (with highest p_T). These jets are thus formed solely of tracks originating from the different z-clusters. They are finally associated with the signal vertex if their z-impact parameter is within 2 mm from the lepton z-impact parameter. This method allows to refine the description of the

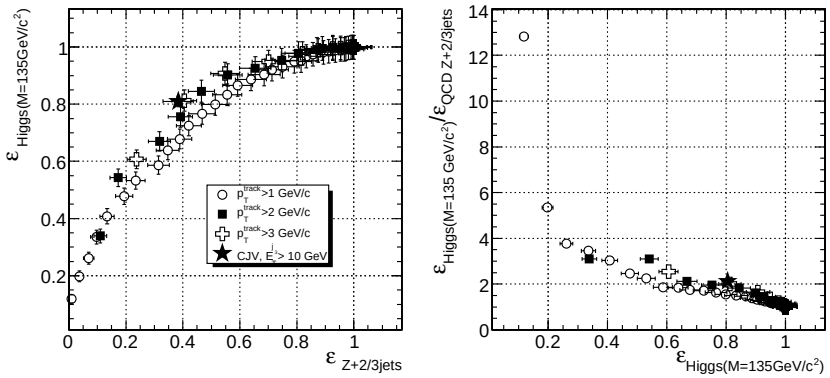

Fig. 17: The track counting veto (TCV) performances (see text) for the different p_T^{track} and track multiplicity thresholds.

hadronization process usually producing several collimated particles with respect to the more exclusive approach of the TCV algorithm. The discrimination variable are then the multiplicity and the minimum p_T of the track-jets and its constituents lying in between the two forward tagging jets. The performance of this algorithm has been found to be very close to the TCV, reaching 80% for the signal efficiency and 40% for the background when requiring no track-jet with $\Delta Z(\mathrm{track-jet,\ lepton}) <$ 2mm, $p_T^{jet} > 3$ GeV/c and with at least one track of $p_T >$0.9 GeV/c.

8.4 The efficiency measurement of the central rapidity gap selection for Z $\rightarrow \tau\tau$ background.

The efficiency of the central rapidity gap selection (CRGS) for the Z+jets, $Z \rightarrow \tau\tau$ background in the VBF $H \rightarrow \tau\tau$ search can be measured with the Z+jets, $Z \rightarrow \mu\mu$ events passed the "signal like" VBF jet selections. We estimated the expected number of such events and the statistical accuracy of the CRGS for 100 pb^{-1} of integrated luminosity. Only QCD Z+jets events were used. The events from the EWK Z+2jets production still have to be added. The fully simulated events with no pile-up were required to pass the di-muon trigger. In the off-line analysis the events with two muons $p_T >$ 10 GeV/c, $|\eta| <$2.4 isolated in the tracker were selected within the di-muon mass window 70$<$ $M_{\mu\mu}$ $<$110 GeV/c^2. The following VBF cuts relaxed for the early analysis with the first 100 pb^{-1} of the data are used. An event must have at least two leading E_T jets that satisfy the following requirements: $E_T^j >$ 40 GeV, $|\eta^j|$ $<$4.5, $\eta^{j1} \times \eta^{j2} < 0$ and:

- soft VBF selections: $M_{j1j2} > 400$ GeV/c^2, $|\Delta\eta^{j1j2}| > 2.5$
- hard VBF selections: $M_{j1j2} > 800$ GeV/c^2, $|\Delta\eta^{j1j2}| > 3.5$

The CJV used in this section requires to reject events with a third calorimeter jet that satisfies

- $E_T^{j3} > 30$ GeV, where E_T is the calibrated jet energy
- $\eta^{j\ min} + 0.5 < \eta^{j3} < \eta^{j\ max} - 0.5$,

Table 7 shows the expected number of events after selections for 100 pb^{-1} and the efficiency and the statistical accuracy of the CJV. Fig. 18 shows the distribution of $\eta^{j\ min}$ and $\eta^{j\ max}$ (left-upper plot), the η^{j3} (left-bottom plot) and the variable η_Z=η^{j3}-0.5($\eta^{j\ min} + \eta^{j\ max}$) (right plot) for 100 pb^{-1} of the "data" for one random experiment. All selections except the CJV were applied.

8.5 Conclusions

With the full detector simulation is was shown that both the central jet veto and the track counting algorithms achieve very similar performance. The robustness and the stability of the methods under a variation of the run and detector conditions will be tested with the real data using Z+jets, $Z \rightarrow \mu\mu$ events. It is believed that the track counting algorithms relying on a single sub-detector, the tracking system, would perform with a higher reliability.

Table 7: The expected number of events after selections for 100 pb^{-1} and the efficiency and the statistical accuracy of the CJV.

selections	number of events with 100 pb^{-1}	CJV efficiency
”soft” VBF	121	
”soft” VBF + CJV	61	0.50 $\pm$ 0.06
”hard” VBF	31	
”hard” VBF + CJV	11	0.35 $\pm$ 0.11

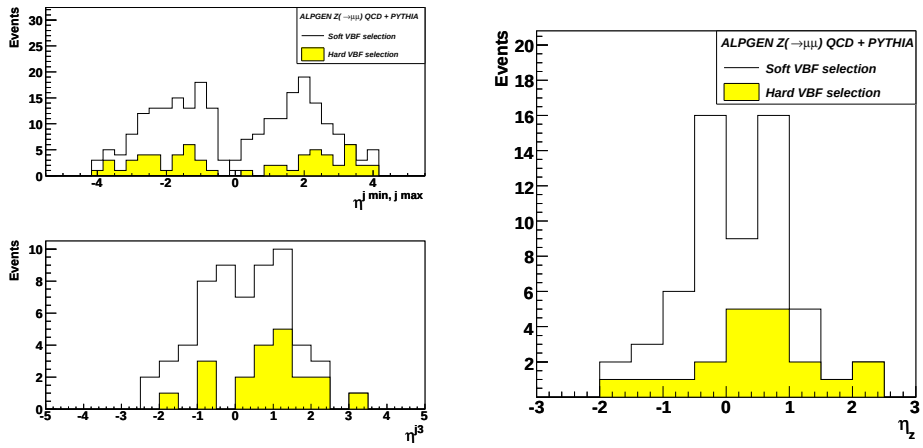

Fig. 18: The distribution of $\eta^{j\ min}$ and $\eta^{j\ max}$ (left-upper plot), the η^{j3} (left-bottom plot) and the variable η_Z=η^{j3}-0.5($\eta^{j\ min}+\eta^{j\ max}$) (right plot).All selections except the CJV were applied.

Acknowledgements

We would like to thank T. Sjostrand and V. Khoze for very useful discussions about the methods for the central rapidity gap selection. A.N. and M.V.A. would like to thank the organizers of Les Houches Workshop 2007 for the hospitality and the nice scientific atmosphere of the Workshop.

9. PRODUCTION OF A HIGGS BOSON AND A PHOTON IN VECTOR BOSON FUSION AT THE LHC [11]

9.1 Introduction

Higgs boson search is one of the main tasks of present and future collider experiments [2, 185]. At the CERN Large Hadron Collider (LHC), the Higgs boson is expected to be produced with high rate via gluon or vector-boson fusion (VBF) mechanisms and associate $W(Z)H$ production. Apart from observing the Higgs signal, it would be crucial to make at the LHC also a measurement of the $Hb\bar{b}$ coupling [8]. To this aim, Higgs production via VBF, with the Higgs boson decaying into a $b\bar{b}$ pair, plays an important role [186]. In this contribution, we consider a further process that could help in determining the $Hb\bar{b}$ coupling, that is the Higgs boson production in association with a large transverse-momentum photon (with $p_{\rm T} \gtrsim 20$ GeV) and two *forward* jets [187]

$$pp \to H\,\gamma\,jj \to b\bar{b}\,\gamma\,jj\ +X\,, \tag{11}$$

[11] Contributed by: E. Gabrielli, F. Maltoni, B. Mele, M. Moretti, F. Piccinini, and R. Pittau

m_H (GeV)	110	120	130	140
$\sigma(H\gamma jj)$ $[fb]$	67.4	64.0	60.4	56.1
$\mathcal{BR}(H \to b\bar{b})$	0.770	0.678	0.525	0.341

Table 8: Cross sections for the $H\,\gamma\,jj$ signal at LHC, for $p_{\rm T}^{\gamma} \geq 20$ GeV, $\Delta R_{\gamma j} > 0.4$, and a cut $m_{jj} > 100\,{\rm GeV}$ on the invariant mass of the final quark pair. Also shown are the Higgs boson branching ratios to $b\bar{b}$ (computed through HDECAY [188]), that are not included in the cross sections shown.

with H decaying to $b\bar{b}$, where at the parton level the final QCD parton is identified with the corresponding jet. In our study, we will not include diagrams where the photon is emitted from one of the two b-quarks, since the requirement of a large $p_{\rm T}$ photon would shift in that case the $b\bar{b}$ invariant mass outside the experimental $b\bar{b}$ mass resolution window around the Higgs mass.

There are a number of advantages in considering this QED higher-order variant of the VBF Higgs production process $pp \to H(\to b\bar{b})\,jj$. The fact that the production rate is penalized by the electromagnetic coupling is compensated by a few peculiarities of the channel in Eq. (11). First of all, the presence of an additional high $p_{\rm T}$ photon can improve the triggering efficiencies for multi-jet final states, such as those needed to select $pp \to H(\to b\bar{b})\,jj$ events. Second, there is a large gluonic component entering the partonic processes giving rise to the QCD backgrounds to the $b\bar{b}\,jj$ final state. As a consequence, the QCD backgrounds are in general much less *active* in radiating a large $p_{\rm T}$ photon with respect to the VBF signal. In addition there are dynamical effects that dramatically suppress the radiation of a central photon in the irreducible QCD background to $b\bar{b}\,\gamma\,jj$ with respect to the VBF channel. When the photon is forced to be emitted in the central rapidity region, a destructive quantum interference arises between the photon emission off the initial quark exchanging a gluon (or any other neutral vector boson) in the t channel, and the photon emission off the corresponding final quark. For the signal case of the $H\,\gamma\,jj$ production, the above mechanism of destructive interferences affects only the diagrams involving the ZZ fusion. On the other hand, in the diagrams involving WW fusion (that are responsible for the dominant part of the basic VBF $H\,jj$ cross section) the charged currents in the $qq'W$ vertices change the electric charges of the in-out partons, and consequently the interference is now additive rather than destructive. Therefore, the cross section for $H\,\gamma\,jj$ is expected to follow the usual pattern of QED corrections as far as its WW fusion component is concerned. The relative contribution of the ZZ fusion will be instead remarkably smaller than in the case of the basic VBF $H\,jj$ process.

To summarize, a measurement of the $b\bar{b}\,\gamma\,jj$ rate could lead to a combined determination of the Higgs boson couplings to b quarks and W vector bosons, with less contamination from the HZZ coupling uncertainties.

In Section 9.2, we go through the main kinematical and dynamical characteristics of the process in Eq. (11). We also discuss the features of the main QCD irreducible background. In Section 9.3, the signal rates are computed at parton level for a set of kinematical cuts that optimizes the signal/background ratio, restricting the analysis to the case of the irreducible background. In Section 9.4, the main reducible background channels are included in the analysis. Finally, in Section 9.5, we draw our conclusions.

9.2 Signal and Irreducible Background

Cross sections for the $H\,\gamma\,jj$ production at $\sqrt{S} = 14$ TeV are shown in Table 8. In order to present results as inclusive as possible only a minimal set of kinematical cuts is applied ($\Delta R_{\gamma j} > 0.4$, $p_{\rm T}^{\gamma} \geq 20$ GeV, and $m_{jj} > 100\,{\rm GeV}$). The Higgs boson branching ratios to $b\bar{b}$, which are not included in the cross section results, (computed through HDECAY [188]), are also shown. The full tree-level matrix elements for the electroweak process $pp \to H\,\gamma\,jj$ have been computed independently with ALPGEN [180], and MadEvent [173]. Details on the values of input parameters, such PDF's and scales are given in Section 9.3.

Before discussing the process in Eq. (11), it is useful to recall here the main kinematical properties of a typical VBF event, that is $pp \to H\,jj$, and the corresponding backgrounds. For the Higgs boson decaying to a $b\bar{b}$ pair, the main background to the basic VBF process comes from the QCD production of the final state $b\bar{b}jj$, whenever the $b\bar{b}jj$ kinematical characteristics approach the typical VBF configuration. By imposing a large invariant mass cut for the two-forward-jet system [i.e., $m_{jj} \gtrsim \mathcal{O}(1)$ TeV], a minimal $p_{\rm T}^j$ of a few tens GeV's, and requiring the $b\bar{b}$ invariant mass to be around m_H within the $m_{b\bar{b}}$ experimental resolution, one can obtain a signal significance ($S/\sqrt{B}$) of the order of $S/\sqrt{B} \sim 3-5$, assuming an integrated luminosity of 600 fb^{-1} [186].

Let us now consider the VBF Higgs production when a further central photon is emitted, namely $pp \to H\,\gamma\,jj$. According to the usual pattern of QED corrections, one might expect the request of a further hard photon to keep the relative weight of signal and background quite stable. Were this the case, the rates for $pp \to H\,\gamma\,jj$ and its background would be related to a $\mathcal{O}(\alpha)$ rescaling of the rates for the $H\,jj$ signal and its background, respectively, where α is the fine electromagnetic structure constant. On this basis, one would conclude that there is no advantage in considering the $H\,\gamma\,jj$ variant of the $H\,jj$ process, apart from the fact that the presence of a hard photon in the final state can improve the triggering efficiency of the detectors. However, as we explained in the introduction, this pattern does not hold in general when restricted regions of phase space are considered.

In the next section we will study this effect on a quantitative level, showing that the requirement of a further central photon gives rise to a dramatic increase (by more than one order of magnitude) in the S/B ratio, while the signal cross section roughly follows the naive QED rescaling.

9.3 Cross Sections for the Signal versus the Irreducible Background

The numerical results presented in this section have been independently obtained by the Monte Carlo event generators ALPGEN [180], and MadEvent [173]. The signal is calculated in the narrow width approximation, *i.e.* we computed the exact lowest-order matrix element for the process $pp \to H\gamma\,jj$, and then let the Higgs boson decay into a $b\bar{b}$ pair according to its branching ratio and isotropic phase space. After the decay, cuts on the $b-$quark jets are implemented. For the irreducible $pp \to b\bar{b}\gamma\,jj$ background, we computed all the matrix elements at $\mathcal{O}(\alpha_s^4\alpha)$, neglecting $\mathcal{O}(\alpha_s^2\alpha^3)$, $\mathcal{O}(\alpha_s^3\alpha^2)$, $\mathcal{O}(\alpha_s\alpha^4)$ and $\mathcal{O}(\alpha^5)$ contributions and their interference with the $\mathcal{O}(\alpha_s^4\alpha)$ contribution. We checked that this has no numerical impact on the results. The present study is limited at the parton level. A more complete simulation, that takes into account showering, hadronization and detector simulation, even if crucial for the assessment of the potential of this channel, is beyond the scope of the present contribution. As PDF's, we use the parametric form of CTEQ5L [189], and the factorization/renormalization scales are fixed at $\mu_{\rm F}^2 = \mu_{\rm R}^2 = \sum E_t^2$ and $\mu_{\rm F}^2 = \mu_{\rm R}^2 = m_H^2 + \sum E_t^2$ for the backgrounds and signal, respectively (E_t is the transverse energy of any QCD parton). The three Higgs-mass cases 120, 130 and 140 GeV are analysed.

We start by the definition of two *basic* event selections (sets 1 and 2) that differ only by the threshold on the photon transverse momentum $p_{\rm T}^\gamma$:

$$\begin{aligned}
&p_{\rm T}^j \geq 30\,{\rm GeV}, \quad p_{\rm T}^b \geq 30\,{\rm GeV}, \quad \Delta R_{ik} \geq 0.7,\\
&|\eta_\gamma| \leq 2.5, \quad |\eta_b| \leq 2.5, \quad |\eta_j| \leq 5,\\
&m_{jj} > 400\,{\rm GeV}, \quad m_H(1-10\%) \leq m_{b\bar{b}} \leq m_H(1+10\%),\\
&1)\ \ p_{\rm T}^\gamma \geq 20\,{\rm GeV},\\
&2)\ \ p_{\rm T}^\gamma \geq 30\,{\rm GeV},
\end{aligned} \tag{12}$$

where ik is any pair of partons in the final state, including the photon, and $\Delta R_{ik} = \sqrt{\Delta^2\eta_{ik} + \Delta^2\phi_{ik}}$, with η the pseudorapidity and ϕ the azimuthal angle. The cross sections for the above *basic* event selections are reported in Table 9. Before comparing the signal and the background for the $H\,\gamma\,jj$ process, we tried to optimize our event selection in Eq. (12). Indeed, the signal detectability can be

	$p_{\rm T}^{\gamma,cut}$	$m_H = 120$ GeV	$m_H = 130$ GeV	$m_H = 140$ GeV
$\sigma[H(\to b\bar{b})\gamma jj]$	20 GeV	9.3(1) fb	7.4(1) fb	4.74(7) fb
	30 GeV	6.54(7) fb	5.2(1) fb	3.31(3) fb
$\sigma[b\bar{b}\gamma jj]$	20 GeV	406(2) fb	405(4) fb	389(1) fb
	30 GeV	260.5(7) fb	257.9(6) fb	251.8(7) fb
$\sigma[H(\to b\bar{b})jj]$		727(2) fb	566(2) fb	363(1) fb
$\sigma[b\bar{b}jj]$		593.7(5) pb	550.5(5) pb	505.6(4) pb

Table 9: Cross sections for the signal and the irreducible background for the *basic* event selections in Eq. (12). Higgs production cross sections include the Higgs branching ratios to $b\bar{b}$. The signal and irreducible background production rates for the VBF process without photon are also shown.

	$p_{\rm T}^{\gamma,cut}$	$m_H = 120$ GeV	$m_H = 130$ GeV	$m_H = 140$ GeV
$\sigma[H(\to b\bar{b})\gamma jj]$	20 GeV	3.59(7) fb	2.92(4) fb	1.98(3) fb
	30 GeV	2.62(3) fb	2.10(2) fb	1.50(3) fb
$\sigma[b\bar{b}\gamma jj]$	20 GeV	33.5(1) fb	37.8(2) fb	40.2(1) fb
	30 GeV	25.7(1) fb	27.7(1) fb	28.9(2) fb
$\sigma[H(\to b\bar{b})jj]$		320(1) fb	254.8(6) fb	167.7(3) fb
$\sigma[b\bar{b}jj]$		103.4(2) pb	102.0(2) pb	98.4(2) pb

Table 10: Cross sections for the signal and the irreducible background for the *optimized* event selections of Eq. (13), added to the *basic* selection in Eq. (12). Higgs production cross sections include the Higgs branching ratios to $b\bar{b}$. The signal and irreducible background production rates for the basic VBF process are also shown.

further improved by imposing *optimized* cuts, that can be deduced by looking at the following kinematical distributions:

$$\frac{d\sigma}{dm_{jj}}, \quad \frac{d\sigma}{dp_{\rm T}^{j1}}, \quad \frac{d\sigma}{dp_{\rm T}^{b1}}, \quad \frac{d\sigma}{dm_{\gamma H}}, \quad \frac{d\sigma}{|\Delta\eta_{jj}|},$$

where $j1$ and $b1$ denote the leading $p_{\rm T}$ light jet and $b-$ jet, respectively, and $m_{\gamma H}$ is the invariant mass of the $\gamma b\bar{b}$ system. By studying the variation of the significance $S/\sqrt{B}$ as a function of the cuts on the distributions (for more details see [187]), we found an *optimized* event selection where, in addition to the *basic* cuts, we impose the following cuts

$$\begin{aligned} & m_{jj} \geq 800\,\mathrm{GeV}, \quad p_{\rm T}^{j1} \geq 60\,\mathrm{GeV}, \quad p_{\rm T}^{b1} \geq 60\,\mathrm{GeV}, \\ & |\Delta\eta_{jj}| > 4, \quad m_{\gamma H} \geq 160\,\mathrm{GeV}, \quad \Delta R_{\gamma b/\gamma j} \geq 1.2\,. \end{aligned} \tag{13}$$

With the above additional requirements, we find the cross sections reported in Table 10. One see that the requirement of the extra central photon with $p_{\rm T}^{\gamma} \gtrsim 20$ GeV in the final state involves a reduction factor of order 100 for the signal rate with respect to the final state without photon, according to the expectations of the $\mathcal{O}(\alpha)$ QED naive scaling. On the other hand, the radiative background is suppressed by a factor of about 3000 with respect to the case of no photon radiation. Finally, a summary of the statistical significances, including only the irreducible background, with an integrated luminosity of 100 fb^{-1} is given in Table 11.

9.4 Reducible Backgrounds

A complete analysis of the reducible backgrounds to the $H\,\gamma\,jj$ signal is beyond the scope of our study. However, in order to have a sensible estimate of the achievable S/B ratio and statistical significance at

	$p_{\rm T}^{\gamma,cut}$	$m_H = 120$ GeV	$m_H = 130$ GeV	$m_H = 140$ GeV
$S/\sqrt{B}\|_{H\gamma jj}$	20 GeV	2.6	2.0	1.3
$S/\sqrt{B}\|_{H\gamma jj}$	30 GeV	2.2	1.7	1.2
$S/\sqrt{B}\|_{H jj}$		3.5	2.8	1.9

Table 11: Statistical significances with the event selection of Eq. (12) and (13), with an integrated luminosity of 100 fb^{-1}. The value $\epsilon_b = 60\%$ for the $b-$tagging efficiency and a Higgs boson event reduction by $\epsilon_{b\bar{b}} \simeq 70\%$, due to the finite ($\pm 10\%$) $b\bar{b}$ mass resolution, have been assumed. Jet-tagging efficiency and photon-identification efficiency are set to 100%. Only the irreducible background is included in this analysis.

parton level, we computed with ALPGEN the cross sections, assuming $m_H = 120$ GeV and with the optimized event selection of Eq. (12) and (13), for three main potentially dangerous processes

- $pp \to \gamma + 4$ jets, where two among the light jets are fake tagged as $b-$jets;
- $pp \to b\bar{b} + 3$ jets, where one of the light jets is misidentified as a photon;
- $pp \to 5$ jets, where one of the light jets is misidentified as a photon, and two light jets are fake tagged as $b-$jets.

By including also the reducible backgrounds, the statistical significance decreases by about 14(12)% for $p_{\rm T}^{\gamma,cut} = 20(30)$ GeV) with respect to Table 11, where only the irreducible background has been considered. The most dangerous contribution to reducible backgrounds comes from $pp \to b\bar{b} + 3j$.

9.5 Conclusions

In this contribution, we studied the detectability of the Higgs boson production signal, when the Higgs boson is accompanied by a high$-p_{\rm T}$ central photon and two forward jets at the LHC. The Higgs boson decay into a $b\bar{b}$ pair is considered. We analyzed the signal, the irreducible QCD background, and main reducible backgrounds at the parton level. The presence of a photon in the final state can improve the triggering efficiencies with respect to the basic VBF Higgs production without a photon. Moreover, we find that the requirement of a central photon in addition to the typical VBF final-state topology significantly suppresses the irreducible QCD background. In particular, due to dynamical effects, the latter has rates that are lower than the expectations of the $\mathcal{O}(\alpha)$ QED naive scaling by more than an order of magnitude. As a consequence, after optimizing kinematical cuts, we obtain a statistical significance $S/\sqrt{B}$ for the $H(\to b\bar{b})\gamma\, jj$ channel that goes from around 3, if $m_H \simeq 120$ GeV, down to about 1.5, if $m_H \simeq 140$ GeV, for an integrated luminosity of 100 fb^{-1}. These significances are not far from the corresponding values for the basic $H(\to b\bar{b})\, jj$ process without a photon. The latter estimates are based on the irreducible QCD background. The impact of including a few main reducible backgrounds has found to be moderate. The same dynamical effects that are responsible for the irreducible background suppression also remarkably curb the relative contribution of the $ZZ \to H$ boson fusion diagrams with respect to the $WW \to H$ ones in the process $pp \to H(\to b\bar{b})\gamma\, jj$. As a consequence, we think that the study of the $H(\to b\bar{b})\gamma\, jj$ signal at the LHC could have a role in the determination of both the Hbb and HWW couplings.

10. THE Z PLUS MULTI-JET BACKGROUND FROM THE DOUBLE PARTON INTERACTIONS IN THE VECTOR BOSON FUSION $H \to \tau^+\tau^-$ SEARCH [12]

The Z+jets production is the dominant background obtained in the VBF $H \to \tau\tau$ searches at the LHC [108, 113, 175, 176]. We estimated an additional Z+jets background originated from double parton interactions (DPI) in a proton-proton collision when the Z boson is produced in one parton-parton interaction

[12] Contributed by: A. Nikitenko

and the QCD di-jets are produced in the second parton-parton interaction. In that case the two choices of the tagging jets are possible: (a) one tagging jet is taken from the QCD di-jet production and the second one is taken from the Drell-Yan production and (b) two tagging jets are both selected from the QCD di-jet production.

The contribution from the double-parton interaction was estimated with PYTHIA6.4 [183] at the particle level [13]. At the first step the Drell-Yan and the QCD di-jet events were generated separately in PYTHIA. The Drell-Yan production was generated with the full underlying event (UE) using Tune DWT [184], while in the QCD di-jet production the UE was switched off (MSTP(81)=0). The Drell-Yan events were generated with the di-lepton mass $m_{\ell\ell} > 70$ GeV/c^2 and the QCD di-jet events were generated with $\hat{p_T}$ >20 GeV/c. The NLO cross section 2×10^6 fb for the Drell-Yan production and the PYTHIA cross section 8.2×10^{11} fb for QCD di-jet production were used in the estimates presented. At the second step two events (Drell-Yan and QCD di-jets) were mixed together and analyzed as one event. Jets were found at the particle level by the simple cone algorithm (cone size 0.5) implemented in the PYTHIA PYCELL routine.

The cross section for the double parton interactions was evaluated with the factorization formula

$$\sigma_{A,B} \; = \; \frac{m}{2} \, \frac{\sigma_A \times \sigma_B}{\sigma_{eff}}, \tag{14}$$

where m=1, for indistinguishable parton processes and m=2 for distinguishable parton processes (in our case we use m=2). In the experimental study of double parton collisions CDF quotes σ_{eff}=14.5 mb [190]. For LHC energy we use currently the value σ_{eff}=20 mb [14]. It gives the $\sigma_{A,D}$=8.2×10^4 fb (A=Drell-Yan, B=QCD di-jets). More pessimistic value of 12 mb [15] will double our estimates of the Z+jets background from the double parton interactions. The longitudinal correlations in the double-parton structure functions neglected in the above formula can have a sizable effect at the LHC [191,192].

We compare the Z+jets background from the double parton collisions with the "normal" QCD Z+jets background from one parton-parton collision. It was generated using the ALPGEN [180] generator with the MLM prescription for jet-parton matching [181,182] at the PYTHIA6.4 shower simulation. We generated $\ell\ell$+2jets exclusive and $\ell\ell$+3 jets inclusive samples with the ALPGEN settings: $m_{\ell\ell} >$ 70 GeV/c^2, p_T^j >20 GeV/c, $|\eta_j| < 5$, $\Delta R_{jj} > 0.5$. The user "soft" VBF pre-selections in ALPGEN generation were: $\Delta\eta_{j1,j2}$ >4, $\eta_{j1} \times \eta_{j2}$ <0, M_{j1j2} >600 GeV/c^2, where j1 and j2 are two leading p_T partons ordered in p_T. The parameters for MLM jet-parton matching were: E_T^{clus}=20 GeV, R^{clus}=0.5 and $\eta^{cl\ max}$ =5.0.

The VBF selections similar to that were used in a full simulation analysis [176] (except cut on E_T of the tagging jets, which is lower here) were applied to the PYTHIA particle level jets. An event must have at least two leading E_T jets reconstructed with a cone algorithm (cone size 0.5) that satisfy the following requirements:

- $E_T^j > 20$ GeV
- $\eta^j \; < \; 5.0$
- $M_{j1j2} > 1000$ GeV
- $|\Delta\eta^{j1j2}| > 4.2$
- $\eta^{j1} \times \eta^{j2} < 0$.

where j1 and j2 are two leading E_T jets ordered in E_T. The double parton scattering events where the two leading jets were both originated from the Drell-Yan production (the fraction of such events is $\simeq$ 20%) were excluded from the consideration to avoid the double counting with "normal" QCD Z+jets background.

[13] The recipe was kindly provided by T. Sjostrand. The possibility to generate two hard processes in the DPI is realized recently in PYTHIA8.

[14] Private communication with T. Sjostrand.

[15] Private communication with D. Treleani.

Table 12 shows the initial cross sections (in fb) for the Z+jets background from one and two parton-parton interactions and cross sections after the VBF cuts. After selections the contribution from

Table 12: The initial cross sections (in fb) for the Z+jets background from one and two parton-parton interactions and cross sections after the VBF cuts.

interaction	one parton-parton		two parton-parton	
process	exclusive $\ell\ell$+2j	inclusive $\ell\ell$+3j	Drell-Yan	QCD di-jets
no cuts	1.0×10^3	2.0×10^3	8.2×10^4	
≥ 2 jets, $E_T^j > 20$ GeV			4.0×10^4	
$\Delta\eta_{j1,j2}$ >4.2, $\eta_{j1}\times\eta_{j2}$ <0	2.4×10^2	5.3×10^2	5.0×10^3	
M_{j1j2} >1000 GeV/c^2			3.2×10^2	

the double parton interactions is $\simeq$ 40% (320 fb) of the "normal" Z+jets background from the one parton-parton interactions (770 fb). Fig. 19 (left plot) shows an angle in the transverse plane between two tagging jets ($\Delta\varphi_{j1j2}$) for the Z+jets backgrounds and the signal $VV \to H$. All distributions are normalized to unit. We have obtained that the fraction of the DPI events when the one tagging jet is

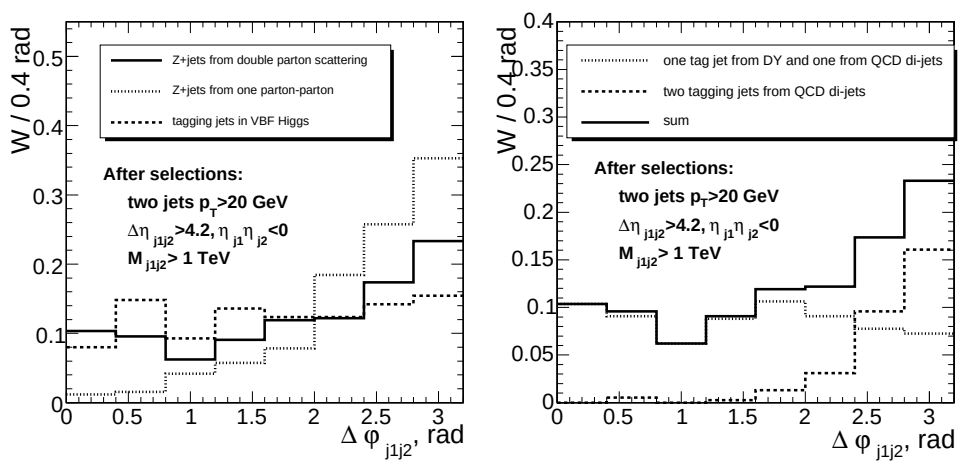

Fig. 19: Left plot: the angle in the transverse plane between two tagging jet for Z+jets backgrounds and the signal $VV \to H$. Right plot: the angle in the transverse plane between two tagging jet for Z+jets background from the DPI for the cases (a), (b) and total (see the text). All distributions are normalized to unit.

selected from the Drell-Yan and another from the QCD di-jet production (case (a)) is $\simeq$ 70%; in the rest 30% of the DPI events the both two tagging jets are selected from the QCD di-jet production (case (b)). Fig. 19 (right plot) shows the $\Delta\varphi_{j1j2}$ distributions for the cases (a) and (b) separately as well as their sum (the same curve as in Fig. 19 (left plot)). One can see that in the case (a), as expected there is no any correlations between two tagging jets, while in the case (b) they are forming the back-to-back configuration.

Fig. 20 (left plot) shows the transverse energy of the tagging jets from the Z+jets backgrounds and the signal $VV \to H$. One can see that the Z+jets background from the DPI can be largely suppressed with the cut on the tagging jet energy E_T^j >40 GeV. This cut was used in the full simulation analysis [176]. After applying this selection the cross section of the Z+jets from the DPI is $\simeq$ 100 fb and the cross section of the "normal" Z+jets background is $\simeq$700 fb, thus the relative contribution from the

DPI is reduced to $\simeq$ 15 %. The further reduction of the relative Z+jets contribution from the DPI is expected when the cuts on the momentum of the lepton (from $\tau \to \ell\nu\nu$ decay) and the hadronic τ jet (from $\tau \to \mathrm{hadrons}\ \nu$ decay) will be applied. It is due to the momentum of the Z boson from the DPI is softer that the one from the "normal" Z+jets production. It is shown in Fig. 20 (right plot) where the distributions of p_T^Z from DPI and the "normal" Z+jets production are normalized on the expected cross sections after the VBF cuts.

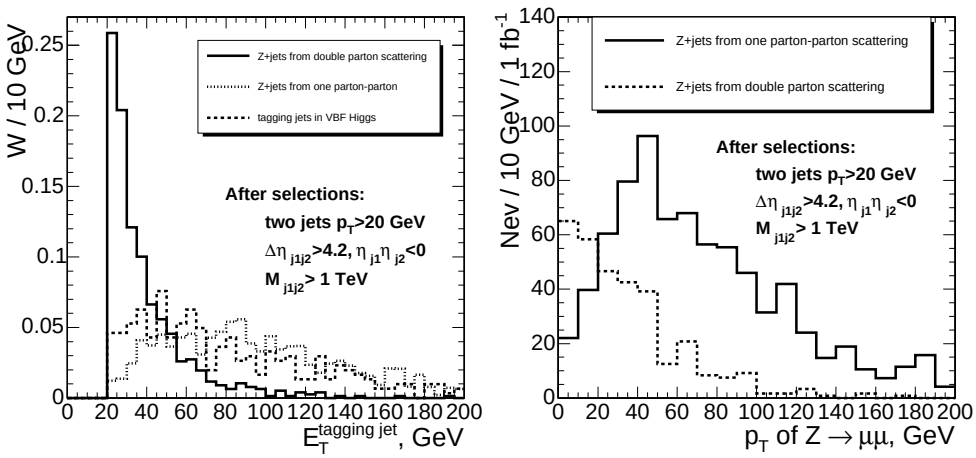

Fig. 20: Left plot: the transverse energy of the tagging jets from the Z+jets backgrounds and the signal $VV \to H$; distributions are normalized to unit. Right plot: the distributions of the Z boson transverse momentum p_T^Z from the DPI and the "normal" Z+jets production are normalized on the expected cross sections after the VBF cuts.

It is important to control and measure the Z+jets background from the double parton interactions. The possibility of the usage of the Z+2jets, Z$\to$ $\mu\mu$ events with the VBF jet selections and looking at the unbalance in $\overrightarrow{p}_T$ between the Z boson and the jets is under investigation.

10.1 Conclusion

The Z+jets background from the double parton interaction was estimated at the particle level to be less than 15% of the "normal" QCD Z+jets background in the VBF $H \to \tau\tau$ searches at LHC after the experimental like event selections and assuming the σ_{eff}=20 mb in the factorization formula. The fraction of the DPI events when the one tagging jet is selected from the Drell-Yan and another from the QCD di-jet production is $\simeq$ 70% while in the rest 30% of the DPI events the both two tagging jets are selected from the QCD di-jet production.

Acknowledgements

I would like to thank T. Sjostrand, P. Scands, D. Zeppenfeld and A. Snigirev for very useful discussions and organizers of Les Houches Workshop 2007 for the warm hospitality and the friendly and stimulating atmosphere.

Part III

MSSM HIGGS BOSONS

11. SUSY–QCD CORRECTIONS TO SQUARK LOOPS IN GLUON FUSION TO HIGGS BOSONS [16]

11.1 Introduction

In the MSSM 2 Higgs doublets are introduced to generate masses of up and down type quarks. After electroweak symmetry breaking this leads to five physical Higgs particles, two light CP-even, h, H, one CP-odd, A, and two charged $H^{\pm}$. At tree level the MSSM Higgs sector can be described by 2 independent parameters, usually chosen as the pseudoscalar mass M_A, and the ratio of the 2 vacuum expectation values $\mathrm{tg}\beta = v_2/v_1$. The MSSM Higgs couplings to quarks are modified such that the couplings to down(up)-type quarks rise(decrease) with $\mathrm{tg}\beta$. The main neutral Higgs production at the Tevatron and LHC proceeds via gg fusion. The next-to-leading order (NLO) QCD corrections to this process have been known for a long time [11, 193] including the full quark mass dependence. They turn out to be important, increasing the cross section by up to 100%. Next-to-next-to leading order (NNLO) corrections, calculated in the large quark mass limit only [15–17, 194, 195], add another 20-30% and next-to-next-to-next-to leading order (NNNLO) corrections have been estimated [19, 196, 197], indicating improved perturbative convergence. NLO corrections to squark loops have been known so far only in the heavy squark mass limit [198], and the full SUSY-QCD corrections have been obtained for heavy SUSY masses [25–27, 199]. As a first step to a full SUSY-QCD result we present the QCD corrections to squark loops including the full squark and Higgs mass dependences [28].

11.2 NLO QCD Corrections

For our calculation of the pure QCD corrections to squark loops we need a modified MSSM Lagrangian which separates the gluon and gluino contributions in a renormalizeable way. In this work we do not take into account the self-interaction among squarks, and the required Lagrangian is then given by

$$\begin{aligned}\mathcal{L} &= -\frac{1}{4}G^{a\mu\nu}G^a_{\mu\nu} - \frac{1}{4}F^{\mu\nu}F_{\mu\nu} + \frac{1}{2}\left[(\partial_\mu\mathcal{H})^2 - M^2_{\mathcal{H}}\mathcal{H}^2\right] \\ &+ \sum_Q \left[\bar{Q}(i\not{D} - m_Q)Q - g^{\mathcal{H}}_Q\frac{m_Q}{v}\bar{Q}Q\mathcal{H}\right] + \sum_{\tilde{Q}}\left[|D_\mu\tilde{Q}|^2 - m^2_{\tilde{Q}}|\tilde{Q}|^2 - g^{\mathcal{H}}_{\tilde{Q}}\frac{m^2_{\tilde{Q}}}{v}|\tilde{Q}|^2\mathcal{H}\right]\end{aligned} \tag{15}$$

with the covariant derivative $D_\mu = \partial_\mu + ig_sG^a_\mu T^a + ieA_\mu\mathcal{Q}$. Here $G^a_{\mu\nu}$ denotes the gluon field strength tensor and G^a_μ the gluon field accompanied by the color $SU(3)$ generators T^a $(a = 1, \ldots, 8)$, while $F_{\mu\nu}$ is the photon field strength tensor and A_μ the photon field associated by the electric charge operator $\mathcal{Q}$. The Higgs field $\mathcal{H}$ represents generically either the light scalar h or the heavy scalar H Higgs boson of the MSSM[17]. Since we do not take into account gluino exchange contributions, the coefficients $g^{\mathcal{H}}_Q$ and $g^{\mathcal{H}}_{\tilde{Q}}$ are not renormalized, thus leading to a renormalizeable model with strongly interacting scalars $\tilde{Q}$. Gluino corrections are expected to be small [25–27, 199].

For our numerical results we choose the gluophobic Higgs scenario [200] which maximizes the destructive interference effects between top and stop loops in the light Higgs coupling to gluons. It is defined by the MSSM parameters [$m_t = 174.3$ GeV] $M_{SUSY} = 350$ GeV, $\mu = M_2 = 300$ GeV,

[16] Contributed by: M. Mühlleitner and M. Spira

[17] Since there are no squark loop contributions to the pseudoscalar Higgs boson couplings to photons and gluons at leading order (LO), in this paper we will only deal with the scalar Higgs bosons h, H.

$X_t = A_t - \mu/\mathrm{tg}\beta = -770$ GeV, $A_b = A_t$ and $m_{\tilde{g}} = 500$ GeV. The squark masses are given by

$$\begin{aligned} \mathrm{tg}\beta = 3: \quad m_{\tilde{t}_1} &= 156 \text{ GeV} \\ m_{\tilde{t}_2} &= 517 \text{ GeV} \\ m_{\tilde{b}_1} &= 346 \text{ GeV} \\ m_{\tilde{b}_2} &= 358 \text{ GeV} \end{aligned} \qquad \begin{aligned} \mathrm{tg}\beta = 30: \quad m_{\tilde{t}_1} &= 155 \text{ GeV} \\ m_{\tilde{t}_2} &= 516 \text{ GeV} \\ m_{\tilde{b}_1} &= 314 \text{ GeV} \\ m_{\tilde{b}_2} &= 388 \text{ GeV}\,. \end{aligned} \tag{16}$$

The results of this work look similar in other scenarios, whenever the squark masses are of the order of the top mass, or the Higgs mass reaches values beyond the corresponding squark-antisquark threshold.

11.21 Scalar Higgs couplings to photons

The leading order photonic Higgs couplings are mediated by top, bottom and W boson loops, with significant contributions from squark loops for stop and sbottom masses below ~ 400 GeV [2, 11, 115, 193, 201–203]. The reverse processes $\gamma\gamma \to h, H$ play an important role for the MSSM Higgs boson searches at a photon collider [204–210]. The two-loop diagrams of the QCD corrections to squark loops lead to 5-dimensional Feynman parameter integrals. We have reduced these integrals in one calculation to 1-dimensional integrals which have been integrated numerically. A second calculation has solved the integrals purely numerically. The two calculations agree within integration errors. In order to improve the perturbative behaviour of the squark loops they have been expressed in terms of the running squark masses $m_{\tilde{Q}}(M_{\mathcal{H}}/2)$, which are related to the pole masses $M_{\tilde{Q}}$ via $m_{\tilde{Q}}(\mu) = M_{\tilde{Q}}(\alpha_s(\mu)/\alpha_s(M_{\tilde{Q}}))^{6/\beta_0}$ where $\beta_0 = 33 - 2N_F$ with $N_F = 5$ light flavors. Their scale is identified with $\mu = M_{\mathcal{H}}/2$ within the photonic decay mode thus insuring a proper definition of the $\tilde{Q}\bar{\tilde{Q}}$ thresholds $M_{\mathcal{H}} = 2M_{\tilde{Q}}$. The LO scale dependence of the squark masses due to light particle contributions has been taken into account.

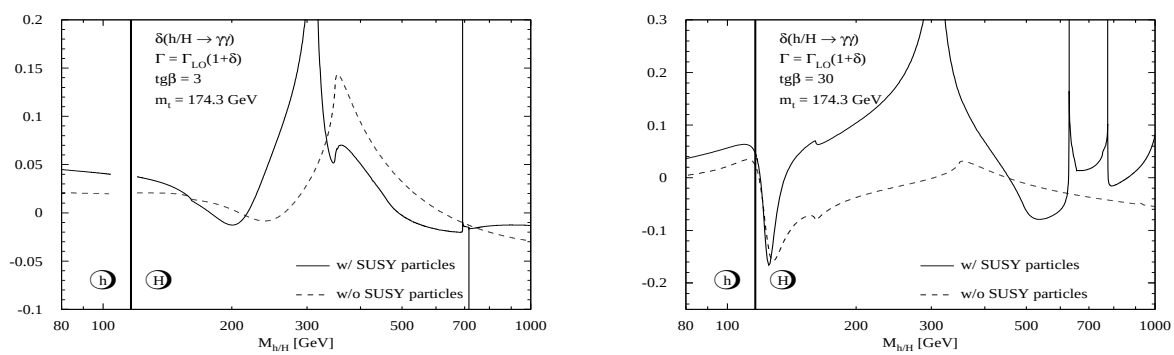

Fig. 21: *Relative QCD corrections to the scalar MSSM Higgs decay widths to two photons for* $\mathrm{tg}\beta = 3$ *and 30. The full curves include all loop contributions while in the dashed lines the SUSY contributions are omitted. The kinks and spikes correspond to the* $WW, \tilde{t}_1\bar{\tilde{t}}_1, t\bar{t}, \tilde{b}_1\bar{\tilde{b}}_1, \tilde{\tau}_1\bar{\tilde{\tau}}_1, \tilde{\tau}_2\bar{\tilde{\tau}}_2$ *and* $\tilde{b}_2\bar{\tilde{b}}_2$ *thresholds in consecutive order with rising Higgs mass.*

Fig.21 shows the relative QCD corrections to the photonic Higgs decay widths for the two cases, in which SUSY particles have been taken into account or not. The spikes which appear at the $\tilde{Q}\bar{\tilde{Q}}$ thresholds are due to singularities originating from Coulomb singularities at the threshold since $\tilde{Q}\bar{\tilde{Q}}$ pairs can form 0^{++} states. This behaviour can be derived quantitatively from the Sommerfeld rescattering corrections, and we checked explicitly that this agrees with our numerical results. As can be inferred from Fig.21 the QCD corrections reach a size of 10–20% for moderate and large Higgs masses apart from the threshold regions, where the perturbative results are unreliable due to the Coulomb singularities. At a $\gamma\gamma$ collider the photon fusion cross section can be measured with few per cent accuracy, and therefore these corrections have to be taken into account properly. The size of the QCD corrections with and without SUSY particle loops is of the same order of magnitude, but they can be of opposite sign.

Fig.22, in which the ratio of the fully massive photonic decay width at NLO $\Gamma(h/H \to \gamma\gamma)$ and the NLO width with the relative QCD corrections in the heavy squark mass limit Γ_∞ is plotted, quantifies the size of the squark mass effects beyond the heavy squark mass limit in the relative QCD corrections.

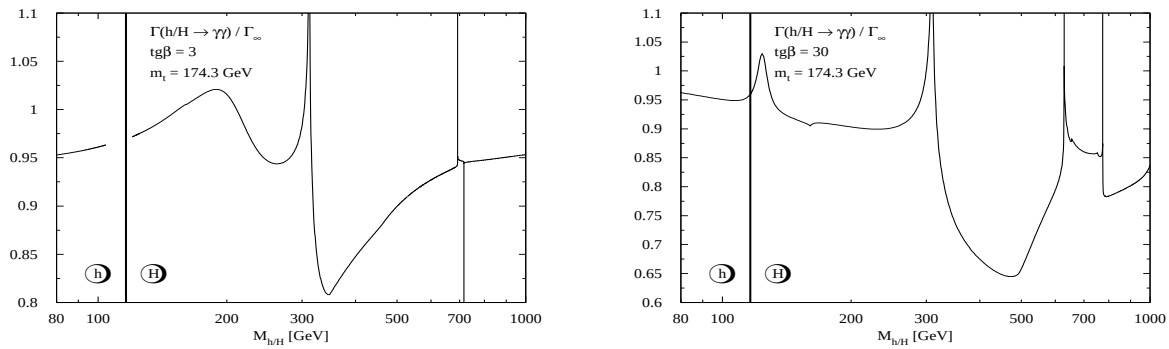

Fig. 22: *Ratio of the QCD corrected partial decay widths of the scalar MSSM Higgs bosons to two photons including the full squark mass dependence and those obtained by taking the relative QCD corrections to the squark loops in the heavy mass limit as functions of the corresponding Higgs masses for* $\mathrm{tg}\beta = 3$ *and 30.*

(The full squark mass dependence in the LO width has been kept in both expressions.) With a size of up to $\sim 30\%$ the squark mass effects are larger than the expected experimental uncertainty in the measurement of the Higgs production in $\gamma\gamma$ fusion and hence have to be taken into account in realistic analyses.

11.22 Gluon Fusion

The gluon fusion processes $gg \to h, H$ are mediated by quark and squark triangle loops with the latter contributing significantly for squark masses below ~ 400 GeV. The NLO QCD corrections consist of virtual two-loop corrections and the real corrections from the radiation processes, $gg \to gh/H$, $gq \to qh/H$ and $q\bar{q} \to gh/H$. The strong coupling constant α_s has been renormalized in the $\overline{\mathrm{MS}}$ scheme, with the top quark and squark contributions decoupled from the scale dependence, and the quark and squark masses in the on-shell scheme. The parton densities are defined in the $\overline{\mathrm{MS}}$ scheme with five active flavors, i.e. the top quark and the squarks are not included in the factorization scale dependence.

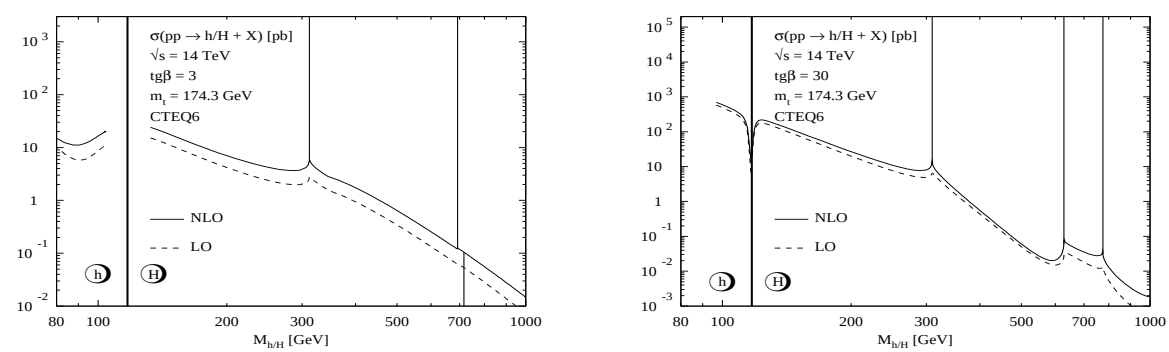

Fig. 23: *Production cross sections of the scalar MSSM Higgs bosons via gluon fusion as functions of the corresponding Higgs masses for* $\mathrm{tg}\beta = 3$ *and 30. The full curves include the QCD corrections, while the dashed lines correspond to the LO predictions. The kinks and spikes correspond to the* $\tilde{t}_1\bar{\tilde{t}}_1, \tilde{b}_1\bar{\tilde{b}}_1$ *and* $\tilde{b}_2\bar{\tilde{b}}_2$ *thresholds in consecutive order with rising Higgs mass.*

Fig. 23 shows the LO and NLO cross sections. The QCD corrections increase the gluon fusion cross sections by 10–100% and are significantly larger in regions of large destructive interferences between quark and squark loops. The corrections are of very similar size for the quark and squark loops individually. In spite of the large corrections the scale dependence is reduced from about 50% at LO to $\sim 20\%$ at NLO thus indicating a significant stabilization of the theoretical predictions. Based on this and the approximate NNLO and NNNLO results in the limit of heavy squarks and top quarks the residual theoretical uncertainties of our NLO results can be estimated to less than about 20%. The spikes at the $\tilde{Q}\bar{\tilde{Q}}$ thresholds are Coulomb singularities due to the formation of 0^{++} states.

Fig. 24, which shows the ratios of the NLO cross sections including the full mass dependence

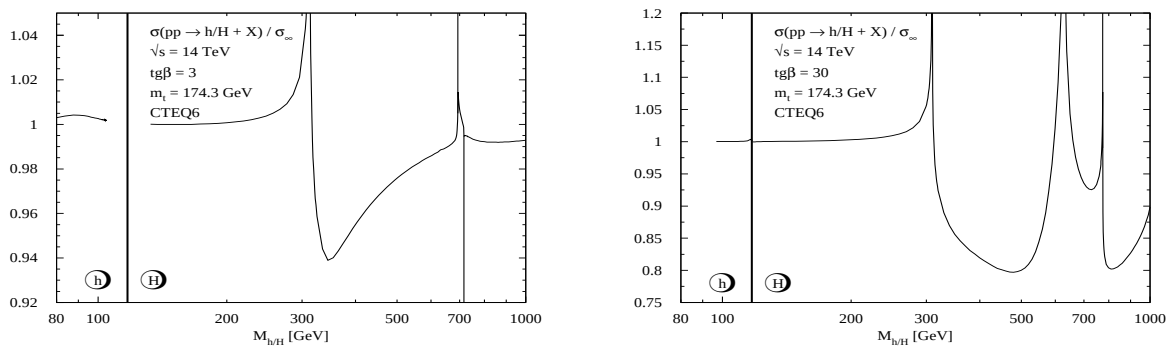

Fig. 24: *Ratio of the QCD corrected production cross sections of the scalar MSSM Higgs bosons via gluon fusion including the full squark mass dependence and those obtained by taking the relative QCD corrections to the squark loops in the heavy mass limit as functions of the corresponding Higgs masses for* $\mathrm{tg}\beta = 3$ *and 30.*

and of the NLO cross sections in the heavy squark limits, exemplifies the squark mass effects on the K factors. In addition to the LO squark mass dependence of the cross section, the K factors develop a squark mass dependence of up to about 20% and hence support the relevance of our results compared to the previous results of Ref. [198]. The squark mass effects on the K factors are larger than the corresponding quark mass effects [211]. And they are larger than the residual theoretical uncertainties so that they cannot be neglected in realistic analyses. Since the gluino contributions are expected to be much smaller, the squark mass dependence will be the dominant part of the differences between the heavy mass limits and a full MSSM calculation at NLO.

11.3 Conclusions

We have discussed the NLO QCD corrections to the squark loop contributions to neutral MSSM Higgs boson production in gg fusion at the LHC and their decay modes into photons, including the full mass dependences. The corrections are sizeable and stabilize the theorectical predictions compared to the LO results. Squark mass effects on the relative QCD corrections are significant and larger than the mass effects from quark loops. They are always relevant for Higgs masses beyond the corresponding virtual squark-antisquark threshold or for squark masses of the order of the top mass. Since they are larger than the experimental uncertainties and the approximative results beyond NLO indicate sufficient perturbative convergence, the results of this work have to be taken into account for realistic analyses.

12. HIGGS BOSON PRODUCTION IN ASSOCIATION WITH b QUARKS: SUSY QCD CONTRIBUTIONS [18]

12.1 Introduction

In the Standard Model, Higg production in association with b quarks is never important. However, in the minimal supersymmetric model (MSSM), the couplings of the Higgs bosons to b quarks can be significantly enhanced for large values of $\tan\beta$ and for a large range of parameter space, Higgs production in association with b quarks is the most likely discovery channel [83, 86, 89, 212, 213].

The production of a Higgs boson in association with a b quark has been extensively studied. In a 4- flavor number scheme, the lowest order processes for producing a Higgs boson and a b quark are $gg \to b\overline{b}\phi$ and $q\overline{q} \to b\overline{b}\phi$ [83,85,214] (The neutral Higgs bosons of the MSSM are generically $\phi = h^0, H^0, A^0$). In a 5- flavor number scheme, the b quark appears as a parton and potentially large logarithms of the form $\ln(\frac{M_\phi}{m_b})$ are absorbed into b quark parton distribution functions. Although the 4- and 5- flavor number schemes represent different orderings of perturbation theory, the two schemes have been shown to yield equivalent numerical results. In the 5- flavor number scheme, the lowest order process for producing a

[18] Contributed by: S. Dawson and C. B. Jackson

Higgs boson in association with b quarks is $b\overline{b} \to \phi$ when no b quarks are tagged in the final state and $bg \to b\phi$ when a single b quark is tagged [83, 85, 86, 89, 214].

In this note, we consider the production process, $bg \to b\phi$, for which the NLO QCD corrections are well understood, [86, 89, 215]. Here we present the $\mathcal{O}(\alpha_s^2)$ SUSY QCD (SQCD) corrections from gluino-squark loops to the b- Higgs production cross section [93, 216]. We compare the results from an effective Lagrangian approach with those obtained from an exact one-loop calculation. Finally, we consider whether the process $bg \to b\phi$ +jet provides a useful signature and compare this channel with the irreducible background from $bg \to bZ$ +jet.

12.2 Effective Lagrangian

The MSSM contains two Higgs doublets, H_u and H_d. At tree level, the b quark couples to only one of the Higgs doublets (H_d) and there is no $\overline{\psi}_L b_R H_u$ coupling (where $\psi_L = (t_L, b_L)$). The coupling of the b quark to the "wrong" Higgs doublet at one-loop leads to the effective interaction [217, 218],

$$L_{eff} = -\lambda_b \overline{\psi}_L \left(H_d + \frac{\Delta m_b}{\tan\beta} H_u \right) b_R + h.c.\,. \tag{17}$$

This effective interaction shifts the b quark mass from its tree level value,

$$m_b = \frac{\lambda_b v_d}{\sqrt{2}} (1 + \Delta m_b)\,, \tag{18}$$

and also implies that the Yukawa couplings of the Higgs bosons to the b quark are shifted from the tree level predictions. The shift of the Yukawa couplings [92] can be accounted for using an effective Lagrangian [217, 219],

$$\begin{aligned} L_{eff} &= -\frac{m_b}{v_{SM}} \left(\frac{1}{1+\Delta m_b} \right) \left(-\frac{\sin\alpha}{\cos\beta} \right) \left(1 - \frac{\Delta m_b}{\tan\beta \tan\alpha} \right) \overline{b} b h^0 \\ &- \frac{m_b}{v_{SM}} \left(\frac{1}{1+\Delta m_b} \right) \left(\frac{\cos\alpha}{\cos\beta} \right) \left(1 + \frac{\Delta m_b \tan\alpha}{\tan\beta} \right) \overline{b} b H^0 \\ &- \frac{m_b}{v_{SM}} \left(\frac{1}{1+\Delta m_b} \right) \left(-\tan\beta \right) \left(1 - \frac{\Delta m_b}{\tan^2\beta} \right) \overline{b} i\gamma_5 b A^0 \\ &\equiv g_{b\overline{b}h} \overline{b} b h^0 + g_{b\overline{b}H} \overline{b} b H^0 + g_{b\overline{b}A} \overline{b} i\gamma_5 b A^0\,, \end{aligned} \tag{19}$$

where $v_{SM} = 246$ GeV, $\tan\beta = v_u/v_d$, and α is the mixing angle which diagonalizes the neutral Higgs boson mass matrix. The Lagrangian of Eq. 19 has been shown to sum all terms of $\mathcal{O}(\alpha_s^n \tan^n\beta)$ for large $\tan\beta$ [217].

The expression for Δm_b is found in the limit $m_b << M_\phi, M_Z << m_{\tilde{b}_1}, m_{\tilde{b}_2}, m_{\tilde{g}}$, (where $m_{\tilde{b}_1}, m_{\tilde{b}_2}, m_{\tilde{g}}$ are the sbottom and gluino masses) . The contribution to Δm_b from sbottom/gluino loops is [218, 220]

$$\Delta m_b = \frac{2\alpha_s(\mu_R)}{3\pi} m_{\tilde{g}} \mu \tan\beta I(m_{\tilde{b_1}}, m_{\tilde{b_2}}, m_{\tilde{g}})\,, \tag{20}$$

where the function $I(a,b,c)$ is,

$$I(a,b,c) = \frac{1}{(a^2-b^2)(b^2-c^2)(a^2-c^2)} \left\{ a^2 b^2 \log\left(\frac{a^2}{b^2}\right) + b^2 c^2 \log\left(\frac{b^2}{c^2}\right) + c^2 a^2 \log\left(\frac{c^2}{a^2}\right) \right\}. \tag{21}$$

μ is the bilinear Higgs mixing parameter and $\alpha_s(\mu_R)$ should be evaluated at a typical squark or gluino mass. Note that Eq. 20 is valid for arbitrary values of $\tan\beta$.

Eq. 20 is a non-decoupling effect: If the masses of the squarks and gluino, along with the mixing parameter μ, become large for fixed M_A, Δm_b does not vanish,

$$\Delta m_b \to -sign(\mu)\frac{\alpha_s}{3\pi}\left(\tan\beta + \cot\alpha\right). \tag{22}$$

In the large M_A limit,

$$\tan\beta + \cot\alpha \to -\frac{2M_Z^2}{M_A^2}\tan\beta\cos 2\beta + \mathcal{O}\left(\frac{M_Z^4}{M_A^4}\right), \tag{23}$$

and the decoupling limit of the MSSM is recovered [221].

The effective Lagrangian can be used to approximate the squark and gluino contributions to the rate for $bg \to b\phi$ [93]. We define an Improved Born Approximation in which the Born amplitude is normalized by the Yukawa couplings, $g_{b\bar{b}\phi}$, of Eq. 19,

$$\frac{d\hat{\sigma}_{IBA}}{dt} \equiv \frac{d\hat{\sigma}_{Born}}{dt}\left(\frac{g_{b\bar{b}\phi}}{g_{b\bar{b}\phi}^{LO}}\right)^2. \tag{24}$$

The Improved Born Approximation incorporates the effective Lagrangian approximation to the SQCD effects on the $b\bar{b}\phi$ Yukawa couplings at low energy, but does not include the full SQCD calculation. In particular, the "Improved Born Approximation" does not include contributions from box diagrams including internal squarks and gluinos or the full momentum dependence of the SQCD contributions.

12.3 Results

In Figs. 25 and 26 we compare the results for $bg \to bh^0$ and $bg \to bH^0$ at the LHC [93,222]. The curves labelled "LO" use CTEQ6L PDFs, $\alpha_s(\mu_R)$ evaluated at 1-loop, and use the tree level Yukawa couplings. The NLO results use CTEQ6M PDFs with the 2-loop evolution of $\alpha_s(\mu_R)$ and $\alpha_s^{NLO}(M_Z) = 0.118$. The Yukawa couplings of both the IBA and NLO results are evaluated using the effective Lagrangian of Eq. 19. The outgoing b quark is required to have $p_T(b) > 20$ GeV and $\mid \eta_b \mid < 2.5$. The renormalization and factorization scales are set to be $M_\phi/4$. The "Improved Born Approximation" (IBA) curves use NLO PDFS and the $2-$loop evolution of $\alpha_s(\mu_R)$. The b quark mass in the Yukawa couplings is the running $\overline{MS}$ mass evaluated at $2-$ loops for the NLO and IBA results and at $1-$ loop for the LO results. Finally, the MSSM parameters are evaluated using FeynHiggs to generate an effective Higgs mixing angle and radiatively corrected Higgs masses.

From Fig. 25, we see that for relatively light squark and gluino masses, it is important to include the exact SQCD contributions and that the Improved Born Approximation is a poor approximation to the complete result. In this case, the SQCD contributions significantly reduce the rate. On the other hand, for squark and gluino masses on the TeV scale, Fig. 26 demonstrates that the effective Lagrangian approach to including the SQCD corrections is extremely accurate. Both Figs. 25 and 26 assume $\tan\beta = 40$. For small values of $\tan\beta$, the SQCD corrections are insignificant.

In Fig. 27, we compare the tree level rate for $pp \to bh^0$ + jet, with the irreducible background from $pp \to bZ$ + jet at the LHC for $\tan\beta = 40$. We require $p_T(b)$ and $p_T(jet) > 20\ GeV$ and $\mid \eta_b, \eta_{jet} \mid < 2.5$. Unfortunately, the rate is quite small.

13. CHARGED HIGGS BOSONS IN THE MSSM AT CMS: DISCOVERY POTENTIAL [19]

13.1 Introduction

Identifying the mechanism of electroweak symmetry breaking will be one of the main goals of the LHC. The most popular models are the Higgs mechanism within the Standard Model (SM) and within the

[19] Contributed by M. Hashemi, S. Heinemeyer,R. Kinnunen, A. Nikitenko, and G. Weiglein

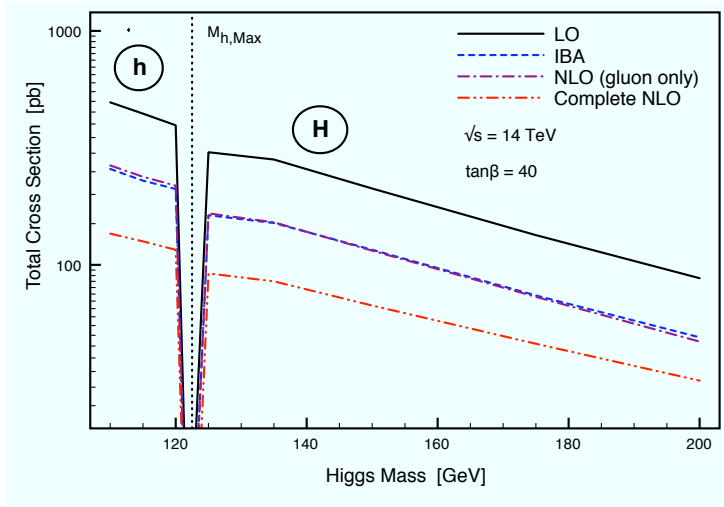

Fig. 25: Total cross section for $pp \to b\phi$ ($\phi = h^0, H^0$) at the LHC with $p_T(b) > 20$ GeV and $|\eta_b| < 2.5$. The curve labelled "Complete NLO" includes the full set of $\mathcal{O}(\alpha_s^2)$ QCD and SQCD contributions, while the curve labelled "NLO (gluon only)" omits the SQCD contributions. The MSSM parameters are $m_{\tilde{g}} = 250$ GeV, $m_{\tilde{b}_1} = 250$ GeV, and $m_{\tilde{b}_2} = 350$ GeV.

Minimal Supersymmetric Standard Model (MSSM) [223–225]. Contrary to the case of the SM, in the MSSM two Higgs doublets are required. This results in five physical Higgs bosons instead of the single Higgs boson of the SM. These are the light and heavy $\mathcal{CP}$-even Higgs bosons, h and H, the $\mathcal{CP}$-odd Higgs boson, A, and the charged Higgs boson, $H^\pm$. The Higgs sector of the MSSM can be specified at lowest order in terms of the gauge couplings, the ratio of the two Higgs vacuum expectation values, $\tan\beta \equiv v_2/v_1$, and the mass of the $\mathcal{CP}$-odd Higgs boson, M_A (or $M_{H^\pm}$, the mass of the charged Higgs boson). Consequently, the masses of the $\mathcal{CP}$-even neutral Higgs bosons (and the charged Higgs boson) are dependent quantities that can be predicted in terms of the Higgs-sector parameters. The same applies to the production and decay properties of the MSSM Higgs bosons[20]. Higgs-phenomenology in the MSSM is strongly affected by higher-order corrections, in particular from the sector of the third generation quarks and squarks, so that the dependencies on various other MSSM parameters can be important.

The charged Higgs bosons of the MSSM (or a more general Two Higgs Doublet Model (THDM)) have been searched at LEP [226], yielding a bound of $M_{H^\pm} \gtrsim 80$ GeV [227, 228]. The Tevatron placed new bounds on the MSSM parameter space from charged Higgs-boson searches at large $\tan\beta$ and low M_A [229]. At the LHC the charged Higgs bosons will be accessible best at large $\tan\beta$ up to $M_A \lesssim 800$ GeV [98, 230, 231]. At the ILC, for $M_{H^\pm} \lesssim \sqrt{s}/2$ a high-precision determination of the charged Higgs boson properties will be possible [232–236].

The prospective sensitivities at the LHC are usually displayed in terms of the parameters M_A and $\tan\beta$ (or $M_{H^\pm}$ and $\tan\beta$) that characterize the MSSM Higgs sector at lowest order. The other MSSM parameters are conventionally fixed according to certain benchmark scenarios [200, 231]. We focus here [237] on the $5\,\sigma$ discovery contours for the charged MSSM Higgs boson for the two cases $M_{H^\pm} < m_t$ and $M_{H^\pm} > m_t$, within the $m_h^{\max}$ scenario and the no-mixing scenario. For the interpretation of the exclusion bounds and prospective discovery contours in the benchmark scenarios it is important to assess how sensitively the results depend on those parameters that have been fixed according to the benchmark prescriptions. Consequently, we investigate how the $5\,\sigma$ discovery regions in the $M_{H^\pm}$–$\tan\beta$ plane for the charged MSSM Higgs boson obtainable with the CMS experiment at the LHC depend on the other MSSM parameters, most prominently the Higgs mixing parameter μ.

[20] If the production or decay involves SUSY particles at tree-level, also other MSSM parameters enter the prediction.

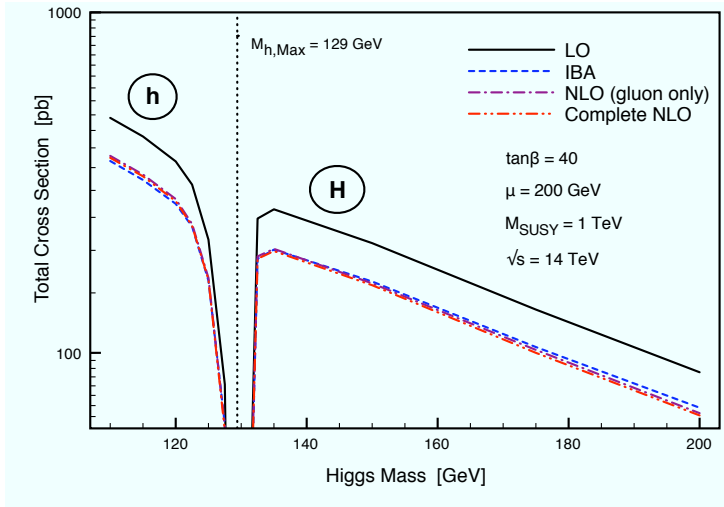

Fig. 26: Total cross section for $pp \to b\phi$ ($\phi = h^0, H^0$) at the LHC with $p_T(b) > 20$ GeV and $|\eta_b| < 2.5$. The curve labelled "Complete NLO" includes the full set of $\mathcal{O}(\alpha_s^2)$ QCD and SQCD contributions, while the curve labelled "NLO (gluon only)" omits the SQCD contributions. The MSSM parameters are $m_{\tilde{g}} \sim m_{\tilde{b}_1} \sim m_{\tilde{b}_2} \sim 1$ TeV.

13.2 Experimental Analysis

The main production channels at the LHC are

$$pp \to t\bar{t} \to H^- \bar{b}\, t \;\text{ or }\; \bar{t}\, H^+ b \tag{25}$$

and

$$gb \to H^- t \;\text{ or }\; g\bar{b} \to H^+ \bar{t}\,. \tag{26}$$

The decay used in the analysis to detect the charged Higgs boson is

$$H^\pm \to \tau \nu_\tau\,. \tag{27}$$

The analysis described below correspond to CMS experimental sensitivities based on full simulation studies, assuming an integrated luminosity of 30 fb^{-1}.

13.21 The light charged Higgs Boson

The "light charged Higgs boson" is characterized by $M_{H^\pm} < m_t$. The main production channel is given in eq. (25). Close to threshold also eq. (26) contributes. The relevant (i.e. detectable) decay channel is given by eq. (27). The experimental analysis, based on 30 fb^{-1} collected with CMS, is presented in Ref. [238].

A total number of events leading to final states with the signal characteristics is evaluated, including their respective experimental efficiencies. The various channels and the corresponding efficiencies can be found in Tab. 13. A $5\,\sigma$ discovery can be achieved if a parameter point results in more than 5260 events (with 30 fb^{-1}). We furthermore used $\mathrm{BR}(W^\pm \to l\nu_l) = 0.217$ ($l = \mu, e$), $\mathrm{BR}(W^\pm \to \tau\nu_\tau) = 0.1085$, $\mathrm{BR}(W^\pm \to \text{jets}) = 0.67$, $\mathrm{BR}(\tau \to \text{hadrons}) = 0.65$. The next-to-leading order LHC cross section for top quark pairs is taken to be 840 pb. For the W+3 jets background the leading order cross section for the process $pp \to W^\pm + 3$ jets, $W^\pm \to \ell^\pm \nu$ ($\ell = e,\ \mu$) as given by MadGraph Ref. [173, 239] generator (840 pb) was used.

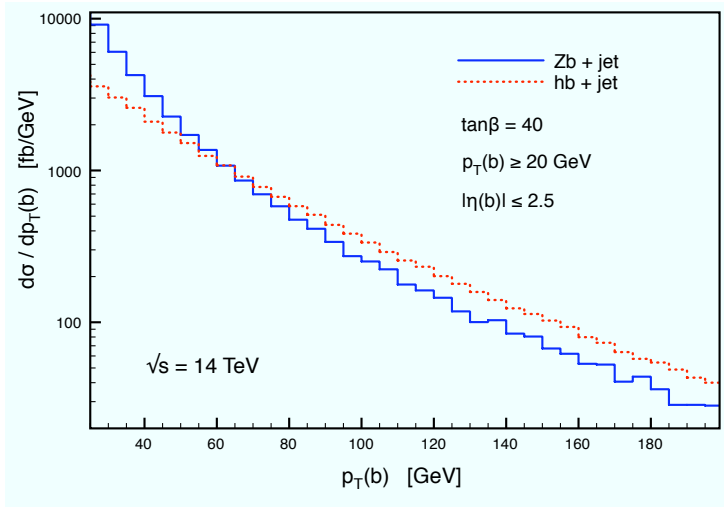

Fig. 27: Comparison of the transverse momentum distributions for the bottom quark jet in the signal process $pp \to b\phi + j$ and background process $pp \to bZ + j$ at the LHC.

channel	exp. efficiency
$pp \to t\bar{t} \to H^+ b\, \bar{t} \to (\tau^+ \bar{\nu}_\tau)\ (W^+ b)$; $\tau \to$ hadrons, $W \to l\nu_l$	0.0052
$pp \to t\bar{t} \to W^+\, W^- \to (\tau\nu_\tau)\ (l\nu_l)$; $\tau \to$ hadrons	0.00217
$pp \to t\bar{t} \to W^+\, W^- \to (l\nu_l)\ (l\nu_l)$	0.000859
$pp \to t\bar{t} \to W^+\, W^- \to$ (jet jet) $(l\nu_l)$	0.000134
$pp \to W + 3$ jets, $W \to \ell\nu$	0.000013

Table 13: Relevant channels for the light charged Higgs bosons and their respective experimental efficiencies. The charge conjugated processes ought to be included. The efficiency for the charged Higgs production is given for M_{H^+}=160 GeV. l denotes e or μ.

13.22 The heavy charged Higgs Boson

The "heavy charged Higgs boson" is characterized by $M_{H^\pm} > m_t$. Here eq. (26) gives the largest contribution, and very close to threshold eq. (25) can contribute somewhat. The relevant decay channel is again given in eq. (27). The experimental analysis, based on 30 fb^{-1} collected with CMS, is presented in Ref. [240].

The number of signal events is evaluated as

$$N_{\rm ev} = \mathcal{L} \times \sigma(pp \to H^\pm + X) \times {\rm BR}(H^\pm \to \tau\nu_\tau) \times {\rm BR}(\tau \to {\rm hadrons}) \times {\rm exp.\ eff.}\ , \qquad (28)$$

where $\mathcal{L}$ denotes the luminosity and the experimental efficiency is given in Tab. 14 as a function of $M_{H^\pm}$. A $5\,\sigma$ discovery corresponds to a number of signal events larger than 14.1.

$M_{H^\pm}$ [GeV]	171.6	180.4	201.0	300.9	400.7	600.8
exp. eff. [10^{-4}]	3.5	4.0	5.0	23	32	42

Table 14: Experimental efficiencies for the heavy charged Higgs boson detection.

The charged Higgs boson production with the mass close to the top quark mass (first column in

Tab. 14) was generated with the PYTHIA generator processes 401 ($gg \to tbH^{\pm}$) and 402 ($qq \to tbH^{\pm}$) implemented as described in Ref. [241].

13.3 Calculation of Cross Section and Branching Ratios

For the calculation of cross sections and branching ratios we use a combination of up-to-date theory evaluations. The Lagrangian for the interaction of the charged Higgs boson with the t/b doublet is given by [217]

$$\mathcal{L} = \frac{g}{2M_W} \frac{\overline{m}_b}{1+\Delta_b} \left[\sqrt{2}\, V_{tb}\, \tan\beta\, H^+ \bar{t}_L b_R \right] + \text{h.c.} \tag{29}$$

Here $\overline{m}_b$ denotes the running bottom quark mass including SM QCD corrections. The prefactor $1/(1+\Delta_b)$ in eq. (29) arises from the resummation of the leading corrections to all orders. The explicit form of Δ_b in the limit of heavy SUSY masses and $\tan\beta \gg 1$ reads [218, 220, 242]

$$\Delta_b = \frac{2\alpha_s}{3\pi}\, m_{\tilde{g}}\, \mu\, \tan\beta \times I(m_{\tilde{b}_1}, m_{\tilde{b}_2}, m_{\tilde{g}}) + \frac{\alpha_t}{4\pi}\, A_t\, \mu\, \tan\beta \times I(m_{\tilde{t}_1}, m_{\tilde{t}_2}, \mu)\,. \tag{30}$$

Here $m_{\tilde{t}_1}, m_{\tilde{t}_2}, m_{\tilde{b}_1}, m_{\tilde{b}_2}$ denote the $\tilde{t}$ and $\tilde{b}$ masses, $m_{\tilde{g}}$ is the gluino mass. Large negative μ can lead to a strong enhancement of the $H^{\pm}tb$ coupling, while a large positive value leads to a strong suppression. Concerning the $m_h^{\max}$ and the no-mixing benchmark scenarios, as discussed in Refs. [231, 243] the Δ_b effects are much more pronounced in the $m_h^{\max}$ scenario, where the two terms in eq. (30) are of similar size. In the no-mixing scenario the first term in eq. (30) dominates, and the total effect is smaller.

For the production cross section in eq. (25) we use the SM cross section $\sigma(pp \to t\bar{t}) = 840$ pb times the $\text{BR}(H^{\pm} \to tb)$ including the Δ_b corrections described above. The production cross section in eq. (26) is evaluated as given in Refs. [244, 245]. In addition also the Δ_b corrections of eq. (29) are applied. Finally the $\text{BR}(H^{\pm} \to \tau\nu_{\tau})$ is evaluated taking into account all decay channels, among whom the most relevant are $H^{\pm} \to tb, cs, W^{(*)}h$. For the decay to tb again the Δ_b corrections are included. All the numerical evaluations are performed with the program `FeynHiggs` [246–249].

13.4 Numerical Analysis

The numerical analysis has been performed in the $m_h^{\max}$ and the no-mixing scenario [200, 231] for $\mu = -1000, -200, +200, +1000$ GeV. In Fig. 28 we show the results combined for the $5\,\sigma$ discovery contours for the light and the heavy charged Higgs boson, corresponding to the experimental analyses in Sects. 13.21 and 13.22, respectively. As described above, the analyses were performed for the CMS detector and 30 fb^{-1}. The top quark mass is set to $m_t = 175$ GeV.

Within the $m_h^{\max}$ scenario, shown in the left plot of Fig. 28 the search for the light charged Higgs boson covers the area of large $\tan\beta$ and $M_{H^{\pm}} \lesssim 150$ GeV. The variation with μ induces a strong shift in the $5\,\sigma$ discovery contours with $\Delta\tan\beta = 15$ for $M_{H^{\pm}} = 100$ GeV, rising up to $\Delta\tan\beta = 40$ for larger $M_{H^{\pm}}$ values. The discovery region is largest (smallest) for $\mu = -(+)1000$ GeV, corresponding to the largest (smallest) production cross section.

The $5\,\sigma$ discovery regions for the search for heavy charged Higgs bosons show a similar behavior. For $M_{H^{\pm}} = 170$ GeV the accessible parameter space starts at $\tan\beta = 20(58)$ for $\mu = -(+)1000$ GeV, i.e. the variation of μ again induces a very strong shift in the $5\,\sigma$ discovery contours. For $M_{H^{\pm}} = 300$ GeV the $5\,\sigma$ regions vary from $\tan\beta = 38$ to $\tan\beta = 54$. For $\mu = -1000$ GeV and larger $\tan\beta$ values the bottom Yukawa coupling becomes so large that a perturbative treatment would no longer be reliable in this region.

The no-mixing scenario is shown in the right plot of Fig. 28. The qualitative behavior is the same as for the $m_h^{\max}$ scenario. However, as discussed above, the effects from a variation of μ are much less pronounced. The induced shifts stay below $\Delta\tan\beta = 20(10)$ in the search for the light (heavy) charged Higgs boson. The $5\,\sigma$ discovery areas are slightly larger than in the $m_h^{\max}$ scenario.

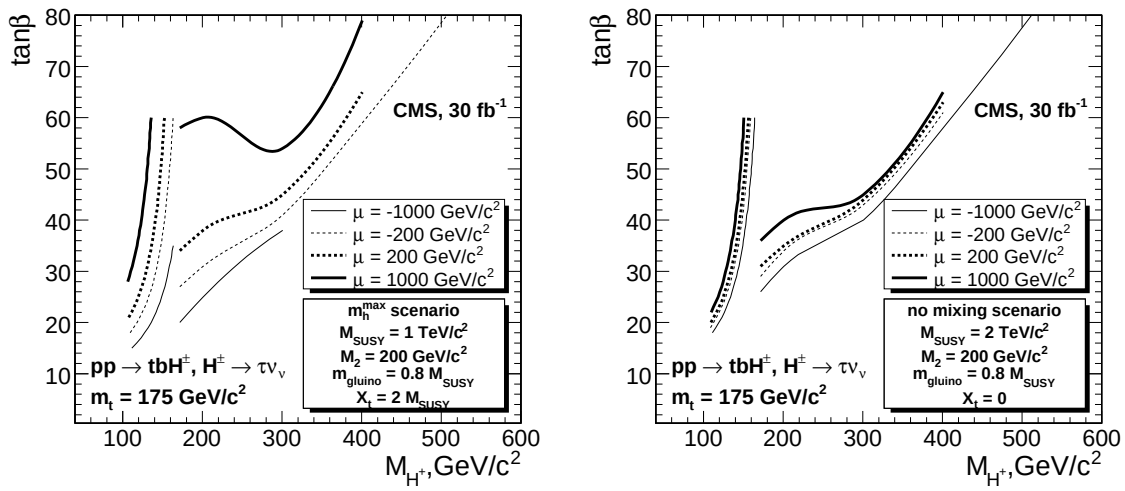

Fig. 28: Discovery reach for the charged Higgs boson of CMS with 30 fb^{-1} in the $M_{H^\pm}$–$\tan\beta$ plane for the $m_h^{\max}$ scenario (left) and the no-mixing scenario (right).

13.5 Conclusions

We have presented the $5\,\sigma$ discovery contours for the search for the charged MSSM Higgs boson. We combine the latest results for the CMS experimental sensitivities based on full simulation studies with state-of-the-art theoretical predictions of MSSM Higgs-boson properties. The experimental analyses are done assuming an integrated luminosity of 30 fb^{-1} for the two cases, $M_{H^\pm} < m_t$ and $M_{H^\pm} > m_t$.

The numerical analysis has been performed in the $m_h^{\max}$ and the no-mixing scenario for $\mu = \pm 200, \pm 1000$ GeV. The search for the light charged Higgs boson covers the are area of large $\tan\beta$ and $M_{H^\pm} \lesssim 160$ GeV. The search for the heavy charged Higgs boson reaches up to $M_{H^\pm} \lesssim 400$ GeV for large tb. The variation of μ induces a very strong shift in the $5\,\sigma$ discovery contours of up to $\Delta\tan\beta = 40$. The effect enters via the variation of Δ_b, affecting the charged Higgs production cross section and branching ratios. Large negative μ values give the largest reach, while large positive values yield the smallest $5\,\sigma$ discovery areas.

Acknowledgements

The work of S.H. was partially supported by CICYT (grant FPA 2007–66387). Work supported in part by the European Community's Marie-Curie Research Training Network under contract MRTN-CT-2006-035505 'Tools and Precision Calculations for Physics Discoveries at Colliders'.

14. STUDIES OF SPIN EFFECTS IN CHARGED HIGGS BOSON PRODUCTION WITH AN ITERATIVE DISCRIMINANT ANALYSIS AT THE TEVATRON AND LHC [21]

14.1 Introduction

The importance of charged Higgs boson searches has in the recent years been emphasized, including in the '2005 Les Houches' proceedings [90]. This work extends the charged Higgs boson '2005 Les Houches' studies. It is the purpose of this note to outline the possible improvements that can be achieved at the Tevatron and LHC in the search for charged Higgs bosons focussing on the spin effects and the $H^\pm \to \tau\nu_\tau$ decay. In order to quantify the spin effect an Iterative Discriminant Analysis (IDA) method [250] has been applied, which is a powerful tool to separate signal and background, even in

[21] Contributed by: S. Hesselbach, S. Moretti, J. Rathsman and A. Sopczak

cases such as the one presently under study when several selection variables with limited discriminant power are present.

14.2 Tevatron Energy

We start by studying charged Higgs production $q\bar{q}, gg \to tbH^{\pm}$ with subsequent decays $t \to bW$, $H^{\pm} \to \tau\nu_{\tau}$ at the FNAL Tevatron with $\sqrt{s} = 1.96$ TeV. In the following we analyze hadronic decays of the $W^{\pm}$ boson and τ lepton ($W^{\pm} \to q\bar{q}'$, $\tau \to \mathrm{hadrons}+\nu_{\tau}$), which results in the signature $2b+2j+\tau_{\mathrm{jet}}+p_t^{\mathrm{miss}}$ (2 b jets, 2 light jets, 1 τ jet and missing transverse momentum). The most important irreducible background process is $q\bar{q}, gg \to t\bar{t}$ with the subsequent decays $t \to bW^{+}$ and $\bar{t} \to \bar{b}W^{-}$, one $W^{\pm}$ boson decaying hadronically ($W^{\pm} \to q\bar{q}'$) and one leptonically ($W^{\mp} \to \tau\nu_{\tau}$), which results in the same final state particles as for the expected signal.

14.21 Simulation and Detector Response

The signal process $q\bar{q}, gg \to tbH^{\pm}$ is simulated with PYTHIA [251]. The subsequent decays $t \to bW^{\pm}$ (or its charge conjugate), $W^{\pm} \to q\bar{q}'$ and $H^{\mp} \to \tau\nu_{\tau}$ are also carried out within PYTHIA, whereas the τ leptons are decayed externally with the program TAUOLA [252, 253], which includes the complete spin structure of the τ decay. The background process $q\bar{q}, gg \to t\bar{t}$ is also simulated with PYTHIA with the built-in subroutines for $t\bar{t}$ production. The decays of the top quarks and $W^{\pm}$ bosons are performed within PYTHIA and that of the τ lepton within TAUOLA.

The momenta of the final b and light quarks from the PYTHIA event record are taken as the momenta of the corresponding jet, whereas for the τ jet the sum of all non-leptonic final state particles as given by TAUOLA is used. The energy resolution of the detector and parton shower and hadronization effects are emulated through a Gaussian smearing $(\Delta(p_t)/p_t)^2 = (0.80/\sqrt{p_t})^2$ of the transverse momentum p_t for all jets in the final state, including the τ jet [254]. As typical for fast simulation studies, no effects of underlying events, are simulated. Events are removed which contain jets with less than 20 GeV transverse momentum[22], corresponding to about $|\eta| > 3$. The transverse momentum of the leading charged pion in the τ jet is assumed to be measured in the tracker independently of the transverse momentum of the τ jet. The identification and momentum measurement of the pion is important to fully exploit the τ spin information. In order to take into account the tracker performance we apply Gaussian smearing on $1/p_t^{\pi}$ with $\sigma(1/p_t^{\pi})[\mathrm{TeV}^{-1}] = \sqrt{0.52^2 + 22^2/(p_t^{\pi}[\mathrm{GeV}])^2 \sin\theta_{\pi}}$, where θ_{π} is the polar angle of the π. The missing transverse momentum p_t^{miss} is constructed from the transverse momenta of all visible jets (including visible τ decay products) after taking the modelling of the detector into account. The generic detector description is a good approximation for both Tevatron experiments, CDF and D0.

14.22 Expected Rates

For completeness we present a brief discussion of the expected cross section of the charged Higgs boson signature under investigation. The signal cross section has been calculated for $\tan\beta = 30$ and $m_{H^{\pm}} = 80, 100, 130$ and 150 GeV with PYTHIA, version 6.325, using the implementation described in [241], in order to take the effects in the transition region into account. Furthermore, it has been shown in [255] that the signal cross section for $tbH^{\pm}$ agrees with the one from the top-decay approximation $t\bar{t} \to tbH^{\pm}$ for charged Higgs boson masses up to about 160 GeV if the same factorization and renormalization scales are used. Thus, we have used everywhere in this study the factorization scale $(m_t + m_{H^{\pm}})/4$ and the renormalization scale $m_{H^{\pm}}$ for both signal and background (i.e., those recommended in [241] as most appropriate for the $tbH^{\pm}$ signal)[23], since the primary purpose of our study is to single out variables that show a difference between our $W^{\pm}$ and $H^{\pm}$ data samples and that this can unambiguously be ascribed to

[22] In order to be largely independent of the specific detector performance, no requirement on the jet resolution is applied.

[23] Clearly, for a proper experimental study, factorization and renormalization scales for our background process $q\bar{q}$, $gg \to t\bar{t} \to tbW^{\pm}$ ought to be chosen appropriately, i.e., unrelated to the charged Higgs boson mass.

the different nature of the two kinds of bosons (chiefly, their different mass and spin state). In addition, the running b quark mass entering in the Yukawa coupling of the signal has been evaluated at $m_{H^\pm}$. This procedure eventually results in a dependence of our background calculations on $\tan\beta$ and, especially, $m_{H^\pm}$ that is more marked than the one that would more naturally arise as only due to indirect effects through the top decay width. Hence, the cross sections have been rescaled with a common factor such that the total $t\bar{t}$ cross section is $\sigma_{t\bar{t}}^{\rm prod} = 5.2$ pb [256]. To be more specific, we have first calculated the total cross section $\sigma_{t\bar{t}}^{\rm prod,PYTHIA}(m_{H^\pm})$ with the built-in routine for $t\bar{t}$ production in PYTHIA for all $m_{H^\pm} = 80, 100, 130$ and 150 GeV and then calculated from this the respective rescaling factors $c(m_{H^\pm}) = 5.2\ {\rm pb}/\sigma_{t\bar{t}}^{\rm prod,PYTHIA}(m_{H^\pm})$ for each $m_{H^\pm}$. Then we have calculated the background cross section for $m_{H^\pm} = 80$ GeV into the final state with the signature $2b + 2j + \tau_{\rm jet} + p_t^{\rm miss}$ by enforcing the respective decay channels in PYTHIA using the built-in routine for $t\bar{t}$ production and multiplied it with $c(80\ {\rm GeV})$. In the same manner we have calculated the signal cross sections with the PYTHIA routines for $tbH^\pm$ production by enforcing the respective decay channels in PYTHIA and multiplying with the rescaling factors $c(m_{H^\pm})$ for $m_{H^\pm} = 80, 100, 130, 150$ GeV. The resulting cross sections are given in Table 15 before ($\sigma^{\rm th}$) and after (σ) applying the basic cuts $p_t^{\rm jets} > 20$ GeV and the hard cut $p_t^{\rm miss} > 100$ GeV. For the four signal masses, the $tbH^\pm$ and $t\bar{t} \to tbH^\pm$ cross section calculations agree numerically.

Table 15: Tevatron cross sections of background $q\bar{q}, gg \to t\bar{t}$ and signal $q\bar{q}, gg \to tbH^\pm$ for $\tan\beta = 30$ and $m_{H^\pm} = 80, 100, 130$ and 150 GeV into the final state $2b + 2j + \tau_{\rm jet} + p_t^{\rm miss}$ before ($\sigma^{\rm th}$) and after (σ) the basic cuts ($p_t > 20$ GeV for all jets) and the hard cut ($p_t^{\rm miss} > 100$ GeV).

	$q\bar{q}, gg \to t\bar{t}$	$q\bar{q}, gg \to tbH^\pm$			
$m_{H^\pm}$ (GeV)	80	80	100	130	150
$\sigma^{\rm th}$ (fb)	350	535	415	213	85
σ (fb) for $p_t^{\rm jets} > 20$ GeV	125	244	202	105	32
σ (fb) for $(p_t^{\rm jets}, p_t^{\rm miss}) > (20, 100)$ GeV	21	30	25	18	7

14.23 Event Preselection and Discussion of Discriminant Variables

The expected cross sections of the $2b + 2j + \tau_{\rm jet} + p_t^{\rm miss}$ signature are of the same order of magnitude for the signal and background reactions, as shown in Table 15. Thus, the same number of signal and background events is assumed for the analysis of different kinematic selection variables. For the signal $5 \cdot 10^5$ events have been simulated with PYTHIA for each charged Higgs mass at the Tevatron energy of 1.96 TeV using the built-in $t\bar{t}$ routine in the $t\bar{t} \to tbH^\pm$ approximation, while for the $t\bar{t}$ background also $5 \cdot 10^5$ events have been simulated using the built-in $t\bar{t}$ routine. Then the basic cuts $p_t^{\rm jets} > 20$ GeV are applied. An additional hard cut on the missing transverse momentum $p_t^{\rm miss} > 100$ GeV is used to suppress the QCD background, as for example demonstrated in Ref. [257]. After the additional anti-QCD cut about 28000 to 42000 signal events, depending on the simulated charged Higgs bosons mass, and about 30000 $t\bar{t}$ background events remain. Other background reactions, for example W+jet production, are expected to be negligible because they have either a much lower production cross section or are strongly suppressed compared to $t\bar{t}$ background, as quantified for example in Ref. [257]. In addition to the previous study (based on $5000 \times {\rm BR}(\tau \to {\rm hadrons})$ events each) [90], the present one applies an IDA method [250] to explore efficiencies and purities. As already mentioned, particular attention is devoted to the study of spin sensitive variables in the exploitation of polarization effects for the separation of signal and background events.

Examples of the signal and background distributions of some of the kinematic variables used in the IDA method and the respective difference between signal and background distributions are given in Ref. [258], namely:

- the transverse momentum of the τ jet, $p_t^{\tau_{\rm jet}}$,

- the transverse momentum of the leading $\pi^\pm$ in the τ jet, $p_t^{\pi^\pm}$,
- the ratio $p_t^{\pi^\pm}/p_t^{\tau_{\rm jet}}$,
- the transverse momentum of the second (least energetic) b quark jet, $p_t^{b_2}$,
- the transverse mass[24] in the $\tau_{\rm jet} + p_t^{\rm miss}$ system, $m_t = \sqrt{2p_t^{\tau_{\rm jet}} p_t^{\rm miss}[1-\cos(\Delta\phi)]}$, where $\Delta\phi$ is the azimuthal angle between $p_t^{\tau_{\rm jet}}$ and $p_t^{\rm miss}$,
- the invariant mass distribution of the two light quark jets and the second b quark jet, m_{jjb_2},
- the spatial distance between the τ jet and the second b quark jet, $\Delta R(\tau, b_2) = \sqrt{(\Delta\phi)^2 + (\Delta\eta)^2}$, where $\Delta\phi$ is the azimuthal angle between the τ and b jet, and
- the sum of the (scalar) transverse momenta of all the quark jets, $H_{\rm jets} = p_t^{j_1} + p_t^{j_2} + p_t^{b_1} + p_t^{b_2}$.

The distributions of signal and background events are normalized to the same number of 10^4 events, in order to make small differences better visible.

The signal and background distributions for the variables shown in Ref. [258] are as expected rather similar for $m_{H^\pm} = m_{W^\pm}$ and are hence mostly important to discriminate between signal and background in the IDA for $m_{H^\pm} > m_{W^\pm}$. Especially the transverse mass, shows a large variation with the charged Higgs boson mass. However, the different spin of the charged Higgs boson and the $W^\pm$ boson has a large effect on the τ jet variables $p_t^{\tau_{\rm jet}}$ and $p_t^{\pi^\pm}$ resulting in significantly different distributions of signal and background even for $m_{H^\pm} = m_{W^\pm}$. Moreover, the spin effects in the $p_t^{\tau_{\rm jet}}$ and $p_t^{\pi^\pm}$ distributions are correlated where the distributions of the ratio $p_t^{\pi^\pm}/p_t^{\tau_{\rm jet}}$ [259–261] show even larger differences [258]. This highlights the importance of the additional variable $p_t^{\pi^\pm}$ (and hence $p_t^{\pi^\pm}/p_t^{\tau_{\rm jet}}$), compared to a previous study [90]. The large separation power of this variable is indeed due to the different τ polarizations in signal and background [258]. There the signal and background distributions for $p_t^{\tau_{\rm jet}}$, $p_t^{\pi^\pm}$ and $p_t^{\pi^\pm}/p_t^{\tau_{\rm jet}}$ are shown for reference samples where the τ decay has been performed without the inclusion of spin effects with the built-in routines of PYTHIA and hence the differences between signal and background nearly vanish.

14.24 Iterative Discriminant Analysis (IDA)

The IDA method is a modified Fisher Discriminant Analysis [250] and is characterized by the use of a quadratic, instead of a linear, discriminant function and also involves iterations in order to enhance the separation between signal and background.

In order to analyze our events with the IDA method, signal and background have been split in two samples of equal size. With the first set of samples the IDA training has been performed and then the second set of samples has been analyzed. We have used the following 20 variables in the IDA study: the transverse momenta $p_t^{\tau_{\rm jet}}$, $p_t^{\pi^\pm}$, $p_t^{\rm miss}$, $p_t^{b_1}$, $p_t^{b_2}$, $p_t^{j_1}$, $p_t^{j_2}$, p_t^{jj}; the transverse mass m_t; the invariant masses m_{jj}, m_{jjb_1}, m_{jjb_2}, m_{bb} and $\hat{s} = m_{jjbb\tau}$; the spatial distances $\Delta R(\tau, b_1)$, $\Delta R(\tau, b_2)$, $\Delta R(\tau, j_1)$, $\Delta R(\tau, j_2)$; the total transverse momenta of all quark jets $H_{\rm jets}$ and of all jets $H_{\rm all} = H_{\rm jets} + p_t^{\tau_{\rm jet}}$. In the analysis of real data, b-quark tagging probabilities and the reconstruction of t and W masses could be used to improve the jet pairing, and replace the allocation of least and most energetic b-jet by a probabilistic analysis.

The results of the IDA study are obtained for the event samples with spin effect in the τ decays for $m_{H^\pm} = 80, 100, 130, 150$ GeV and for the reference samples without the spin effect for $m_{H^\pm} = 80$ GeV in order to illustrate the spin effect. In all plots of the IDA output variable the number of background events has been normalized to the number of signal events. Two IDA steps have been performed. After the first step, 90% of the signal is retained when a cut at zero is applied on the IDA output variable. The signal and background events after this cut are then passed to the second IDA step. A cut on IDA output variable distributions after the second step leads to the efficiency and purity (defined as ratio

[24] Strictly speaking this is not the transverse mass since there are two neutrinos in the decay chain of the charged Higgs boson we are considering, even so the characteristics of this mass are very similar to that of the true transverse mass.

of the number of signal events divided by the sum of signal and background events) combinations. These combinations define the working point (number of expected background events for a given signal efficiency) and the latter can be optimized to maximize the discovery potential.

In order to illustrate the effect of the hard cut on the missing transverse momentum ($p_t^{\rm miss} > 100$ GeV), which is imposed to suppress the QCD background, the final efficiency-purity plot of the IDA analysis is shown in Fig. 29 for $m_{H^\pm} = 80$ GeV for two reference samples (red, long dashed: with spin effects in the τ decay; red, dotted: without spin effects) without imposing the hard cut. As expected the achievable purity for a given efficiency decreases with the hard cut, therefore the spin effects become even more important to separate signal and background. In principle, by choosing the signal reduction rates in the previous IDA iterations, the signal and background rates in the final distributions can be varied appropriately. However, we have checked that a different number of IDA iterations and/or different efficiencies for the first IDA iteration have only a minor effect on the final result.

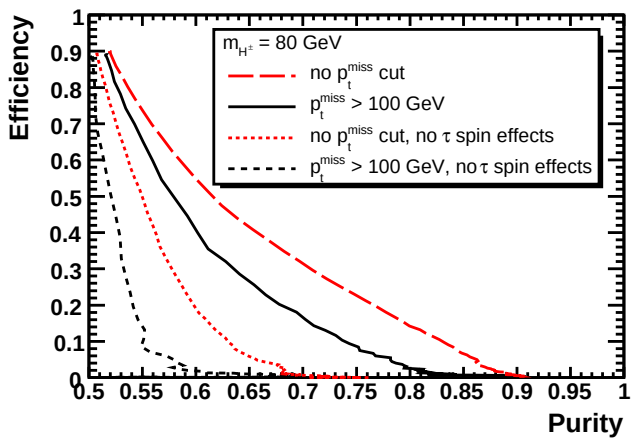

Fig. 29: Efficiency as a function of purity for $m_{H^\pm} = 80$ GeV and $\sqrt{s} = 1.96$ TeV. The black lines are the results after applying the hard cut $p_t^{\rm miss} > 100$ GeV when not taking the spin effects in the τ decay into account (dashed) and with spin effects in the τ decay (solid). The red lines are the results without applying the hard cut on $p_t^{\rm miss}$ when not taking the spin effects in the τ decay into account (dotted) and with spin effects in the τ decay (long dashed).

14.3 LHC Energy

The simulation procedure and the emulation of the detector response are the same as those outlined in Sect. 2.1 for the Tevatron, as well as, for the preselection and IDA method, as described in Sects. 2.3 and 2.4, respectively. Hence, only the expected LHC rates are discussed, followed by the description of changes in the distributions of the variables and the final IDA results.

Unlike the case of the Tevatron, where only charged Higgs masses smaller than the top quark mass can be explored, and 2HDM/MSSM signatures practically rely on $\tau\nu_\tau$ pairs only, at the LHC the phenomenology is more varied. Here, the search strategies depend strongly on the charged Higgs boson mass. If $m_{H^\pm} < m_t - m_b$ (later referred to as a light Higgs boson), the charged Higgs boson can be produced in top (anti-)quark decay. The main source of top (anti-)quarks at the LHC is again $t\bar{t}$ pair production ($\sigma_{t\bar{t}} = 850$ pb at NLO) [262]. For the whole $(\tan\beta, m_{H^\pm})$ parameter space there is a competition between the $bW^\pm$ and $bH^\pm$ channels in top decay keeping the sum ${\rm BR}(t \to bW^+) + {\rm BR}(t \to bH^+)$ at almost unity. The top quark decay to $bW^\pm$ is however the dominant mode for most of the parameter space. Thus, the best way to search for a (light) charged Higgs boson is by requiring that the top quark produced in the $tbH^\pm$ process decays to a $W^\pm$. While in the case of $H^\pm$ decays τ's will be tagged via their hadronic decay producing low-multiplicity narrow jets in the detector, there are two different $W^\pm$ decays that can be explored. The leptonic signature $b\bar{b}H^\pm W^\mp \to b\bar{b}\tau\nu l\nu$ provides a clean selection of the signal via the identification of the lepton $l = e, \mu$. In this case the charged Higgs transverse mass cannot be reconstructed because of the presence of two neutrinos with different origin. In this channel charged Higgs discovery will be determined by the observation of an excess of such events over SM expectations through a simple counting experiment. In the case of hadronic decays $b\bar{b}H^\pm W^\mp \to b\bar{b}\tau\nu jj$ the transverse mass can instead be reconstructed since all neutrinos are arising from the charged Higgs boson decay. This allows for an efficient separation of the signal and the main $t\bar{t} \to b\bar{b}W^\pm W^\mp \to b\bar{b}\tau\nu jj$ background (assuming $m_{H^\pm} \gtrsim m_{W^\pm}$). The absence of a lepton (e or μ)

provides a less clean environment but the use of the transverse mass makes it possible to reach the same mass discovery region as in the previous case and also to extract the charged Higgs boson mass. Both these channels show that after an integrated luminosity of 30 fb^{-1} the discovery could be possible up to a mass of 150 GeV for all tanβ values in both ATLAS and CMS [263–265].

If the charged Higgs is heavier than the top quark, the dominant decay channels are $H^\pm \to \tau\nu$ and $H^\pm \to tb$ depending on $\tan\beta$. They have both been studied by ATLAS and CMS [266–269]. The charged Higgs bosons are produced in the $pp \to tbH^\pm$ channel. For the $H^\pm \to tb$ decay, a charged Higgs boson can be discovered up to high masses ($m_{H^\pm} \sim 400$ GeV) in the case of very large $\tan\beta$ values and this reach cannot be much improved because of the large multi-jet environment. For the $H^\pm \to \tau\nu$ decay mode this reach is larger due to a cleaner signal despite a lower BR. In this case the 5σ reach ranges from $\tan\beta = 20$ for $m_{H^\pm} = 200$ GeV to $\tan\beta = 30$ for $m_{H^\pm} = 400$ GeV.

For the LHC, signal and background events have been simulated in the same way as for the Tevatron as described before, however, without implying any rescaling factor to match a measured $t\bar{t}$ cross section. Table 16 lists the resulting cross sections before ($\sigma^{\rm th}$) and after (σ) applying the basic cuts $p_t^{\rm jets} > 20$ GeV and the hard cut $p_t^{\rm miss} > 100$ GeV. The LHC rates allow for the discovery to be less challenging than at the Tevatron in the region $m_{H^\pm} \sim m_{W^\pm}$, yet the separation of signal events from background remains crucial for the measurement of the charged Higgs mass.

Table 16: LHC cross sections of background $q\bar{q}, gg \to t\bar{t}$ and signal $q\bar{q}, gg \to tbH^\pm$ for $\tan\beta = 30$ and $m_{H^\pm} = 80, 100, 130$ and 150 GeV into the final state $2b + 2j + \tau_{\rm jet} + p_t^{\rm miss}$ before ($\sigma^{\rm th}$) and after (σ) the basic cuts ($p_t > 20$ GeV for all jets) and the hard cut ($p_t^{\rm miss} > 100$ GeV).

	$q\bar{q}, gg \to t\bar{t}$	$q\bar{q}, gg \to tbH^\pm$			
$m_{H^\pm}$ (GeV)	80	80	100	130	150
$\sigma^{\rm th}$ (pb)	45.5	72.6	52.0	24.5	9.8
σ (pb) for $p_t^{\rm jets} > 20$ GeV	17.3	33.9	25.7	12.2	3.8
σ (pb) for $(p_t^{\rm jets}, p_t^{\rm miss}) > (20, 100)$ GeV	4.6	6.0	4.8	2.9	1.2

The kinematic distributions for $\sqrt{s} = 14$ TeV are shown in Ref. [258]. The choice of variables is identical to the one for the Tevatron and allows for a one-to-one comparison, the differences being due to a change in CM energy (and, to a somewhat lesser extent, due to the leading partonic mode of the production process[25]). The main differences with respect to the Tevatron case are that the various transverse momenta and invariant masses have longer high energy tails. In particular, it should be noted that the effect of the spin differences between $W^\pm$ and $H^\pm$ events can be explored very effectively also at LHC energies, e.g. the ratio $p_t^{\pi^\pm}/p_t^{\tau_{\rm jet}}$ which is very sensitive to the spin effects. These observations lead to the conclusion that the same method using spin differences can be used to separate signal from background at both the Tevatron and the LHC.

The distributions of the IDA output variables are shown in Ref. [258] for the study at $\sqrt{s} = 14$ TeV for two steps with 90% efficiency in the first step. These distributions are qualitatively similar to those for the Tevatron The final achievable purity for a given efficiency is shown in Fig. 30. As for the Tevatron energy a good separation of signal and background events can be achieved with the spin sensitive variables and the IDA method even in case $m_{H^\pm} \sim m_{W^\pm}$. For heavier $H^\pm$ masses the separation of signal and background events increases due to the kinematic differences of the event topology.

14.4 Conclusions

The discovery of charged Higgs bosons would be a clear sign of physics beyond the SM. In this case study we have investigated charged Higgs boson topologies produced at the current Tevatron and LHC energies and compared them against the irreducible SM background due to top-antitop production and

[25] As the latter is dominated by $q\bar{q}$ annihilation at the Tevatron and gg fusion at the LHC.

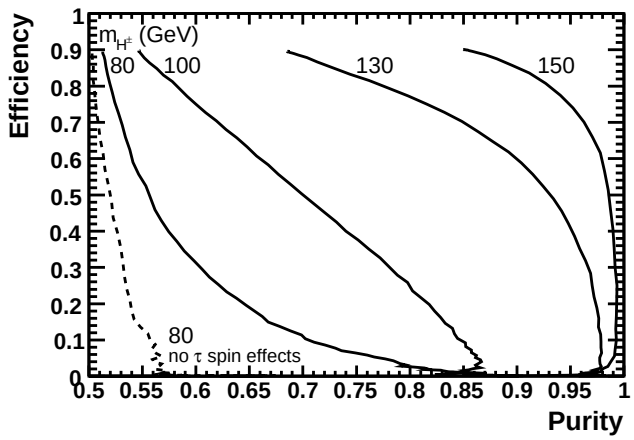

Fig. 30: Efficiency as a function of the purity when not taking the spin effects in the τ decay into account for $m_{H^\pm} = 80$ GeV (dashed) and with spin effects in the τ decay for $m_{H^\pm} = 80, 100, 130, 150$ GeV (solid, from left to right). Results are for the LHC.

decay. While sizable differences between signal and background are expected whenever $m_{H^\pm} \neq m_{W^\pm}$, near the current mass limit of about $m_{H^\pm} \approx 80$ GeV the kinematic spectra are very similar between SM decays and those involving charged Higgs bosons. In this case, spin information will significantly distinguish between signal and irreducible SM background. In fact, we have considered hadronic $\tau\nu_\tau$ decays of charged Higgs bosons, wherein the τ polarization induced by a decaying (pseudo)scalar object is significantly different from those emerging in the vector ($W^\pm$) decays onsetting in the top-antitop case. For a realistic analysis which is not specific for a particular detector, a dedicated Monte Carlo event generation and a simplified multipurpose detector response approximation have been applied. The identification of a hadronic tau-lepton will be an experimental challenge in an environment with typically four jets being present. We have demonstrated how an IDA method can be an applied to separate signal and background when the differences between the signal and background distributions are small. Our results show that the IDA method will be equally effective at both the Tevatron and LHC. While only the dominant irreducible $t\bar{t}$ background has been dealt with in detail, we have also specifically addressed the QCD background. A suitably hard missing transverse momentum cut has been applied to reject such jet activity and we have demonstrated that although the discriminative power is reduced by such a cut, the reduction is small compared to the gain from including the τ polarization effects. Using the differences in τ polarization between the signal and the dominant SM irreducible $t\bar{t}$ background is crucial for disentangling the former from the latter.

Acknowledgements

We would like to thank the organizers of the 2005 and 2007 editions of the Les Houches workshops "Physics at TeV Colliders' (where part of this work was carried out) and Johan Alwall for fruitful discussions.

Part IV

CP VIOLATING HIGGS BOSONS

15. JET ASSIGNMENT STUDIES IN THE SEARCH FOR THE DECAY $t \to bH^+$, $H^+ \to H_1^0 W^+$, $H_1^0 \to b\bar{b}$ IN THE CPX MSSM SCENARIO [26]

15.1 Introduction

The Minimal Supersymmetric Standard Model (MSSM) can have loop-induced CP-violation (CPX) if the Higgsino mass parameter, the gaugino masses and the trilinear couplings are complex. One of the key

[26] Contributed by: J.E. Cole, C.H. Shepherd-Themistocleous,and I.R. Tomalin

features of the CPX scenario is the suppression of the couplings of the neutral Higgs boson to both vector boson pairs and to $t\bar{t}$ pairs. The suppression of the H_1^0VV coupling effectively dilutes the limits set on the neutral Higgs using LEP data [270], allowing the existence of a light neutral Higgs boson ($40 - 50$ GeV) and a relatively light charged Higgs boson ($M(H^{\pm}) < M_{top}$) at low $\tan\beta$. The suppression of the couplings also makes the usual search methods at hadron colliders unviable. However, the suppression of the H_1^0VV leads to the enhancement of the $H_1H^+W^-$ coupling via a sum rule, making $t\bar{t}$ production events in which one of the top quarks decays via $t \to bH^+$, $H^+ \to H_1^0W^+$, $H_1^0 \to b\bar{b}$ one of the most promising search channels for the CPX scenario [271].

We present here a study of mass reconstruction and the impact of jet misassignment on this search using the CMS detector; A feasibility study for discovering the Higgs bosons in the CPX scenario also using the CMS detector is presented in Section 16.

15.2 Event generation

The signal event sample was generated using PYTHIA [183] and assuming the following parameters: $M(H_1^0 = 51$ GeV, $M(H^{\pm}) = 133$ GeV, $M_t = 175$ GeV, $\tan\beta = 5$ and $\Phi_{CP} = 90°$. In each event, one of the top quarks was forced to decay in the usual way, ie. $t \to bW$, while the other was forced to decay via $t \to bH^+$, $H^+ \to H_1^0W^+$, $H_1^0 \to b\bar{b}$. All possible $W^{\pm}$ decays were allowed. The relevant branching fractions were calculated using CPSuperH [272] and were found to be: $BR(t \to bH^+) = 0.01$, $BR(H^+ \to H_1^0W^+) = 0.99$ and $BR(H_1^0 \to b\bar{b}) = 0.92$. Taking the total $t\bar{t}$ production cross section to be 840 pb [273], this gives a cross section for this process of 8.68 pb.

For the purposes of this study only the subset of signal events in which one $W^{\pm}$ decayed hadronically and the other decayed leptonically (electron or muon) were considered, as this is the experimental signature that will be used to identify events in this analysis.

15.3 Event selection and mass reconstruction

This study was performed using only generator-level information. The iterative cone (IC) algorithm [274] with a radius of 0.5 was used for jet identification. The jets are formed out of stable generator-level particles, although neutrinos and muons are explcitly excluded from the process. Six or more jets must be found using the IC algorithm that satisfy the following requirements: $p_T^{jet} > 20$ GeV and $|\eta_{jet}| < 2.4$. Three of more must also satisfy $p_T^{jet} > 30$ GeV. In addition, an electron or muon that satisfies $p_T^l > 20$ GeV and $|\eta_l| < 2.4$ must also be present and the missing E_T reconstructed from generator-level particles must be greater than 20 GeV.

Events that pass these selection requirements then undergo the mass reconstruction procedure. The events are searched for the two possible decay channels, namely, $t \to bq\bar{q}'$, $t \to bbbl\nu$ and $t \to bl\nu$, $t \to bbbq\bar{q}' +$ (c.c.). As the study presented here is performed using generator-level information, the true lepton and neutrino from the leptonically-decaying $W^{\pm}$ are used. This means that during the mass reconstruction procedure, the $W^{\pm}$ four-vector is calculated simply by summing the lepton and neutrino four-vectors. When the $W^{\pm}$ decays hadronically, the mass is reconstructed using jets and must lie within 25 GeV of the nominal value. The corresponding mass constraint is placed on all reconstructed top masses. When reconstructing both of the top masses from a given jet combination, the jet associated with the b-quark ($t \to bW^{\pm}$ or $t \to bH^{\pm}$) must satisfy $p_T > 40$ GeV. A number of jet combinations will pass these requirements in each event and therefore the best candidate for a given event is selected by the minimization of a χ^2 based on the top masses and the mass of the hadronically-decaying $W^{\pm}$ candidate.

It should be noted that this mass reconstruction procedure results in three possible jet combinations associated with the best candidate χ^2. This is because the jets associated to the three b-quarks produced in the $t \to bbbW^{\pm}$ decay can be swapped around, but still give the same top mass value. However, the stricter jet p_T requirement applied to the jet associated to the b-quark from the $t \to bH^{\pm}$ decay can cause one or possibly two of the three combinations to be rejected before the χ^2 calculation is performed. All

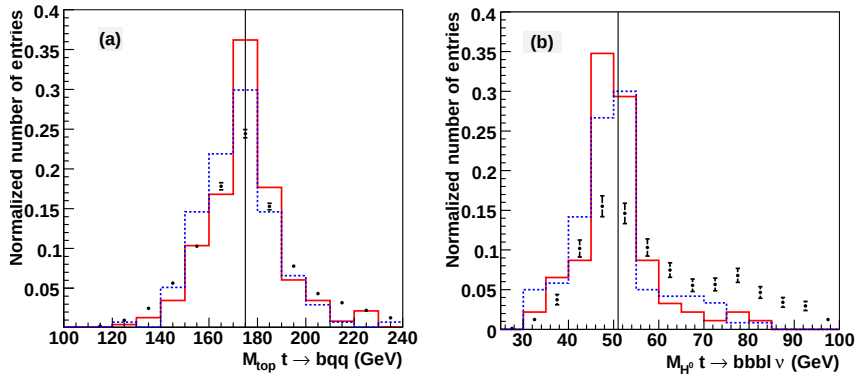

Fig. 31: The top mass distribution from the decay $t \to bq\bar{q}'$ and the $M(H_1^0)$ distribution from the decay $t \to bbbl\nu$ reconstructed from angular-matched jets. All distributions are made with angular-matched jets that satisfy $\Delta R < 0.5$. The dashed histograms, in addition, have the top and $W^{\pm}$ mass constraints applied, while the solid lines have the ΔR requirements tightened on for the decay products of the $W^{\pm} \to q\bar{q}'$ and the $H_1^0 \to b\bar{b}$.

the combinations corresponding to the best candidate χ^2 that also satisfy the stricter jet p_T requirement will be used when making the mass distributions.

15.4 Mass reconstruction studies

Before attempting to reconstruct masses at the detector level, it is important to understand whether good mass reconstruction is possible. This is done by identifying the jets associated to the quarks produced in the decay channel (these quarks are hereafter referred to collectively as "decay quarks") and reconstructing the masses from these jets.

The association of jets with the decay quarks is done using two possible matching procedures: Angular matching, in which the quantity $\Delta R = \sqrt{\Delta\eta^2 + \Delta\phi^2}$ is used to determine a unique set of jet-parton matches; or jet constituent matching, in which the particles assigned to a given jet are classified according to the top quark decay from which they originated. The fraction of the transverse momentum of a given jet, p_T^{jet}, carried by the constituents originating from each decay quark can then be determined and used to create a unique set of jet-parton matches.

Figure 31 shows the top mass distribution from the $t \to bq\bar{q}'$ decay and the H_1^0 mass distribution from the $t \to bbbl\nu$ decay reconstructed using angular-matched jets. The points correspond to those made using only jets that satisfy $\Delta R < 0.5$ and it can be seen that in both cases a clear peak is visible in the correct position, although the H_1^0 mass has a noticeable high mass tail. The dashed lines represent the distributions after some mass constraints have been applied: in the case of the top mass from the $t \to bq\bar{q}'$ decay, the light-quark jet pair must give $W^{\pm}$ mass within 25 GeV of the nominal value, while the mass from the corresponding $t \to bbbl\nu$ decay must lie within 25 GeV of the nominal value. In the case of the H_1^0 mass distribution both top masses and the hadronically-decaying $W^{\pm}$ must lie within 25 GeV of their nominal values. These mass constraints reduce slightly the high mass tail on the H_1^0 mass distribution. The solid lines do not have the mass constraints applied, but instead the ΔR requirement on the decay products of the H_1^0 and the hadronically-decaying $W^{\pm}$ boson have been tightened to $\Delta R < 0.1$. This all but removes the high mass tail on the neutral Higgs mass distribution, suggesting that the tail is caused by problems in the jet-parton matching procedure.

Given the large number of jets in these events, the most likely reason for having problems with jet-parton matching (and potentially more generally with mass reconstruction) is that the jets tend to overlap with each other. This can be verified using the p_T^{jet} fractions used for jet constituent matching. These fractions are determined by tracing all the particles associated to a given jet back to the top quark

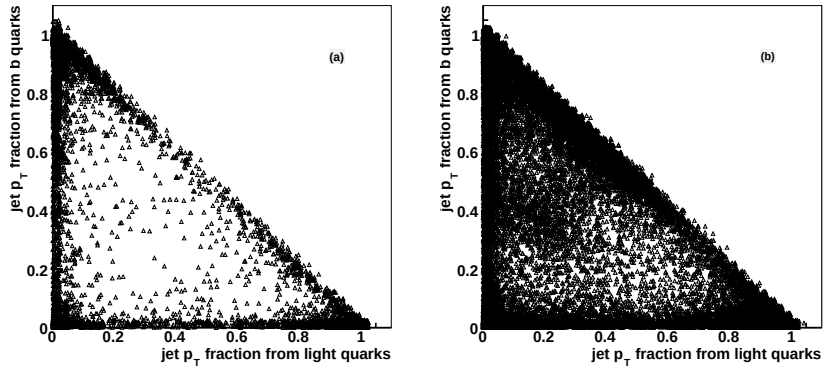

Fig. 32: (a) A comparison of the jet transverse momentum fractions for constituents coming from the b-quark and the light quarks in the decay $t \to bq\bar{q}'$ and (b) A comparison of the jet transverse momentum fractions for consituents coming from the decay products of the neutral Higgs and the hadronically-decaying $W^{\pm}$ in the decay channel $t \to bbbq\bar{q}'$.

decay they came from. The transverse momenta of the particles associated to a given decay quark are then summed and the result divided by the jet transverse momentum, resulting in six p_T fraction values per jet.

Figure 32(a) compares the p_T^{jet} fractions for all jets with particles associated to the b-quark and to either of the light quarks in the decay $t \to bq\bar{q}'$. Figure 32(b) shows the equivalent distribution for the decay channel $t \to bbbq\bar{q}'$, but compares the the fractions for all jets with particles associated to the H_1^0 decay products and the light quarks coming from the $W^{\pm}$ decay. No jet angular matching has been applied. The two combinations are chosen because they represent the jets from decay quarks that are expected to be closest to each other. In the case of the SM top decay, the distribution shows that the jets are well separated, as the values are concentrated at very high or low values. In the case of the $t \to bbbq\bar{q}'$ decay, it is clear that the jets overlap significantly, as suspected.

15.41 Jet assignment studies

Although jet overlapping has been identified as a potential problem for mass reconstruction, the results in section 15.4 show that it is basically possible to reconstruct reasonable mass distributions. However, the impact of jet misassignment on the mass distributions must also be understood and ways found to minimize its effect. Jet misassignment arises from two different sources: the misassignment of jets associated to the decay quarks and the misassignment of jets associated to other hard partons in the event, for example, gluons from initial state radiation or produced during parton showering. The contribution from these two sources can be studied by comparing the mass distributions from three different reconstruction procedures: those produced using jets matched to the decay quarks ("fully-matched"), those produced using the subset of jets matched to the decay quarks, but without using the knowledge about which jet belongs to which quark, ("partially-matched") and those produced using the standard mass reconstruction procedure ("unmatched"). Comparisons of "fully-matched" and "partially-matched" distributions provide information about the misassignment of jets from decay quarks, while comparisons of "partially-matched" and "unmatched distributions" provide information about the misassignment of jets from other hard partons.

Figure 33 shows the comparison of these three reconstruction methods for the top mass distribution from the $t \to bq\bar{q}'$ decay and the H_1^0 mass distribution and the corresponding top mass distribution from the $t \to bbbl\nu$ decay. The three methods for the top mass from the SM top decay are broadly in agreement, indicating that the reconstruction procedure is working well. The H_1^0 mass distribution shows differences between all three methods, indicating that there are contributions from both sources of misas-

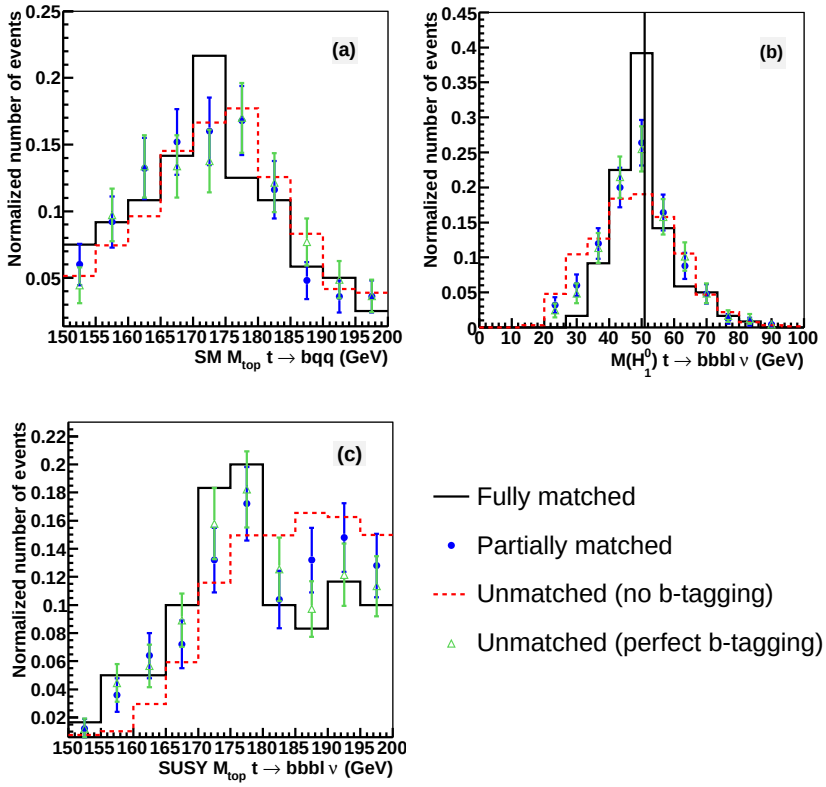

Fig. 33: A comparison of the fully-matched, partially-matched and unmatched (with and without b-tagging) mass distributions: (a) The top mass distribution from the decay $t \to bq\bar{q}'$, (b) the H_1^0 mass distribution from the decay $t \to bbbl\nu$ and (c) the top mass distribution from the $t \to bbbl\nu$ decay.

signed jets. However, in the case of the top mass distribution from the same decay the only difference is between the partially-matched and unmatched versions, ie. the contribution from the misassignment of jets associated to the decay quarks has disappeared. This indicates that the misassigned decay-quark jets observed in the H_1^0 mass distribution come from within the $t \to bbbl\nu$ decay chain. The high mass tail observed on the unmatched top mass distribution is therefore partially caused by the misassignment of jets associated to other hard partons. The remainder of the high mass tail, ie. the contribution that is also observed in the fully-matched distribution, is caused by overlapping jets, as discussed in section 15.4.

One possible method of improving the jet assignment during the mass reconstruction procedure is to use b-tagging. To study what impact it may have at generator level, "perfect" b-tagging can be used. Perfect b-tagging means using only jets that have been matched to one of the b-quarks if a b-tagged jet is required, while only jets not matched to a b-quark are used when a light-quark jet is required. Perfect b-tagging has been applied to the unmatched distributions, as shown in Fig.33, and it can be seen that the differences between the partially-matched and unmatched distributions are eliminated for all the mass distributions. This is consistent with the conclusion that this difference is a result of the misassignment of jets associated to other hard partons in the event, as the other hard partons are more likely to be gluon or light-quark jets than b-quark jets.

15.5 Conclusions

A study of jet reconstruction and assignment has been performed at generator level for the analysis of CP-violating Higgs production at LHC via the decay channel $pp \to t\bar{t}X$, $t \to bW^{\pm}$, $t \to bH^{\pm}$, $H^{\pm} \to H_1^0 W^{\pm}$, $H_1^0 \to b\bar{b}$. It has been established that it is possible to reconstruct reasonable mass distributions for this decay channel, but studies of jet-parton matching show that overlapping jets are a significant problem for the supersymmetric top decay. This results in a high mass tail on the top mass distributions reconstructed from the $t \to bbbW^{\pm}$ decay.

Jet assignment has also been studied for this decay channel and it has been found to be good for the mass distributions reconstructed using the Standard Model top decay channels. However, in the case of the supersymmetric top decay, the Higgs mass distributions show that there are contributions from both the misassignment of jets associated to other decay quarks and from jets associated to other hard partons in the event. However, only the latter contribution is observed in the corresponding top mass distributions, indicating that it is jets associated to the supersymmetric top decay that are being misassigned, not those from the SM top decay. The misassignment of jets from other hard partons also results in a high mass tail on the top mass distributions. The use of perfect b-tagging (based on jet-parton matching) suppresses this effect. This is consistent with the assumption that the other hard partons come from initial state gluon radiation or parton showering, as in this case the misassigned jets are much more likely to be gluon- or light quark-initiated jets.

It may be possible to reduce the impact of overlapping jets on the mass distributions by using a smaller jet cone radius or by using another jet finder, such as the k_t algorithm [155, 275]. The impact of detector-level jet finding and lepton identification must also be assessed.

16. SEARCH FOR THE $t \to bH^+$, $H^+ \to H_1W$, $H_1 \to b\bar{b}$ CHANNEL IN CPX MSSM SCENARIO IN CMS [27] [28]

16.1 Introduction

CP violation (CPX) in the Higgs sector of the Minimal Supersymmetric Standard Model (MSSM), when the Higgsino mass parameter μ, the gaugino mass parameters M_i and the trilinear couplings A_f are complex, allows the existence of the light neutral Higgs boson ($m_{H_1} \leq$ 50 GeV) and relatively light charged Higgs boson ($m_{H^+} \leq m_t$) in low tanβ region not excluded by the LEP data because of the reduction of H_1ZZ coupling [270]. In CPX scenario the usual search channels may not be useful, because of the simultaneous reduction in the couplings of the Higgs boson to the vector boson pair and to the top quark pair, as it affects the Higgs boson production and decays rates. The one of the promising search channels in the CPX scenario proposed in [271] is the $t\bar{t}$ production when one of the top quarks decays as $t \to bH^+$, $H^+ \to H_1W$, $H_1 \to b\bar{b}$. It is due to the suppression of the H_1ZZ coupling leads to the enhancement of the $H^+W^-H_1$ coupling in order to satisfy the coupling sum-rule. We investigated a feasibility for the discovery of the Higgs bosons in this channel using the full CMS detector simulated data. The results shown are preliminary.

16.2 Event generation

The signal events were generated using PYTHIA [183] with m_t=175 GeV, m_{H_1}=51 GeV and m_{H^+}=133 GeV, corresponding to tanβ=5 and CP mixing angle Φ(CP)=90^0 in the CPX MSSM. The following decays were forced in PYTHIA: $t_1 \to bW$, $t_2 \to bH^+$, $H^+ \to WH_1$, $H_1 \to b\bar{b}$ and both W bosons from the top decays were allowed to decay into all possible modes. The decay branching fractions were calculated using CPsuperH program [272]. The total cross section was calculated taking the next-to-leading order cross section for an inclusive $t\bar{t}$ production 840 pb [273] and multiplying by the branching ratios, Br($t \to bH^+$)=0.01, Br($H^+ \to H_1W$)=0.567, Br($t \to bW$)=0.99, Br($H_1 \to b\bar{b}$)=0.92 which gives the cross section 8.68 pb.

The major background processes for this channel are $t\bar{t} + \text{jets}$ and $t\bar{t}b\bar{b}$. The $t\bar{t} + \text{jets}$ background was generated using ALPGEN [180] with the MLM prescription for jet-parton matching [181, 182] at the PYTHIA shower simulation. The $t\bar{t} + 2$ jets (exclusive), $t\bar{t} + 3$ jets and $t\bar{t} + 4$ jets(inclusive) with jet p_T >20 GeV were generated. The cross sections for these processes are shown in Table 17. The $t\bar{t}b\bar{b}$ background was not considered yet in this study.

[27] Contributed by: A. K. Nayak, T. Aziz, and A. Nikitenko

[28] Results are preliminary and must not be shown at conferences

16.3 Simulation and Reconstruction

The CMS detector was simulated using full GEANT4 [276] simulation and the reconstruction was done using the CMS simulation and reconstruction software CMSSW. No pileup events were included. We summarize briefly the object reconstruction methods [277] used in this analysis. Muons are reconstructed from the muon chambers and the silicon tracker and electrons are reconstructed from the tracks in the silicon tracker and the clusters in the electromagnetic calorimeter. The loose electron identification criteria were applied. The lepton isolation was done using the tracker isolation such that leptons are selected if sum p_T of the tracks in a cone around the lepton (inner radius 0.015 and outer radius 0.25) is less than 3 GeV. The jets were reconstructed from the calorimeter towers using an iterative cone algorithm with the cone size 0.5. The jet energy was corrected using the Monte Carlo jet energy corrections. The missing E_T was reconstructed from the calorimeter towers and corrected for the jet energy scale. The missing E_T was also corrected for the muons by adding the muon momenta to the calorimeter missing E_T.

16.4 Event selection

16.41 Primary selections

The final state considered in this analysis consists of two light quarks, four b quarks, one lepton and neutrino: $\ell\nu + qq' + b\bar{b}b\bar{b}$. Since the neutral Higgs boson H_1 is very light (51 GeV), the b quarks from the $H_1 \rightarrow b\bar{b}$ decay are very soft as seen in Fig.34 (a,b). Only $\simeq 36\%$ of events have both b quarks from the H_1 decay with p_T^b >20 GeV. The final state quarks in the event fall very close to each other in (η, ϕ) space. Fig. 34 (c) shows the separation in (η, ϕ) space between two closest quarks. Because of these reasons it is difficult to reconstruct six jets in the event corresponding to the six final states quarks. The

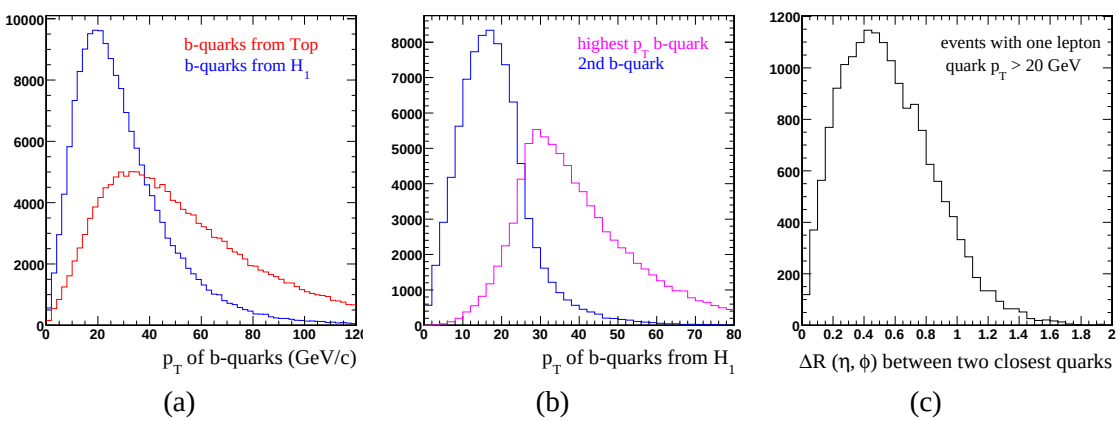

Fig. 34: (a) p_T distribution of b quarks from top quark and from H_1 decays, (b) p_T distribution of b quarks from H_1 decay, (c) the ΔR separation in (η, ϕ) space between two closest final state quarks in the event.

events with one isolated lepton with p_T >20 GeV and six or more jets with E_T >20 GeV were selected. The number of leptons in the event (electrons with $p_T > 10$ GeV and muons with p_T >5 GeV) passing the identification and the isolation were counted and the events with more than one lepton were rejected. The jets were b tagged using the track counting b-tagging algorithm. The three dimensional impact parameter significance of the second highest significance track in the jet was used as the b-discriminator parameter. The four highest discriminator jets with the discriminator value greater than 2.95 were tagged as b jets.

16.42 *Top mass reconstruction*

One W boson in the event was reconstructed from the lepton and the missing E_T. The z-component of the missing energy was calculated using the W mass constraint. This yields the real solutions in nearly 66% events. The events with the imaginary solutions were rejected. There are two possible solutions for the z-component of the missing energy which gives two possible candidates for the leptonically decaying W boson. The W boson decaying hadronically was reconstructed from the jets not tagged as b jets. All jet pairs with the invariant mass within the $m_W\pm$ 20 GeV mass window were considered as possible candidates. The di-jets invariant mass for the jets matching to quarks from the W boson decay is shown in Fig.35 (a). The momenta of the two top quarks were reconstructed simultaneously from four b-tagged

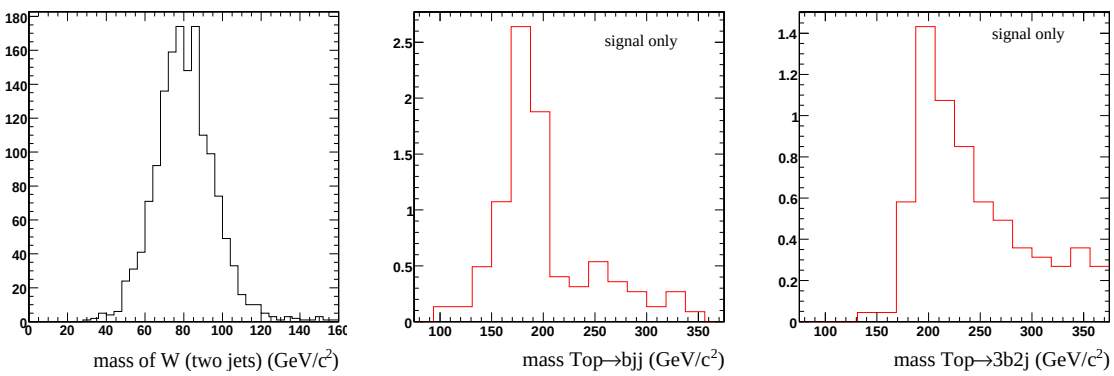

(a) (b) (c)

Fig. 35: (a) the di-jet invariant mass of the jets matching to quarks from W decay. (b) the top-quark mass reconstructed from the bjj final state after the minimization of δM. (c) the top-quark mass reconstructed from bbbjj final state after the minimization of δM.

jets, two $W \to \ell\nu$ candidates and candidates for the hadronically decaying W boson. The jets and the W boson candidates were assigned to the two top quarks by minimizing the δM, where δM is defined as

$$\delta\mathrm{M} = \sqrt{(\mathrm{m_{top1}} - \mathrm{m_{top}})^2 + (\mathrm{m_{top2}} - \mathrm{m_{top}})^2 + (\mathrm{m_{W(hadronic)}} - \mathrm{m_W})^2}, \tag{31}$$

there m_{top1} is reconstructed from one b-tagged jet and one W boson candidate, m_{top2} is reconstructed from three b-tagged jets and one W boson candidate, m_{top} is the generated top-quark mass (175 GeV) and the m_W is the W boson mass (PDG value).

The top-quark mass distributions reconstructed from three jets (bjj) and five jets ($bbbjj$) after the minimization of δM are shown in Fig.35 (b,c). One can see that the top-quark mass distribution from the $bbbjj$ final state is very wide and has a big tail. It is because of wrong assignment of the jets or W candidates to the top while minimizing δM. The events with the two top-quark reconstructed masses within the $m_{top}\pm$ 30 GeV mass window were selected. Table 17 shows the initial cross sections for the signal and background processes, the number of Monte-Carlo events remaining after each selection step and the cross sections after all selections. [29]

16.43 *Reconstruction of the neutral H_1 and charged H^+ Higgs bosons*

Since it is not known what pair of the b-tagged jets from the reconstructed top quark decay chain $t \to bbbW$ is coming from the $H_1 \to b\bar{b}$ decay, all three b-tagged jet pairs were considered as the

[29] The $W \to \ell\nu$ and $W \to$ jj reconstruction step selects events with the positive solution for z-component of E_T^{miss} and with at least one jet pair having the di-jet mass within the $m_W\pm$ 20 GeV mass window; the top-quark mass reconstruction step requires that the two top-quark reconstructed masses are within the $m_{top}\pm$ 30 GeV mass window.

Table 17: The initial cross sections for the signal and background processes, the number of Monte Carlo events remaining after each selection steps and the cross section after all selections.

	signal	$t\bar{t}+2$ jets (exclusive)	$t\bar{t}+3$ jets (exclusive)	$t\bar{t}+4$ jets (inclusive)
cross section, pb	8.68	100	40	61
number of MC events analyzed (corresponding luminosity, fb^{-1})	193884 (22.35)	241000 (2.41)	71000 (1.775)	94000 (1.54)
isolated lepton $p_T > 20$ GeV	41035	57920	16915	22214
≥ 6 jets $E_T > 20$ GeV	21389	36315	14479	21866
4 b-tagged jets with discr. >2.95	881	371	248	1069
$W \to \ell\nu$ and $W \to$ jj reco	379	158	132	602
top-quark mass reconstruction	83	4	1	7
cross section after all selections, fb	3.71	1.66	0.56	4.54

possible candidates. The invariant mass of b-tagged jet pairs, m_{bb} is shown in Fig. 36 (left plot) for the background and the signal plus background. The right plot in Fig. 36 shows, fitted by the Gaussian the m_{bb} distribution of the signal plus background. The mean value of the fitted distribution is close to the generated mass of H_1. The charged Higgs boson was reconstructed from the two b-tagged jets and W boson, where the b-tagged jet pair was chosen as the jet pair with the invariant mass closest to the peak of the m_{bb} mass distribution and within the window ± 20 GeV around the fitted mean value. The invariant mass distribution of the charged Higgs boson reconstructed in this way, m_{bbW} is shown in Fig.37.

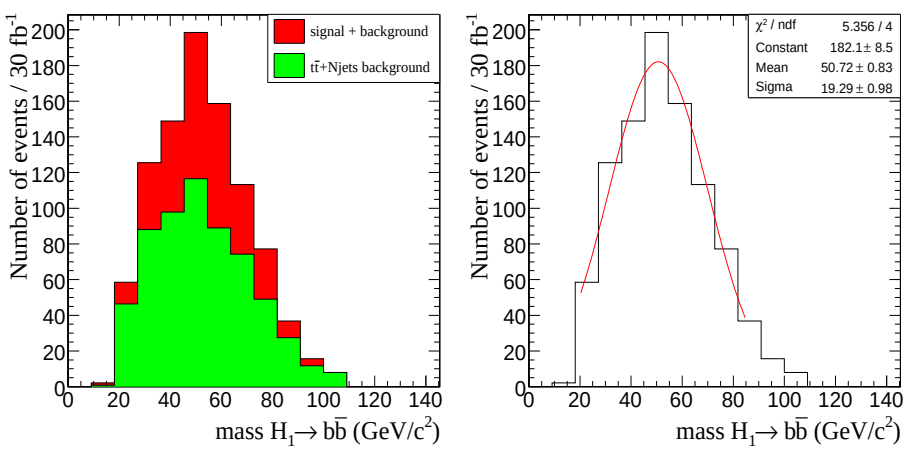

Fig. 36: The invariant mass of the b-tagged jet pairs from the reconstructed top quark decay chain $t \to bbbW$

The available Monte Carlo statistics of $t\bar{t}+$jets background events for this study was only order of $\simeq 2$ fb^{-1}, thus it can not be simply rescaled in order to produce the smooth shape of m_{bb} and m_{bbW} distributions expected for 30 fb^{-1} after all selections. We have obtained, however that the shape of m_{bb} and m_{bbW} distributions is almost the same after relaxing the cut on the b-discriminator value. Fig. 38 shows the m_{bb} (left plot) and m_{bbW} (right plot) distributions for four different b-discriminator cuts: 0, 1.0, 1.5 and 2.0.

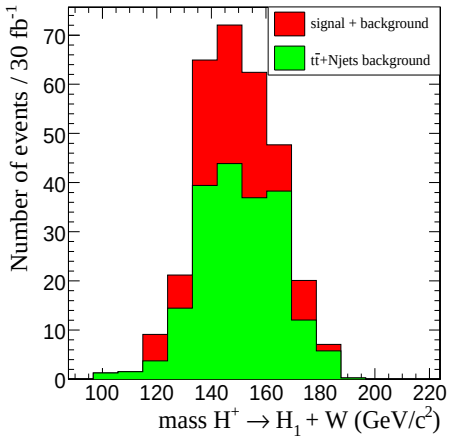

Fig. 37: The invariant mass of two b-tagged jets and W boson, where two b-tagged jets were chosen with the mass closest to the peak of the m_{bb} mass distribution and within the window $\pm$20 GeV around the fitted mean value

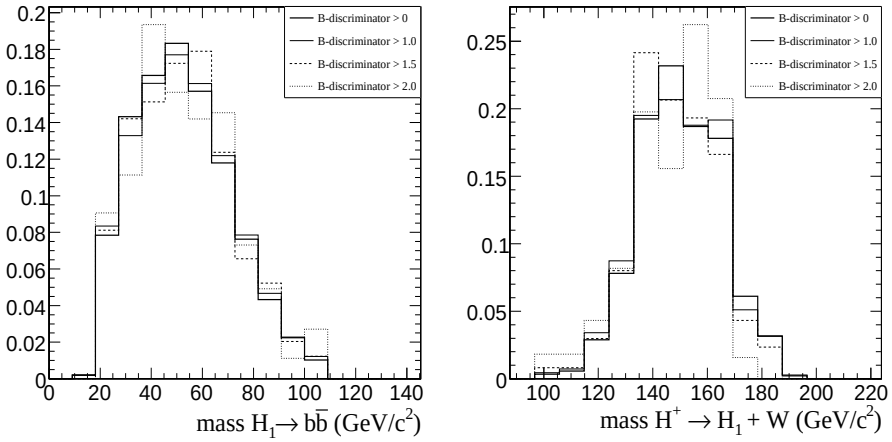

Fig. 38: The m_{bb} (left) and m_{bbW} (right) distributions after all selections for four different cuts on the b-discriminator value: 0, 1.0, 1.5 and 2.0.

16.5 Results

The simple selection strategy described in the previous sections yields S=110 signal events and B=203 $t\bar{t}+\text{jets}$ background events expected with 30 fb^{-1}. The $t\bar{t}b\bar{b}$ background still need to be taken into account. The uncertainty due to the Monte Carlo statistics on the $t\bar{t}+\text{jets}$ backgrounds is $\simeq$ 30$\%$. The experimental systematic uncertainty was estimated by taking into account the systematic uncertainties on the lepton identification (2$\%$), the b-jet tagging (5$\%$ per jet), the jet energy scale (5$\%$ per jet), the missing transeverse energy scale (10$\%$ on the raw calorimeter energy scale and 5$\%$ on the jet energy scale) and the luminosity uncertainty (5$\%$). It leads to the total systematic uncertainty 22.5$\%$ (the uncertainty due to the jet and the missing E_T scale only is 8.8%). The significance is calculated as $S/\sqrt{B+\Delta B^2}$, where ΔB is the experimental systematic uncertainty on the background. In order to get the pessimistic value for the significance, the Monte Carlo statistical uncertainty was added to the total background: B=203+60=263 events. The signal significance is then 110/$\sqrt{263+59^2}$=1.8. The uncertainty on the theoretical leading-order cross section of the $t\bar{t}+\text{n jets}$, (n$\geq$2) processes is $\geq$50%.

One can see that the discovery potential is restricted by both the experimental and the theoretical

uncertainties. The uncertainties can be partially reduced if the number of the background events and the m_{bb} and m_{bbW} mass shapes can be extracted from the data. The shapes can be evaluated from the data with the ratio S/B$<<$1 when the relaxed cut on the b-discriminator value is used (see Fig. 38). The background normalization on the number of events with the relaxed b-jet tagging will eliminate the jet and the missing E_T scale uncertainties, the luminosity uncertainty and partially reduce the b-tagging uncertainty which dominates the experimental uncertainty. It will also reduce the absolute background prediction uncertainty from the theory, since only the ratio of $t\bar{t} + \mathrm{jets}$ and $t\bar{t}b\bar{b}$ cross sections need to be used. The further, more detailed investigations of this channel is foreseen in CMS.

Acknowledgements

We would like to thank R. Godbole for very useful discussions and providing the code calculating Br($t \to bH^+$). We would like to thank our CMS colleagues Joanne Cole and Claire Shepherd-Themistocleous for the discussions about the optimal strategy for the jet reconstruction and assignment. Finally A.K.N. and A.N. thank organizers of Les Houches Workshop 2007 for the warm hospitality and the friendly and stimulating atmosphere.

Part V

NMSSM HIGGS BOSONS

17. LES HOUCHES BENCHMARK SCENARIOS FOR THE NMSSM [30]

17.1 Introduction

The next-to-minimal supersymmetric extension of the Standard Model (NMSSM) [278, 279], in which the spectrum of the minimal supersymmetric extension (MSSM) is extended by one singlet superfield, is interesting in many respects. Compared to the MSSM, it solves in an elegant way the so–called μ problem, has less fine tuning and can induce a rather different phenomenology in the Higgs and neutralino sectors. Given the possibility of a quite different phenomenology, it is important to address the question whether such NMSSM specific scenarios will be probed at the LHC. In particular, it would be crucial to make sure that at least one Higgs particle should be observed at the LHC for the planned integrated luminosity or try to define regions of the NMSSM parameter space in which more Higgs states than those available within the MSSM are visible. However, a potential drawback of the NMSSM, at least in its non-constrained versions, is that it leads to a larger number of input parameters to deal with. In particular, it is clearly unfeasible to make multi-dimensional scans over the free inputs of the NMSSM when performing complete/realistic simulations to address the two points mentioned above.

An alternative approach is to resort to a few benchmark scenarios which embodying the most peculiar/representative phenomenological features of the model's parameter space, which can be subject to full experimental investigation, without loss of substantial theoretical information. Building on the experience of Ref. [280], we define in this note benchmark points which fulfill the present collider and cosmological constraints using the most–up to date tools to calculate the particle spectra. We work in the framework of a semi–constrained NMSSM (cNMSSM) where the soft Supersymmetry (SUSY) breaking parameters are defined at some high scale, typically that of grand unification theories (GUTs). This approach leads to a much more plausible sparticle spectrum, allows to relate features of the Higgs sector to properties of the neutralino sector and, at the same time, still contains the distinctive phenomenological features of the NMSSM that are suitable for intensive phenomenological/experimental investigation. The emphasis is primarily on the different possible scenarios within the Higgs sector and the implication for

[30] Contributed by: A. Djouadi, M. Drees, U. Ellwanger, R.Godbole, C. Hugonie, S.F. King, S. Lehti, S. Moretti, A. Nikitenko, I. Rottländer, M. Schumacher, A. M. Teixeira

Higgs searches at the LHC. In particular, we propose five benchmark points which lead to Higgs-to-Higgs decays or a light Higgs spectrum but with reduced Higgs–gauge boson couplings, which are known to be rather difficult to probe at the LHC.

17.2 The Model and Its Spectrum

We confine ourselves to the NMSSM with a scale invariant superpotential given, in terms of (hatted) superfields with only the third generation (s)fermions included, by

$$\mathcal{W} = \lambda \widehat{S}\widehat{H}_u\widehat{H}_d + \frac{\kappa}{3}\,\widehat{S}^3 + h_t\widehat{Q}\widehat{H}_u\widehat{t}^c_R - h_b\widehat{Q}\widehat{H}_d\widehat{b}^c_R - h_\tau\widehat{L}\widehat{H}_d\widehat{\tau}^c_R. \tag{32}$$

The first two terms substitute the $\mu\widehat{H}_u\widehat{H}_d$ term in the MSSM superpotential, while the three last terms are the usual generalization of the Yukawa interactions. The soft SUSY breaking terms consist of the scalar mass terms for the Higgs, sfermion and gaugino fields and the trilinear interactions between the sfermion and Higgs fields. In an unconstrained NMSSM with non–universal soft terms at the GUT scale, the three SUSY breaking masses squared for H_u, H_d and S are determined through the minimization conditions of the scalar potential. Thus, the Higgs sector of the NMSSM is described by the six parameters

$$\lambda\ ,\ \kappa\ ,\ A_\lambda\ ,\ A_\kappa,\ \tan\beta = \langle H_u\rangle/\langle H_d\rangle \text{ and } \mu_{\rm eff} = \lambda\langle S\rangle\ . \tag{33}$$

As the number of input parameters is rather large, one can attempt to define a constrained (cNMSSM) model, similar to the minimal supergravity model or cMSSM, in which the soft SUSY breaking parameters are fixed at the GUT scale, leading to only a handful of inputs. One can thus impose unification of the gaugino, sfermion and Higgs mass parameters and the trilinear couplings at $M_{\rm GUT}$: $M_{1,2,3} \equiv M_{1/2}, m_{\tilde{F}_i} = m_{H_i} \equiv m_0, A_i \equiv A_0$. The fully constrained cNMSSM has two additional parameters, λ and κ, beyond the above and the correct M_Z value imposes one constraint. Hence, a priori, the number of inputs in the cMSSM and the fully constrained cNMSSM is exactly the same.

In practice, it is convenient to use the analytic form of the three minimization conditions of the NMSSM effective potential and, for given M_Z, $\tan\beta$, λ and all soft terms at the weak scale except for m_S^2, these can be solved for $|\mu_{\rm eff}|$ (or $|\langle S\rangle|$), κ and m_S^2; sign($\mu_{\rm eff}$) can still be chosen at will. Here, we will relax the hypothesis of complete unification of the soft terms in the singlet sector, $m_S^2 \neq m_0^2$ and $A_\kappa \neq A_0$ at $M_{\rm GUT}$, since the singlet could play a special rôle. In addition, for some of the benchmark points, we will also relax the unification hypothesis for $m_{H_u}^2$ and $m_{H_d}^2$ and for one scenario, the hypothesis $A_\lambda = A_0$. Such points in parameter space can have additional unconventional properties, whose phenomenology should also be investigated.

Following the procedure employed by the routine NMSPEC within NMSSMTools [281], which calculates the spectra of the Higgs and SUSY particles in the NMSSM, a point in the parameter space of the cNMSSM is defined by the soft SUSY breaking terms at $M_{\rm GUT}$ (except for the parameter m_S^2), $\tan\beta$ at the weak scale, λ at the SUSY scale (defined as an average of the first generation squark masses) and the sign of the parameter $\mu_{\rm eff}$. The parameters κ, m_S^2 and $|\mu_{\rm eff}|$ are determined at the SUSY scale in terms of the other parameters through the minimization equations of the scalar potential. The renormalisation group equations (RGEs) for the gauge and Yukawa couplings and those for the soft terms are integrated between M_Z and $M_{\rm GUT}$ defined by gauge couplings unification. For the most relevant Standard Model parameters, we chose $\alpha_s(M_Z) = 0.1172$, $m_b(m_b)^{\overline{\rm MS}} = 4.214$ GeV and $m_{\rm top}^{\rm pole} = 171.4$ GeV.

After RGE running is completed, the Higgs, gluino, chargino, neutralino and sfermion masses are computed including dominant one-loop corrections to their pole masses. All the Higgs decay branching ratios (BRs) into SM and SUSY particles are determined including dominant radiative corrections. Subsequently, the following Tevatron and LEP constraints are applied: i) Direct searches for the LSP neutralino and invisible Z decay width, ii) direct bounds on the masses of the charged particles $h^\pm$, $\chi^\pm$, $\tilde{q}$, $\tilde{l}$ and the gluino; iii) constraints on the Higgs production rates from all channels studied at LEP.

Light h_i ($i = 1, 2$) scalar states (with $M_{h_i} \lesssim 114$ GeV) can still be allowed by LEP constraints, if the Z–Z-h_i coupling is heavily suppressed or the lightest pseudoscalar a_1 state has $M_{a_1} \lesssim 10\,\mathrm{GeV}$ such that h_i decays dominantly into $a_1 a_1$ states but the $b\bar{b}$ decay of the a_1 is impossible. Constraints from the decays $h_i \to a_1 a_1 \to 4\tau$ allow for M_{h_i} down to ~ 86 GeV. Note that LEP constraints are implemented only for individual processes and that combinations of different processes could potentially rule out seemingly viable scenarios. Finally, experimental constraints from B physics are taken into account, and we require that the relic abundance of the NMSSM dark matter (DM) candidate, the lightest neutralino χ_1^0 which can be singlino-like, matches the WMAP constraint $0.094 \lesssim \Omega_{\rm CDM} h^2 \lesssim 0.136$ at the 2σ level.

17.3 The Benchmark Points

In the Higgs sector of the NMSSM, two different types of difficult scenarios have been pointed out, depending on whether Higgs-to-Higgs decays are kinematically allowed or forbidden; see e.g. Ref. [280].

Within the first category, there are two possibilities, each associated with light scalar/pseudoscalar Higgs states: (i) The lightest CP–odd a_1 state is rather light, $M_{a_1} \lesssim$ 40–50 GeV, and the lightest CP–even h_1 particle has enough phase space for the decay into two a_1 particles, $h_1 \to a_1 a_1$, to be allowed and dominant. The a_1 state will mainly decay into $\tau^+\tau^-$ if $M_{a_1} \lesssim 10$ GeV or to $\tau^+\tau^-$ ($\sim 10\%$) and $b\bar{b}$ (90%) states if $M_{a_1} \gtrsim 10$ GeV. One would have then the possibilities $h_1 \to a_1 a_1 \to 4\tau$ and $h_1 \to a_1 a_1 \to 4\tau, 4b$ and $2\tau 2b$ for the h_1 state which can have a mass that is either close to its theoretical upper limit of 130 GeV or to the lower limit of 90 GeV. (ii) The lightest CP–even h_1 boson is relatively light, $M_{h_1} \lesssim 50$ GeV, and decays into $b\bar{b}$ pairs (the situation where $M_{h_1} \lesssim 10$ GeV is very constrained by LEP data). In this case, the next-to-lightest CP-even h_2 state is SM–like with a mass below ~ 140 GeV and can decay into two h_1 bosons leading to the final topologies $h_2 \to h_1 h_1 \to 4\tau$, $2\tau 2b$ and $4b$.

The second category of scenarios, where Higgs-to-Higgs decays are suppressed, includes regions of the parameter space where the five neutral Higgs particles are relatively light, with masses in the range 90–180 GeV, which opens the possibility of producing all of the them at the LHC, but with couplings to gauge bosons that are reduced compared to the SM Higgs case. This scenario is similar to the so–called "intense coupling regime" of the MSSM [282] but with two more neutral Higgs particles.

We propose five benchmark points of the NMSSM parameter space, P1 to P5, in which the above mentioned scenarios are realized (see Ref. [283] for more details). Each point is representative of distinctive NMSSM features. Points P1 to P3 exemplify scenarios where h_1 decays into light pseudoscalar states decaying, in turn, into $b\bar{b}$ or $\tau^+\tau^-$ final states; these points can be realized within the cNMSSM with nearly universal soft terms at $M_{\rm GUT}$, the exception being the parameters m_S^2 and A_κ. P4 illustrates the NMSSM possibility of a very light h_1 and can be obtained once one relaxes the universality conditions on the soft SUSY breaking Higgs mass terms, $M_{H_d} \neq M_{H_u} \neq m_0$. Point P5 corresponds to the case where all Higgs bosons are rather light and can be obtained if one allows additionally for the inequality $A_\lambda \neq A_0$. In all cases, the input parameters as well as the resulting Higgs masses and some decay information are given in Table 18; the main characteristics of the χ_1^0 DM candidate are also given. Next, we summarize the most relevant phenomenological properties of the benchmark points.

In the first two points P1 and P2, the lightest h_1 CP–even state has a mass of $M_{h_1} \simeq 120$ GeV and is SM–like with couplings (relative to that of the SM Higgs) to gauge bosons R_1, top quarks t_1 and bottom quarks b_1, which are almost equal to unity. The lightest CP–odd a_1 boson has a mass of, respectively, 40.5 GeV and 9.09 GeV. In both cases P1 and P2, the decay channel $h_1 \to a_1 a_1$ is largely dominating with a BR very close to 90%, while the decays $h_1 \to b\bar{b}$ and $\tau^+\tau^-$ are suppressed by an order of magnitude when compared to the SM case. The most relevant difference between the two scenarios concerns the mass and decays of the lightest pseudoscalar state. In P1 the a_1 boson decays into b quarks and τ leptons with rates of $\sim 90\%$ and $\sim 10\%$, respectively. In contrast, in P2 the pseudoscalar a_1 state with its mass $M_{a_1} \simeq 9.09$ GeV decays dominantly into $\tau^+\tau^-$ pairs, with a rate above 80%.

For point P3, the same inputs of points P1 and P2 are chosen except for the A_κ and λ parameters,

Table 18: Input and output parameters for the five benchmark NMSSM points.

Point	P1	P2	P3	P4	P5
GUT/input parameters					
sign($\mu_{\rm eff}$)	+	+	+	–	+
$\tan\beta$	10	10	10	2.6	6
m_0 (GeV)	174	174	174	775	1500
$M_{1/2}$ (GeV)	500	500	500	760	175
A_0	-1500	-1500	-1500	-2300	-2468
A_λ	-1500	-1500	-1500	-2300	-800
A_κ	-33.9	-33.4	-628.56	-1170	60
NUHM: M_{H_d} (GeV)	-	-	-	880	-311
NUHM: M_{H_u} (GeV)	-	-	-	2195	1910
Parameters at the SUSY scale					
λ (input parameter)	0.1	0.1	0.4	0.53	0.016
κ	0.11	0.11	0.31	0.12	-0.0029
A_λ (GeV)	-982	-982	-629	-510	45.8
A_κ (GeV)	-1.63	-1.14	-11.4	220	60.2
M_2 (GeV)	392	392	393	603	140
$\mu_{\rm eff}$ (GeV)	968	968	936	-193	303
CP-even Higgs bosons					
m_{h_1} (GeV)	120.2	120.2	89.9	32.3	90.7
BR($h_1 \to b\bar{b}$)	0.072	0.056	7×10^{-4}	0.918	0.895
BR($h_1 \to \tau^+\tau^-$)	0.008	0.006	7×10^{-5}	0.073	0.088
BR($h_1 \to a_1 a_1$)	0.897	0.921	0.999	0.0	0.0
m_{h_2} (GeV)	998	998	964	123	118
m_{h_3} (GeV)	2142	2142	1434	547	174
CP-odd Higgs bosons					
m_{a_1} (GeV)	40.5	9.09	9.13	185	99.6
BR($a_1 \to b\bar{b}$)	0.91	0.	0.	0.62	0.91
BR($a_1 \to \tau^+\tau^-$)	0.085	0.88	0.88	0.070	0.090
m_{a_2} (GeV)	1003	1003	996	546	170
Charged Higgs boson					
$m_{h^\pm}$ (GeV)	1005	1005	987	541	188
LSP					
$m_{\tilde{\chi}_1^0}$ (GeV)	208	208	208	101	70.4
$\Omega_{CDM}h^2$	0.099	0.099	0.130	0.099	0.105

which are now varied as to have a lighter h_1 state. This again leads to a pseudoscalar a_1 boson which has approximately the same mass as in scenario P2, $M_{a_1} \simeq 9.96$ GeV, and which decays almost exclusively into $\tau^+\tau^-$ final states. The difference between P3 and P2 is the lightest CP–even Higgs boson h_1, which has a mass $M_{h_1} \simeq 90$ GeV, lower than in scenarios P1 and P2. In this case, and although h_1 is still SM–like, i.e. exhibiting couplings to gauge bosons, top and bottom quarks that are very close to those of the SM Higgs boson, it decays nevertheless almost exclusively into a_1 pairs, with a rate close to 100%. Another difference between P2 and P3 is that in the former case, the interesting decay mode $h_1 \to a_1 Z$ is kinematically possible but the rate is rather small, BR($h_1 \to a_1 Z$) $\sim 3\%$.

Note that in all these first three points, the heaviest neutral Higgs particles h_2, h_3 and a_2, as well as the charged Higgs states $h^\pm$, all have masses close to, or above, 1 TeV. The main decay modes are into $b\bar{b}$ and $t\bar{t}$ for the neutral and tb for the charged states, as $\tan\beta$ is not too large and the $t\bar{t}$–Higgs couplings are not very strongly suppressed, while the BRs for the neutral Higgs-to-Higgs decays, in particular the channels $h_2 \to h_1 h_1$ and $h_2 \to a_1 a_1$, are very tiny, not exceeding the permille level. Regarding the properties of the DM candidate, P1, P2 and P3 exhibit a lightest neutralino which is bino–like, with mass is $m_{\chi_1^0} \simeq 208$ GeV. In all three cases, the correct cosmological density, $\Omega_{\rm CDM}h^2 \simeq 0.1$, is achieved

through the co–annihilation with the $\tilde{\tau}_1$ slepton, which has a mass comparable to that of the LSP.

Point P4 corresponds to a scenario in which the CP–even boson h_1 is very light, $M_{h_1} = 32.3$ GeV and singlet–like and predominantly decays into $b\bar{b}$ pairs, with BR$(h_1 \to b\bar{b}) = 92\%$, and to a smaller extent into τ pairs with BR$(h_1 \to \tau^+\tau^-) \simeq 7\%$. The CP–even h_2 boson has a mass of $M_{h_2} \simeq 123$ GeV and is SM–like, with normalized couplings to W/Z and t/b states close to unity. However, it mostly decays into two h_1 bosons, BR$(h_2 \to h_1 h_1) \simeq 88\%$ and the dominant SM–like $b\bar{b}$ decay mode occurs only at a rate less than 10%. The lightest CP–odd particle is not very heavy, $M_{a_1} = 185$ GeV, and decays mostly into fermion pairs, with BR$(a_1 \to b\bar{b}) \sim 61\%$ and BR$(a_1 \to \tau^+\tau^-) \sim 7\%$; the other dominant decay is the interesting channel $a_1 \to h_1 Z$ which has a rate of the order of 30%. Finally, the heaviest CP-even h_3, CP–odd a_2 and the charged $h^\pm$ particles have masses in the 500 GeV range and will mostly decay, as $\tan\beta$ is small, into $t\bar{t}/tb$ final states for the neutral/charged states. All these features make the phenomenology of point P4 rather different from that of points P1 to P3 discussed above. To achieve a correct cosmological relic density, the common sfermion and gaugino mass parameters at $M_{\rm GUT}$ are close to 1 TeV. At the SUSY scale, one thus finds a higgsino-singlino-like neutralino LSP, whose mass is $m_{\chi_1^0} \sim 100$ GeV and LSP annihilation essentially leads to WW and Zh_1 final states.

Finally, point P5 is characterized by having all Higgs particles relatively light with masses in the range 90 to 190 GeV. Here, both λ and κ are relatively small. The three CP–even Higgs bosons with masses of 91, 118 and 174 GeV, respectively, share the couplings of the SM Higgs boson to the gauge bosons with the dominant component being taken by the h_2 state. The pseudoscalar Higgs bosons have masses $M_{a_1} \simeq 100$ GeV and $M_{a_2} \simeq 170$ GeV, while the charged Higgs particle is the heaviest one with $M_{h^\pm} \simeq 188$ GeV. Here, all the neutral Higgs-to–Higgs decays are kinematically disfavored; this is also the case of neutral Higgs decays into into lighter Higgs states with opposite parity and gauge bosons. The only non–fermionic two–body Higgs decays are thus $h^\pm \to W h_1$ and $h_3 \to WW$, but as the involved Higgs–gauge boson couplings are small, the BRs are tiny. Here, the LSP with a mass $m_{\chi_1^0} \sim 70$ GeV, is a bino–like neutralino but it has a small non–negligible higgsino component. The value $\Omega_{\rm CDM} h^2 \simeq 0.1$ is achieved through the annihilation processes $\chi_1^0 \chi_1^0 \to b\bar{b}, \tau^+\tau^-$, with s–channel exchange of Higgs bosons.

17.4 Expectations at the LHC

In the cases discussed here, at least one CP–even Higgs particle h_i has strong enough couplings to massive gauge bosons and top quarks, $R_i, t_i \sim 1$, to allow for the production at the LHC in one of the main channels which are advocated for the search of the SM Higgs particle [284]: $i)$ gluon–gluon fusion, $gg \to h_i$, $ii)$ vector boson fusion (VBF), $qq \to qqW^*W^*, qqZ^*Z^* \to qqh_i$ with two forward jets and a centrally decaying Higgs boson, $iii)$ Higgs–strahlung (HS), $q\bar{q}' \to Wh_i$ and $q\bar{q} \to Zh_i$, with the gauge boson decaying leptonically, $iv)$ associated production with heavy top quark pairs $q\bar{q}/gg \to t\bar{t}h_i$.

In scenarios P1 to P3, this CP–even h_i particle is the h_1 boson which has $R_1 \simeq t_1 \simeq b_1 \simeq 1$, but which decays most of the time into a pair of light pseudoscalar Higgs particles, $h_1 \to a_1 a_1$, which subsequently decay into light fermion pairs, $a_1 \to b\bar{b}$ and $\tau^+\tau^-$. In scenario P4, this particle is the h_2 boson which decays most of the time into a pair of h_1 particles, $h_2 \to h_1 h_1$, which again decay into light fermion pairs. In these four cases, the backgrounds in both $gg \to h_i \to 4f$ and $qq/gg \to t\bar{t}h_i \to t\bar{t}+4f$, with $f = b, \tau$, processes will be extremely large and only the VBF (owing to the forward jet tagging) and eventually HS (due to the leptons coming from the decays of the gauge bosons) can be viable at the LHC. In P5, the particle that has couplings to gauge bosons and top quarks close to those of the SM Higgs boson is the h_2 boson which decays into $b\bar{b}$ and $\tau^+\tau^-$ final states with BRs close to 90% and 10%, respectively. Here again, the gg fusion and presumably associated production with top quarks cannot be used since the interesting decays such as $h_2 \to WW^*, ZZ^*$ and $\gamma\gamma$ are suppressed compared to the SM case. Thus, in this case, only the channels $qq \to qqh_2 \to qq\tau^+\tau^-$ and eventually $q\bar{q}' \to Wh_2 \to \ell\nu b\bar{b}$ seem feasible. The state h_1 has still non–negligible couplings to gauge bosons and top quarks which lead to cross sections that are "only" one order of magnitude smaller than in the SM. Since here again,

only the decays $h_1 \to b\bar{b}$ (90%) and $\tau^+\tau^-$ (10%) are relevant, the only channels which can be used are the VBF and HS processes discussed above, but one needs a luminosity 10 times larger to have the same event samples as in the SM.

Several theoretical studies have been performed in the past to assess the potential of the LHC to observe NMSSM Higgs particles in some scenarios close to those presented here; see Ref. [283] for an account. Recently, the ATLAS and CMS collaborations started investigating some channels, the main focus being on the VBF production process $pp \to qqh_1$ and to a lesser extent HS via $q\bar{q} \to Wh_1 \to \ell\nu h_1$, with the SM–like h_1 state decaying into $h_1 \to a_1a_1 \to 4\tau$, corresponding to scenario P2 and P3. The ATLAS collaboration is analyzing the $4\mu + 4\nu_\tau + 4\nu_\mu$ channel from VBF, requiring three leptons to be observed and, for triggering, one or two high–p_T leptons ($p_T > 20$ or 10 GeV) [285]. CMS is currently considering the $\mu^\pm\mu^\pm\tau^\mp_{\rm jet}\tau^\mp_{\rm jet}$ final state containing two same sign muons and two τ jets [286]. Despite of the missing energy and the possibility of missing one lepton, the mass of the h_2 state could be reconstructed with the help of the collinear approximation. The performance of the algorithms to observe the signals and the effects of the various backgrounds are under study.

17.5 Conclusions

The NMSSM is a very interesting supersymmetric extension of the SM as it solves the notorious μ problem of the MSSM and it has less fine tuning. It also leads to an interesting collider phenomenology in some cases, in particular in the Higgs sector, which is extended to contain an additional CP–even and a CP–odd state. Compared to the SM and MSSM, the searches for the NMSSM Higgs bosons will be rather challenging at the LHC in scenarios in which some neutral Higgs particles are very light, opening the possibility of dominant Higgs-to-Higgs decays, or when all Higgs bosons have reduced couplings to the electroweak gauge bosons and to the top quarks. These scenarios, for which we have provided benchmark points in a semi–unified NMSSM which involves a rather limited number of input parameters at the grand unification scale and which fulfills all present collider and cosmological constraints, require much more detailed phenomenological studies and experimental simulations to make sure that at least one Higgs particle of the NMSSM will be observed at the LHC.

Acknowledgments

We acknowledge support from The Leverhulme Trust, the Royal Society (London, UK), the A. von-Humboldt Foundation, the FP7 RTN MRTN-CT-2006-035505 HEPTOOLS, the Indo–French Center IFCPAR for the project 3004-2 and the French ANR for the project PHYS@COL&COS.

18. PARAMETER SCANS IN TWO INTERESTING NMSSM SCENARIOS [31]

18.1 Introduction

In the past, proposals for interesting points in the parameter space of the *Next-to-Minimal Supersymmetric Standard Model* (NMSSM) [287–292] have been made (see e.g. Refs. [293–295]). A new study proposes benchmark points for the constrained NMSSM [296]. To evaluate the discovery potential of NMSSM particles at collider experiments like the *Large Hadron Collider* (LHC)[32], it is furthermore desirable to define two-dimensional benchmark scans which include regions of typical and experimentally challenging NMSSM phenomenology. In the following, two such parameter scans over the Higgs sector of the NMSSM are proposed for this model. Both scans include a benchmark point from Ref. [295].

[31] Contributed by: I. Rottländer and M. Schumacher

[32] A proton-proton collider with a design center-of-mass energy of 14 TeV. First physics runs are expected for 2008.

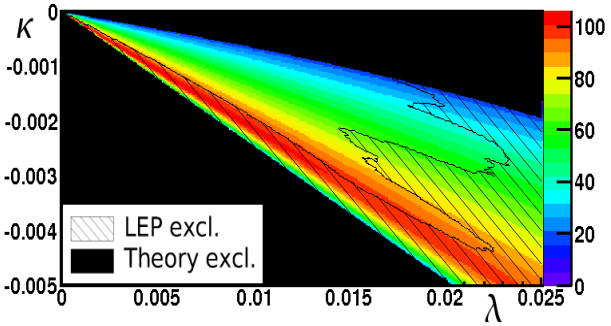

Fig. 39: H_1 mass [GeV] in the *Reduced Couplings Scenario*

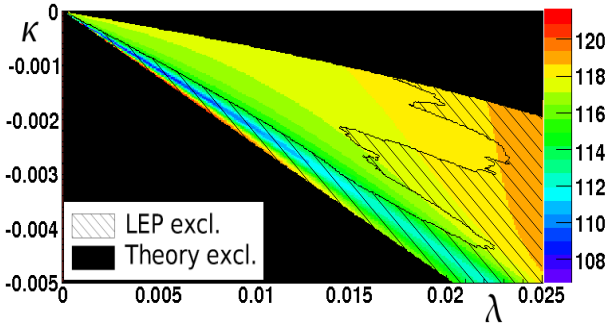

Fig. 40: H_2 mass [GeV] in the *Reduced Couplings Scenario*

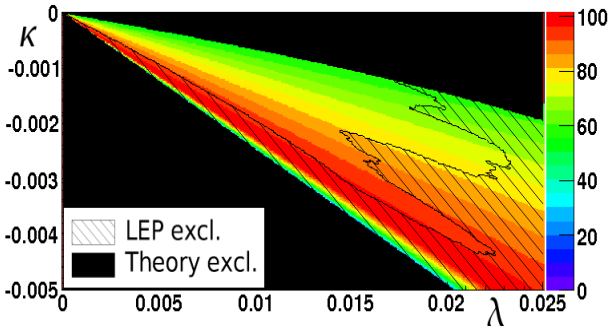

Fig. 41: A_1 mass [GeV] in the *Reduced Couplings Scenario*

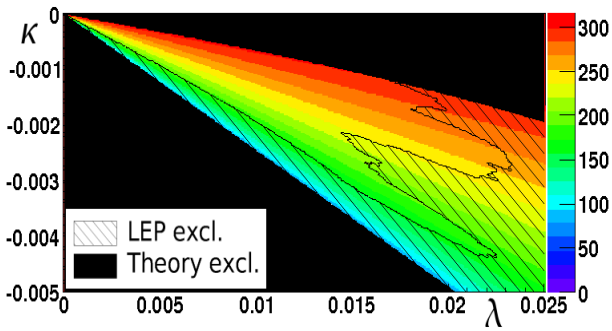

Fig. 42: $H^{\pm}$ mass [GeV] in the *Reduced Couplings Scenario*

18.2 The NMSSM

In the *Minimal Supersymmetric Standard Model* (MSSM), the value of the Higgs-Higgsino mass parameter μ is not confined by theory, but it is experimentally constrained to lie at the weak scale or else large fine-tuning is required (the so called μ-*problem*). In the NMSSM, an additional neutral singlet superfield S is added to the MSSM. After symmetry breaking, μ is then given by the product of the vacuum expectation value of the bosonic component of S ($<s>$) and a new coupling constant λ. Constraints from the Higgs potential minimization strongly prefer $<s>$ to lie at the weak scale. The right value of μ is thus obtained naturally.

The resulting model contains the whole particle spectrum of the MSSM with an additional neutral scalar boson, a pseudoscalar boson and a neutral fermion (”singlino”). The two additional neutral scalar bosons contained in S mix with the MSSM Higgs bosons to form the five neutral Higgs bosons of the NMSSM: three CP-even bosons H_1, H_2, H_3 and two CP-odd Higgs bosons A_1, A_2. The neutral fermion mixes with the four neutralinos of the MSSM, thus, the model contains in total five neutral fermion states. Since no charged particles are added, the features of the other MSSM particles, including the charged Higgs boson $H^{\pm}$, are only modified marginally. The maximally allowed mass of the lightest NMSSM scalar H_1 is about 10 GeV higher than the bound for h in the MSSM [297].

In the NMSSM, the Higgs sector can at tree level be described by six parameters. Usually, these are chosen to be the coupling parameters of S (λ, κ, A_λ, A_κ), μ and the ratio of the vacuum expectation values of the Higgs fields, $\tan\beta$. In the here defined two-dimensional parameter scans, λ and κ are varied. Variation of the other parameters also changes the features of the Higgs sector, however, a λ-κ variation was found to be sufficient to cover the most important phenomenology types in the two scans described here.

To calculate the NMSSM particle spectra and exclusion constraints from theory and LEP[33], the program NMHDECAY [298–300] was used. The mass parameters were chosen as $M_1 = 500$ GeV, $M_2 = 1$ TeV,

[33]The *Large Electron Positron Collider*, which ran until 2000 at center-of mass energies up to 209 GeV.

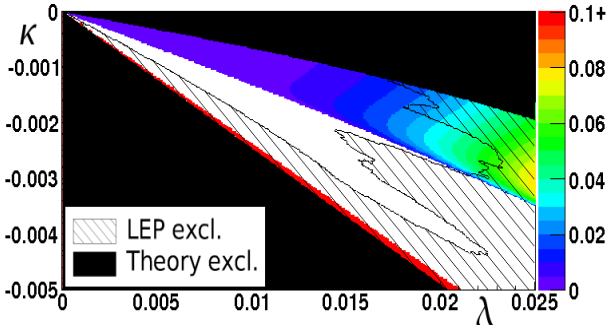

Fig. 43: $H_2 \to H_1 H_1$ branching ratio in the *Reduced Couplings Scenario*

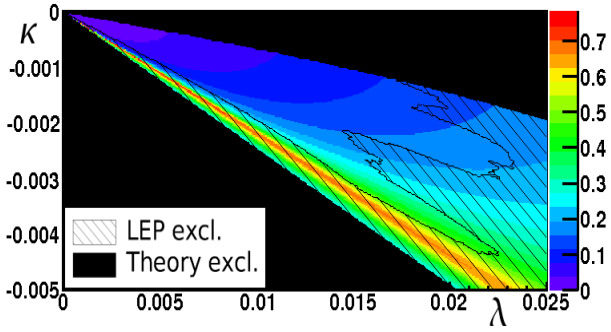

Fig. 44: H_1 vector boson coupling relative to its SM-value in the *Reduced Couplings Scenario*

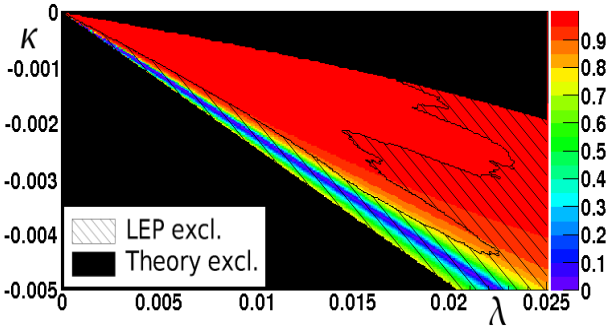

Fig. 45: H_2 vector boson coupling relative to its SM-value in the *Reduced Couplings Scenario*

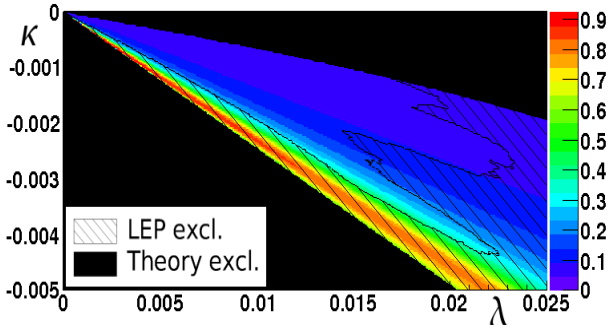

Fig. 46: H_3 vector boson coupling relative to its SM-value in the *Reduced Couplings Scenario*

$M_3 = 3$ TeV and $M_{susy} = 1$ TeV. The trilinear soft supersymmetry-breaking parameters were set to $A_t = A_b = A_\tau = 1.5$ TeV, the top quark mass to 172 GeV.

18.3 The Reduced Couplings Scenario

Due to the mixing with the gauge singlet states, the NMSSM Higgs bosons can have reduced gauge couplings and thus reduced production cross sections compared to the *Standard Model* (SM) or the MSSM case. A light scalar with reduced gauge couplings and a mass below 114 GeV is still unexcluded by LEP.

The here proposed scenario is a λ-κ scan with parameters given in Table 19. The point with $\lambda = 0.0163$ and $\kappa = -0.0034$ is described as having the lowest statistical significance found in a region without Higgs-to-Higgs decays in Ref. [295].

The masses of all six Higgs bosons in this scenario are smaller than about 300 GeV. The H_1 is very light, down to values of about 20 GeV in an unexcluded region with small negative κ (Fig.39). Since the H_2 has a SM-like mass around 120 GeV in the entire plane (Fig.40), there is a region where the decay $H_2 \to H_1 H_1$ is allowed with a small branching ratio of at maximum 6% in the unexcluded region (Fig.43). The A_1 mass ranges from about 55-100 GeV (Fig.41) in the allowed parameter region, whereas the H_3, A_2, and $H^\pm$ are approximately degenerate in the entire plane, but with small differences in mass for large negative κ. The mass of the H_3 ranges from about 150 to 300 GeV, the mass of the A_2 from about 140 to 300 GeV and the charged Higgs boson mass from about 165 to 300 GeV in the unexcluded region (Fig.42).

In Figures 44, 45 & 46, the vector boson couplings of the scalar bosons are given as an example gauge coupling. Higgs boson couplings to gluons and up-type fermions vary similarly. The H_1 and H_3 gauge

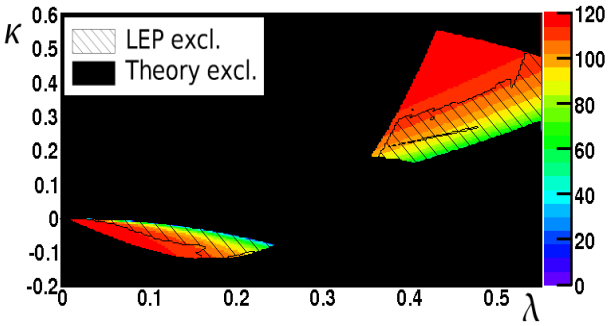

Fig. 47: H_1 mass [GeV] in the *Light* A_1 *Scenario*

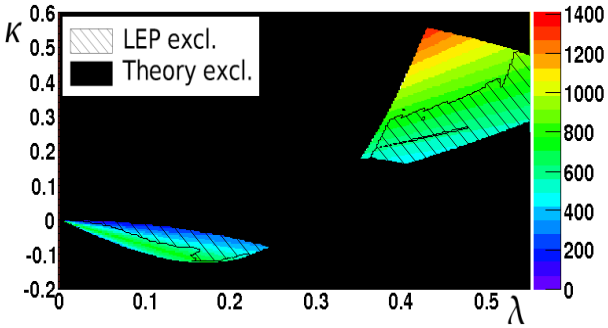

Fig. 48: H_2 mass [GeV] in the *Light* A_1 *Scenario*

couplings[34] are highly suppressed in most of the parameter plane, reaching sizeable values only in the LEP excluded region at large negative κ. The H_2 has SM-like gauge couplings in large parts of the parameter plane. In the unexcluded region close to the benchmark point from Ref. [295], the vector boson couplings are reduced down to about 80% of their SM-value. Gauge couplings of the A_1 and A_2 are highly suppressed for all considered parameter values.

To summarize, this scenario is characterized by a region with a very light H_1 close to the upper exclusion bound, where $H_2 \to H_1 H_1$ decays are possible, a region with a SM-like H_2 in the middle of the allowed parameter space, and a region with reduced couplings of the H_2 at large negative κ close to the lower exclusion bound.

Table 19: Higgs sector parameters of the proposed scenarios

Scenario	λ-range	κ-range	A_λ [GeV]	A_κ [GeV]	μ [GeV]	$\tan\beta$
Reduced couplings	0 - 0.025	-0.005 - 0	-70	-54	-284	5.7
Light A_1	0 - 0.55	-0.2 - 0.6	-580	-2.8	-520	5.0

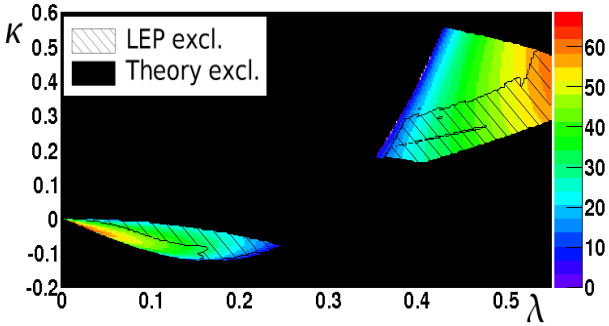

Fig. 49: A_1 mass [GeV] in the *Light* A_1 *Scenario*

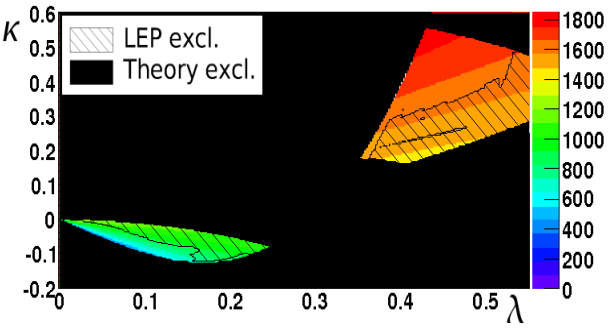

Fig. 50: $H^\pm$ mass [GeV] in the *Light* A_1 *Scenario*

18.4 The Light A_1 Scenario

Unlike in the MSSM, the mass of the lightest pseudoscalar A_1 is in the NMSSM not closely coupled to the masses of the scalar Higgs bosons and might thus lie well below the H_1/H_2 masses. In such a case,

[34] The term 'gauge couplings' here and in the following always excludes the Higgs boson coupling to down-type fermions which may be enhanced with respect to the SM-value, but are still too small to have an impact on the Higgs boson discovery potential with the here used $\tan\beta$ values around 5.

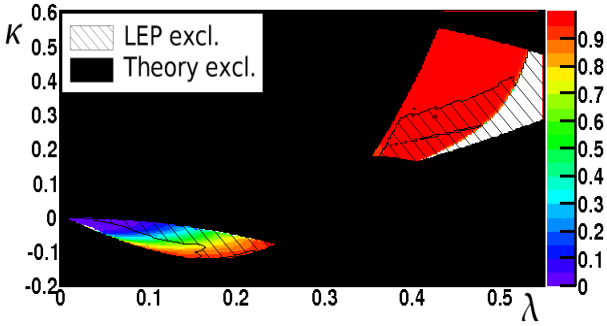

Fig. 51: $H_1 \to A_1 A_1$ branching ratio in the *Light* A_1 *Scenario*

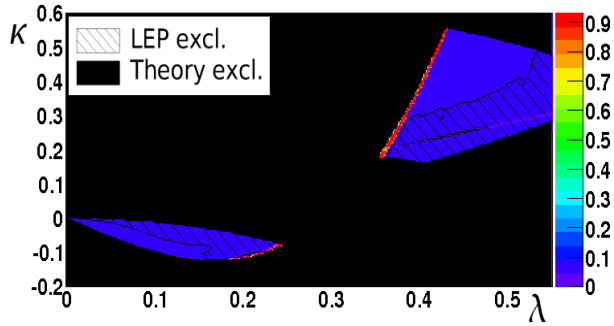

Fig. 52: $A_1 \to \tau\tau$ branching ratio in the *Light* A_1 *Scenario*

the decay chain $H_{1/2} \to A_1 A_1$ can be the dominant decay mode of the lightest scalars.
The here described scenario is also a λ-κ scan with parameters given in Table 19. The point with $\lambda = 0.22$ and $\kappa = -0.1$ has been described in Ref. [295].
Here, the lightest scalar H_1 has a mass around 120 GeV in the unexcluded region (Fig.47). The A_1 is very light with masses up to about 60 GeV (Fig.49), so that the decay $H_1 \to A_1 A_1$ is possible in the entire parameter plane with exception of a small region at very small λ and κ (Fig.51). In the unexcluded region with large λ and κ, this decay reaches branching ratios above 90%. Areas with a smaller branching ratio exists for smaller λ and κ. The other Higgs bosons are rather heavy (Figs.48,50), with the H_3, A_2 and $H^\pm$ being approximately degenerate in large parts of the parameter plane.
For A_1 masses larger than $2m_b$, about 90% of the lightest pseudoscalar bosons decay to bottom quarks. In these regions, the decay chains $H_1 \to A_1 A_1 \to b\bar{b}b\bar{b}$ and $H_1 \to A_1 A_1 \to b\bar{b}\tau\tau$ are important. In small regions at the borders of the unexcluded region, the A_1 is so light that the decay chain $H_1 \to A_1 A_1 \to \tau\tau\tau\tau$ prevails (Fig.52). In the narrow unexcluded band around $\lambda \approx 0.25$, the couplings of the A_1 to fermions are heavily suppressed. Here, the decay chain $H_1 \to A_1 A_1 \to \gamma\gamma\gamma\gamma$ is dominant.
The gauge couplings of the H_1 are SM-like in the entire allowed parameter region (Fig.53). The gauge couplings of the H_2 are sizeable only in a small excluded region with κ-values close to zero (Fig.54). All other Higgs bosons have highly suppressed gauge couplings in the entire parameter plane.

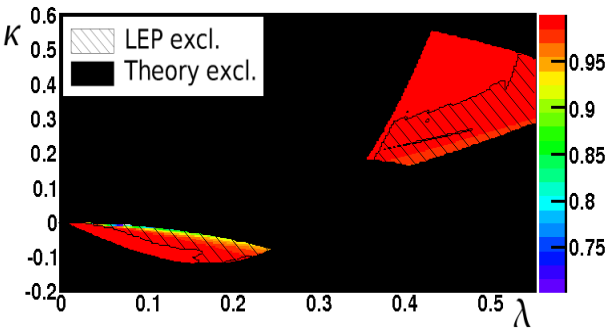

Fig. 53: H_1 vector boson coupling relative to its SM-value in the *Light* A_1 *Scenario*

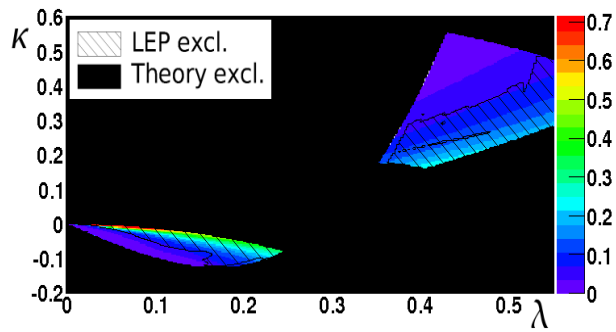

Fig. 54: H_2 vector boson coupling relative to its SM-value in the *Light* A_1 *Scenario*

18.5 Conclusions

Two interesting two-dimensional NMSSM scans were described and proposed as possible benchmarks for NMSSM Higgs boson searches. These two scans cover the four main, for the NMSSM typical phenomenology types, for which a discovery of Higgs bosons at future experiments like the LHC might be difficult:

- A region with very light scalar H_1.

- A region with reduced gauge couplings of an otherwise SM-like scalar H_2.
- Regions with dominant $H_1 \to A_1 A_1 \to b\bar{b}b\bar{b}/b\bar{b}\tau\tau$ decays of an otherwise SM-like scalar H_1.
- Regions with dominant $H_1 \to A_1 A_1 \to \tau\tau\tau\tau$ decay of an otherwise SM-like scalar H_1.

Another example of an experimentally challenging phenomenology type not covered here is a dominant $H_1 \to c\bar{c}$ decay [294]. Also the region where the mass of the lightest scalar is maximal [297] could prove interesting for Higgs boson discovery .

19. THE NMSSM NO-LOSE THEOREM AT THE LHC: THE SCOPE OF THE 4τ CHANNEL IN HIGGS-STRAHLUNG AND VECTOR BOSON FUSION [35]

19.1 Introduction

As emphasised in Sect. 17. (see also [283]), the NMSSM has obvious advantages with respect to the MSSM. In constrast, it is not certain that at least one Higgs boson can be found at the LHC in such a scenario. In this respect, of particular relevance are $h_1 \to a_1 a_1$ decays, as they have been claimed to be the only means to establish a no-lose theorem at the CERN machine for the NMSSM [185, 293, 294, 301–307], at least over a region of parameter space where Supersymmetry (SUSY) partners of ordinary Standard Model (SM) objects are made suitable heavy. Here, a_1 states are rather light (of 10 GeV or less) while h_1 ones could well be below the LEP limit on the SM Higgs mass, of 114 GeV (albeit with weakened couplings to ordinary matter). The scope of $h_1 \to a_1 a_1$ decays into $jj\tau^+\tau^-$ pairs (where j represents a jet of either heavy or light flavour and where the τ's decay leptonically) has been found to be rather questionable [308]. Hence, in this contribution we investigate the scope of the 4τ channel, wherein two τ's are searched for in their muonic decays while the other two are selected via their hadronic ones. We will consider both HS and VBF as production channels. Finally, to enhance the yield of $a_1 \to \tau^+\tau^-$ decays, we limit ourselves to regions of NMSSM parameter space where $M_{a_1} < 2m_b$ (light a_1 scenario).

19.2 The Low-Energy NMSSM Parameter Space For The Light a_1 Scenario

In this section we investigate the NMSSM parameter space setups which yield the $M_{a_1} < 2m_b$ mass configuration, with particular interest to the cases where the aforementioned $h_1 \to a_1 a_1 \to 4\tau$ decays may be visible at the LHC if happening in conjunction with HS and/or VBF production processes of Higgs bosons. Notice that there are altogether fourteen parameters that uniquely define at the Electro-Weak (EW) scale the NMSSM Higgs sector for the purposes of our analysis. With reference to notation already defined elsewhere in this report, these are: $\tan\beta, \lambda, \kappa, A_\lambda, A_\kappa, M_1, M_2, M_3, A_t, A_b, A_\tau, M_{f_L}$ and M_{f_R}, where M_{f_L} and M_{f_R} denote the soft SUSY breaking slepton and squark mass parameters. We will start by establishing the portion of NMSSM parameter space, defined in terms of the above inputs, that survives present theoretical and experimental constraints.

19.21 Full NMSSM Parameter Scan

The numerical values over which the parameters introduced above have been scanned are:

$$-1000 \text{ GeV} < A_\kappa < 100 \text{ GeV}, \quad -10 \text{ TeV} < A_\lambda < 10 \text{ TeV}, \quad 100 \text{ GeV} < \mu < 1000 \text{ GeV},$$
$$10^{-5} < \lambda, \kappa < 0.7, \quad 1.5 < \tan\beta < 50 \tag{34}$$

while the remaining parameters were fixed at

$$M_1/M_2/M_3 = 150/300/1000 \text{ GeV}, \quad A_t = A_b = A_\tau = 2.5 \text{ TeV}, \quad M_{f_L} = M_{f_R} = 1 \text{ TeV}. \tag{35}$$

We will call the scan performed over such intervals a 'wide' scan. This (as well as all those in the remainder of this note) has been performed by using the NMSSMTools package [298–300], which calculates

[35] Contributed by: Alexander Belyaev, Stefan Hesselbach, Sami Lehti, Stefano Moretti, Alexander Nikitenko, Claire H. Shepherd-Themistocleous

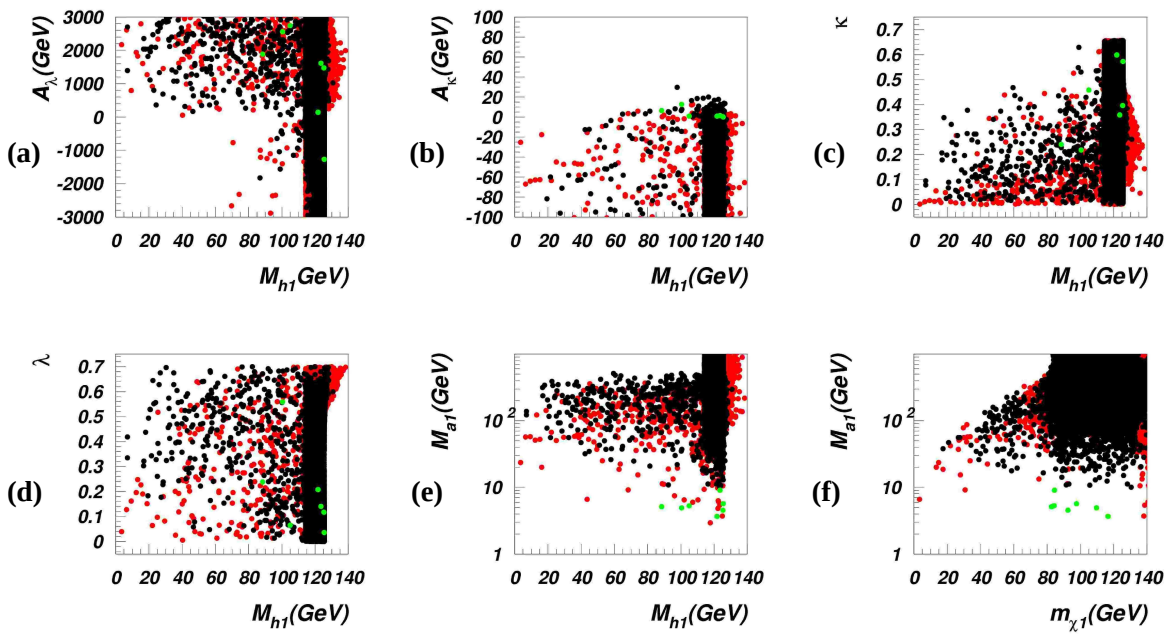

Fig. 55: Result of the NMSSM 'wide' scan mapped onto the planes: (a) $[A_\lambda, M_{h_1}]$, (b) $[A_\kappa, M_{h_1}]$, (c) $[\kappa, M_{h_1}]$, (d) $[\lambda, M_{h_1}]$, (e) $[M_{a_1}, M_{h_1}]$, (f) $[M_{a_1}, m_{\chi_1^0}]$. Colour code: red – all constraints are satisfied but relic density (above WMAP constraint: $\Omega h^2 > 0.11$); black – all constraints are satisfied, $M_A > 10$ GeV; green – all constraints are satisfied, $M_A < 10$ GeV.

NMSSM spectra (masses, couplings and decay rates) and takes into account experimental inputs including LEP limits, B-physics bounds as well as (cold) DM constraints. In Fig. 55 we present the results of this scan. Though only a few $M_{a_1} < 10$ GeV points survive, one can see from Fig. 55(a) the preference for a large positive A_λ while Fig. 55(b) indicates that small $|A_\kappa|$'s are preferred.

19.22 Scan for Narrowed A_κ

The results of Fig. 55 (specifically, the preference for small A_κ's) motivated us to 'narrow' the range of the parameters, by scanning it over the intervals

$$-15\ \text{GeV} < A_\kappa < 20\ \text{GeV}, \quad -2\ \text{TeV} < A_\lambda < 4\ \text{TeV}, \quad 100\ \text{GeV} < \mu < 300\ \text{GeV}, \tag{36}$$

and the rest of the parameters as in Eq. (34). Fig. 56 makes the point that this is precisely the region where a large portion of NMSSM points with $M_{a_1} < 10$ GeV are found, consistent with all known constraints. Now we can clearly see certain correlations onsetting in the $M_{a_1} < 10$ GeV region: 1. values of $A_\lambda > 0$ are preferred, see Fig. 56(a); 2. points with low M_{h_1}, $A_k \sim 0$ (Fig. 56(b)) and small values of κ (Fig. 56(c)) are preferred; 3. we can see interesting $M_{a_1} < 10$ GeV points with also low, down to 20 GeV, M_{h_1} values (Fig. 56(e)).

19.23 Final Scan For the Light a_1 Scenario

We have then performed one 'final' scan over the NMSSM parameter space by requiring at the same time $M_{a_1} < 10$ GeV and Eq. (36). Having already learnt the size of such portion of the entire NMSSM parameter space after experimental constraints, we now want to characterise it in terms of the quantities which enter the event rates for $h_1 \to a_1 a_1 \to 4\tau$ decays produced via HS and VBF. The results of this scan are shown in Fig. 57. Note that, here, the colours were chosen to indicate the measure of decoupling of the lightest CP-even Higgs boson, h_1, from the SM limit (denoted simply by H). To this aim, we have defined the measure $R_{ZZh} = \left(g^{\text{NMSSM}}_{ZZh_1}/g^{\text{SM}}_{ZZH}\right)^2$, i.e., the ratio of the coupling strength (squared)

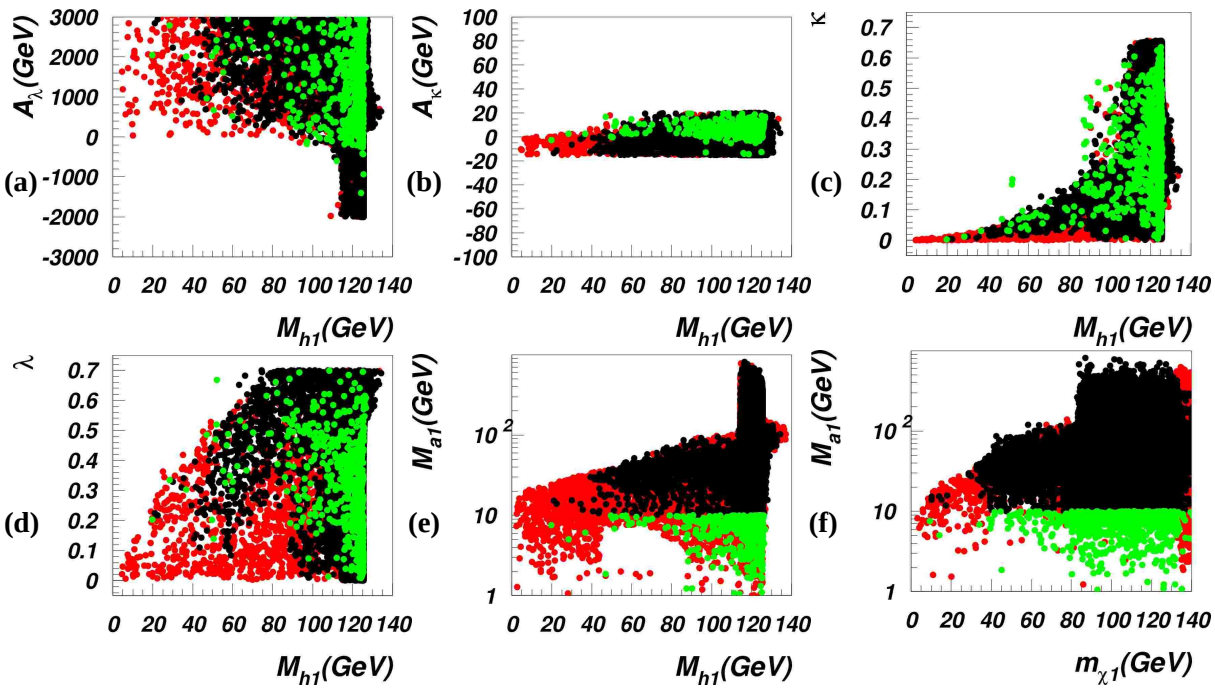

Fig. 56: Results of the NMSSM 'narrow' scan, i.e., analogous to Fig. 55 but for -15 GeV $< A_\kappa <$ 20 GeV, -2 TeV $< A_\lambda <$ 4 TeV, 100 GeV $< \mu <$ 300 GeV. The individual plots and the colour code are the same as in Fig. 55.

of the ZZh_1 vertex in the NMSSM relative to the SM case (in fact, this is the same for couplings to $W^\pm$ gauge bosons). One should notice that both HS, $pp \to Vh_1$, and VBF, $pp \to jjV^*V^* \to jjh_1$, rates ($V = Z, W^\pm$) are directly proportional to R_{ZZh} and are suppressed in the non-decoupling regime whenever R_{ZZh} is essentially smaller then unity. From Fig. 57 one can see the following important features of the $M_{a_1} < 2m_b \approx 10$ GeV scenario: 1. the lighter the Higgs the more significant should be the NMSSM deviations from the SM case, e.g., for any $M_{h_1} < 50$ GeV any R_{ZZh} is limited to be < 0.5, as dictated by LEP constraints [4, 270] (this correlation is illustrated in a more clear way in Fig. 58(a), presenting the R_{ZZh} versus M_{h_1} plane, which exhibits the typical pattern of the LEP Higgs exclusion curve [270]); 2. in the $M_{h_1} < 40$ GeV region A_λ is always positive (Fig. 57(a)), $\kappa < 0.1$ (Fig. 57(c)) while $\lambda < 0.45$ (Fig. 57(d)). In this case, one should notice the correlation between the singlet nature of the h_1 and the singlino component of the lightest neutralino, which is visually depicted in Fig. 58(b). Finally, it is also worth to point out the correlation between their masses in Fig. 58(c). From these plots, one can see a striking correlation between the lightest neutralino and Higgs boson whenever one has that $M_{h_1} < 50$ GeV. In this connection, one should stress that the NMSSM model structure requires h_1 to be a singlet and χ_1^0 to be a singlino (for $M_{a_1} < 10$ GeV and $M_{h_1} < 10$ GeV) in order to have a relic density consistent with current experimental constraints. In fact, over the NMSSM parameter space restricted to having $M_{a_1} < 10$ GeV and $M_{h_1} < 10$ GeV, the χ_1^0-pair annihilation in the early Universe proceeds through the h_1-funnel region. So, in this region, $2m_{\chi_1^0} \simeq M_{h_1}$ as we observe from the lower-left part of Fig. 58(c).

19.3 Phenomenology of the Light a_1 Scenario

As final step of our analysis, we combined the production rates of HS and VBF with selection efficiencies determined by generating these processes within the PYTHIA Monte Carlo (including smearing effects). The latter have been estimated in presence of cuts, after parton shower, hadronisation plus heavy hadrons decays (and with underlying event turned on). For HS we enforced (assuming e, μ decays of the $W^\pm$) $\tau^+ \to \mu\nu\nu$ and $\tau^- \to$ hadrons and the selection cuts were

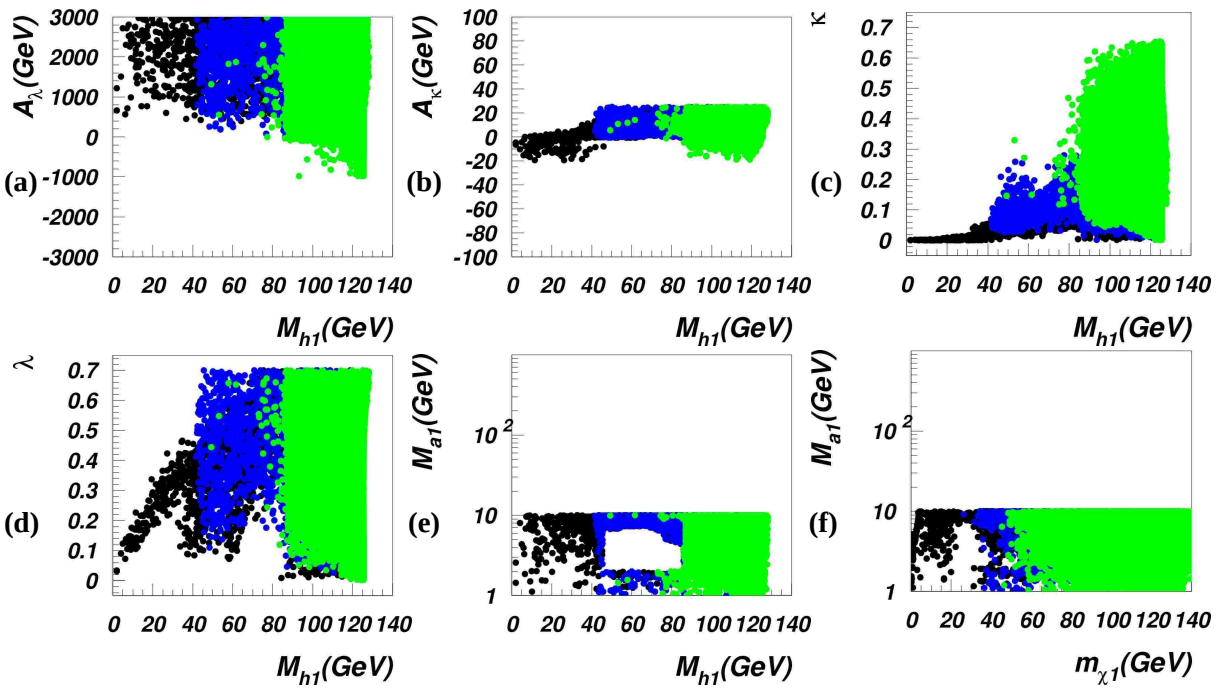

Fig. 57: Results of the NMSSM 'final' scan, i.e., with $M_{a_1} < 10$ GeV and with Eq. (36) enforced. The black, blue and green colours indicate the cases $R_{ZZh} < 0.1$, $0.1 < R_{ZZh} < 0.5$ and $R_{ZZh} > 0.5$, respectively (where R_{ZZh} is defined in the text). The individual plots are the same as in Fig. 55.

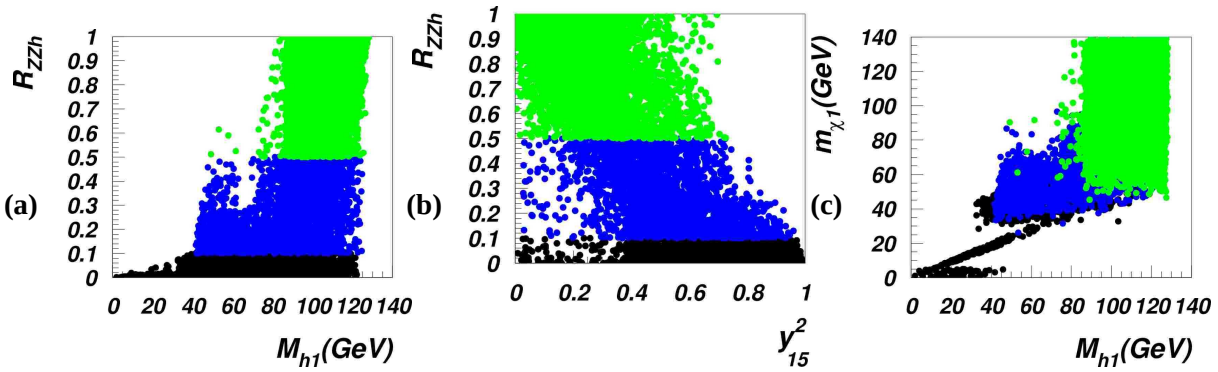

Fig. 58: Results of the NMSSM 'final' scan, i.e., with $M_{a_1} < 10$ GeV and with Eq. (36) enforced: (a) R_{ZZh} (see text) versus M_{h_1}, (b) R_{ZZh} versus the singlino component y^2_{15} of the lightest neutralino χ^0_1, (c) $m_{\chi^0_1}$ versus M_{h_1}. The colour coding is the same as in Fig. 57.

• Trigger selection: isolated single muon or single electron found with thresholds 19 and 26 GeV, respectively, $|\eta| < 2.5$. • Muon $\mathrm{p_T} > 7$ GeV, $|\eta| < 2.1$. • Tau jet $\mathrm{E_T} > 10$ GeV, $|\eta| < 2.1$. • Isolated 1-prong τ's within $\Delta R < 0.6$ from the muon using tracker isolation for tracks $p_\mathrm{T} > 2$ GeV. • Tau and muon oppositely charged. • Two tau + muon pairs found.

For VBF the selection cuts were

• Two same sign muons with $\mathrm{p_T} > 7$ GeV, $|\eta| < 2.1$ and with one track of $\mathrm{p_T} > 2$ GeV in cone 0.6 around each muon. • Two τ jets with $\mathrm{E_T} > 10$ GeV, $|\eta| < 2.1$. • Two jets with $\mathrm{E_T} > 30$ GeV, $|\eta| < 4.5$.

The results in Fig. 59 show that, after our final scan, the population of parameter points is such that in both channels the highest cross sections are found for $M_{h_1} \gtrsim 80$ GeV, although in the case of VBF also lower h_1 masses can yield sizable rates, but never for values less than 40 GeV. Independently of M_{h_1},

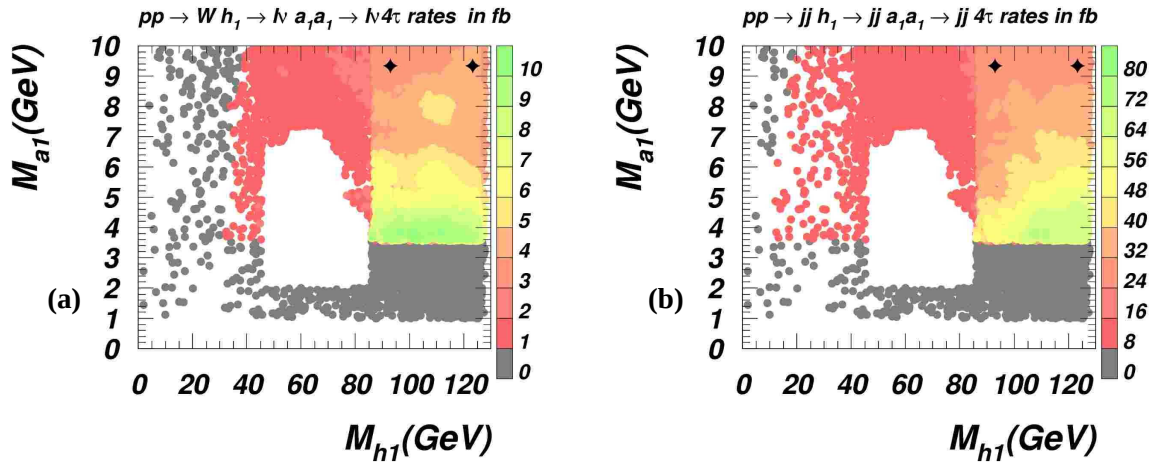

Fig. 59: Cross sections (including all relevant branching ratios) for HS (a) and VBF (b) after the selection cuts described in the text. The population of points used correspond to that of the 'final scan' described previously. Black diamonds correspond to the benchmark P2 (right) and P3 (left) from Ref. [283].

the a_1 mass enables sizable event rates anywhere above $2m_\tau$, but particularly just above the threshold. At high luminosity, 100 fb^{-1}, the highest rates would correspond to 1000 events per year for HS and 8000 for VBF.

19.4 Conclusions

We have shown that there is significant potential in establishing a no-lose theorem for the NMSSM at the LHC via (marginally) HS and (primarily) VBF production of the lightest CP-even Higgs boson h_1 decaying into $a_1 a_1$ pairs in turn yielding four τ leptons, searched for through their semi-leptonic/hadronic decays into muons and jets. To enhance the decay fraction into τ's of the lightest CP-odd Higgs boson a_1 we have restricted ourselves to the case $M_{a_1} < 2m_b$ (otherwise $a_1 \to b\bar{b}$ decays are dominant). We have also found that the h_1 state can be very light, indeed at times lighter than the a_1. However, this last configuration can only be achieved in a low-energy NMSSM setup, with no unification assumptions at the high scale. In fact, we are currently investigating whether such light h_1 masses can be found in a less constrained version of the cNMSSM discussed in [283]. Finally, with reference to the NMSSM benchmarks discussed in [283], we should like to point out here that those relevant to our 4τ channels are P2 and P3. We have reported the cross section times efficiency rates for these two points in Fig. 59 (black diamond symbols, P2 to the right and P3 to the left). As it can be appreciated, they correspond to event rates that are mid range amongst all those explored, hence not particularly biased towards a far too favourable NMSSM setup, yet susceptible to experimental discovery. Our summary is preliminary, as only signal processes have been considered and only in presence of MC simulations, with no backgrounds and detector performance enabled. The latter clearly ought to be investigated before drawing any firm conclusions and this is currently being done.

Acknowledgements

SM thanks the Royal Society (London, UK) for financial support in the form of a Conference Grant to attend the workshop.

20. INVESTIGATION OF THE LHC DISCOVERY POTENTIAL FOR HIGGS BOSONS IN THE NMSSM [36]

20.1 Introduction

The *Large Hadron Collider* (LHC) will deliver proton-proton collisions at a center-of-mass energy of 14 TeV. First physics runs are expected for 2008. First, the LHC will operate at low luminosity ($2 \cdot 10^{33}\text{cm}^{-2}\text{s}^{-1}$). Later, the luminosity will be increased to its design value of $10^{34}\text{cm}^{-2}\text{s}^{-1}$. One of the main aims of the ATLAS [309] and CMS [98] experiments at the LHC is the search for the Higgs boson. In the Standard Model (SM) electroweak symmetry breaking is achieved via the introduction of one Higgs doublet. Only one neutral Higgs boson is predicted. Extended Higgs sectors, with additonal Higgs doublets and Higgs singlets give rise to several neutral and charged Higgs bosons, e.g. the two Higgs doublets of the Minimal Supersymmetric Extension of the SM (MSSM) yield three neutral and two charged Higgs bosons. Detailed studies have shown that the SM Higgs boson will be observable at ATLAS and CMS [98, 108, 309]. The discovery of one or more Higgs bosons of the CP-conserving MSSM will be possible [310]. Previous studies claim that at least one Higgs boson of the Next-to-Minimal Supersymmetric Standard Model (NMSSM) will most likely be observable at the LHC [293, 302]. Here, we present an evaluation of the discovery potential for NMSSM Higgs bosons based on current ATLAS studies [108, 263, 309, 311–319].

20.2 The NMSSM Higgs Sector

In the framework of the NMSSM, the μ-*problem* of the MSSM is solved by the introduction of an additional neutral singlet superfield S [290]. The two additional neutral scalar bosons contained in S mix with the MSSM Higgs bosons to form the five neutral Higgs bosons of the NMSSM: three CP-even bosons H_1, H_2, H_3 and two CP-odd Higgs bosons A_1, A_2. The phenomenology of the charged Higgs boson $H^{\pm}$ is only modified marginally with respect to the MSSM. The Higgs sector of the NMSSM at Born level is determined by the four coupling parameters of the singlet superfield, λ, κ, A_λ, A_κ, and the two parameters μ and $\tan\beta$. For a more detailed description of the NMSSM Higgs sector see e.g. Refs. [290, 320].

20.3 Evaluation of the Discovery Potential

Two two-dimensional benchmark scenarios are investigated in this study: the *Reduced Couplings Scenario* and the *Light A_1 Scenario* which were proposed during this workshop (for details see these proceedings). The parameters λ and κ are varied in meaningful ranges whereas the other parameters are fixed as described previously in this report. The method of evaluation of the discovery potential is similar to the study performed for the MSSM in Ref. [310].

20.31 Calculation of masses and events rates in the NMSSM

NMHDECAY [298, 299] was used to calculate the masses, branching ratios and decay widths of the NMSSM Higgs bosons and the couplings of the neutral Higgs bosons to fermions and gauge bosons, relative to the respective SM couplings. Couplings to gluons relative to the SM couplings were calculated from the ratio of partial widths of $H \to gg$ in the NMSSM and the SM [188] as in Eq.37.

$$\frac{g^2_{Hgg,NMSSM}}{g^2_{Hgg,SM}} = \frac{\Gamma(H \to gg)_{NMSSM}}{\Gamma(H \to gg)_{SM}} \tag{37}$$

For the neutral Higgs bosons, leading order SM cross sections [115] were scaled according to Eq.38.

$$\sigma_{NMSSM} = \sigma_{SM} \cdot \frac{g^2_{NMSSM}}{g^2_{SM}} \tag{38}$$

[36] Contributed by: I. Rottländer and M. Schumacher

Table 20: Included search topologies with allowed mass ranges.

Search Channel	**Mass Range [GeV]**	**Refs.**
VBF, $H\to\tau\tau$	110-150	[108]
VBF, $H\to WW\to ll\nu\nu$	110-200	[108]
VBF, $H\to WW\to l\nu h$	130-200	[108]
VBF, $H\to\gamma\gamma$	110-160	[311]
ttH, $H\to b\bar{b}$	70-150	[312]
GGF, $H\to ZZ\to 4l$	120-420	[309]
GGF, $H\to WW\to ll\nu\nu$	140-200	[313]
WH, $H\to WW\to ll\nu\nu$, W$\to$lν	150-190	[309]
Inclusive $H\to\gamma\gamma$	70-160	[309]
Inclusive $A\to\gamma\gamma$	200-450	[309]
WH, ZH, ttH, $H\to\gamma\gamma$	70-150	[309]
bbH, $H/A\to\tau\tau\to$hh	450-800	[314]
GGF, bbH, $H/A\to\tau\tau\to l\nu$h	150-800	[315]
GGF, bbH, $H/A\to\mu\mu$	70-450	[316, 317]
GGF, $H\to hh\to\gamma\gamma$bb	230-270 / 70-100	[309]
GGF, $H\to ZA\to llb\bar{b}$	200-250 / 70-100	[309]
$gb\to H^{\pm}t$, $H^{\pm}\to\tau\nu$	175-600	[263]
$gb\to H^{\pm}t$, $H^{\pm}\to tb$	190-400	[318]
$t\bar{t}\to H^{\pm}bWb\to\tau\nu l\nu b\bar{b}$	90-165	[309]
$t\bar{t}\to H^{\pm}bWb\to\tau\nu q\bar{q}b\bar{b}$	80-165	[319]

The charged Higgs boson $gb\to tH^{\pm}$ cross sections in leading order were taken from Ref. [244] and were modified according to the $H^{\pm}tb$-couplings obtained with NMHDECAY. The branching ratio $t\to H^{\pm}b$ was calculated with Feynhiggs [246]. For $t\bar{t}$-production, a leading order cross section of 482 pb was assumed. The top quark mass was set to 172 GeV. Theoretical and LEP[37] exclusion criteria (bounds from hZ and hA searches) were calculated by NMHDECAY.

20.32 Significance Calculation

The expected number of signal events is derived from the above discussed NMSSM cross sections. Signal efficiencies are taken from published ATLAS Monte-Carlo studies (Table 20). The expected numbers of background events are also taken from published ATLAS MC studies. If MC studies at design luminosity exist, a data volume of 300 fb^{-1} is assumed; if only low luminosity studies are available, 30 fb^{-1} are used, and if both scenarios have been investigated, 30 fb^{-1} taken at low luminosity and 270 fb^{-1} taken at design luminosity are assumed. The current results only include SM background processes. Systematic uncertainties are neglected. For the significance calculation, the profile likelihood method [321] with asymptotic approximation [322] is used. To claim a discovery, a significance of at least 5σ is required. The number of expected signal events is corrected for the effects of increased Higgs boson decay widths and the possibility of degenerate Higgs boson masses as described in the following.

Corrections for large Higgs bosons widths

In the NMSSM, the natural line width of the Higgs boson may be enhanced relative to the SM case. Thus, a larger fraction of signal events may lie outside a mass window cut than in the SM. To correct for this, the Higgs boson peak was described by a Voigt-function whose Breit-Wigner part is given by the

[37] The *Large Electron Positron Collider*, which ran until 2000 at center-of mass energies up to 209 GeV.

natural line width, the Gaussian part by the detector resolution. The ratio of the integral values over the mass window for the SM and the NMSSM case was used as a correction factor.

Corrections for degenerate Higgs boson masses
Higgs boson peaks were described by a Voigt function as previously. The peaks were assumed to be indistinguishable if their separation was smaller than $2.355 \cdot$FWHM. In case of negligible Higgs boson width, this corresponds to a 2σ separation of two Gaussians. Higgs bosons with overlapping mass windows were also considered indistinguishable to avoid double counting of events. In case of inseparable peaks, contributions from all Higgs bosons were added up for each boson's mass window. Only the highest observed significance was kept and assigned to the Higgs boson with the largest fraction of signal events in that mass window.

20.4 Search Topologies

The combinations of production mechanisms and decay modes considered in the evaluation of the discovery potential and the considered mass ranges are summarised in Table 20.[38] Within the scenarios examined here, only the VBF, $H \to \tau\tau$; ttH, $H \to b\bar{b}$ and $H \to \gamma\gamma$ channels show significances greater 5σ at the given integrated luminosities in the theoretically allowed and yet unexcluded regions (see section 20.5).

20.5 Results

20.51 The Reduced Couplings Scenario

In the *Reduced Couplings Scenario*, the H_2 with a mass of about 120 GeV is SM-like in large parts of the parameter space. In an unexcluded region with large negative κ close to the lower exclusion bound, the gauge couplings of H_2 are reduced to about 80% of their SM-value. The H_1 gets very light at the region close to the upper exclusion bound, so that the decay $H_2 \to H_1 H_1$ is kinematically allowed. However, due to the small branching ratio for this decay mode of at maximum 6%, its effect on the discovery potential is negligible. The discovery potential for the H_2 is shown in Fig.60. The entire unexcluded region is covered by the ttH, $H_2 \to b\bar{b}$ channel despite the coupling reduction. The inclusive $H_2 \to \gamma\gamma$ and the VBF, $H_2 \to \tau\tau$ channels also contribute. With 30 fb^{-1}, the search for $H_2 \to \tau\tau$ will be the only sensitive channel. The region with reduced couplings will not be covered in that case. The gauge couplings of the H_1 and H_3 are sizable only at large negative κ. Here, the channels $H_3 \to \gamma\gamma$;

[38] Production modes are abbreviated GGF for gluonfusion, VBF for vector boson fusion and ttH, bbH, WH and ZH for associated production with top quarks, bottom quarks and vector bosons.

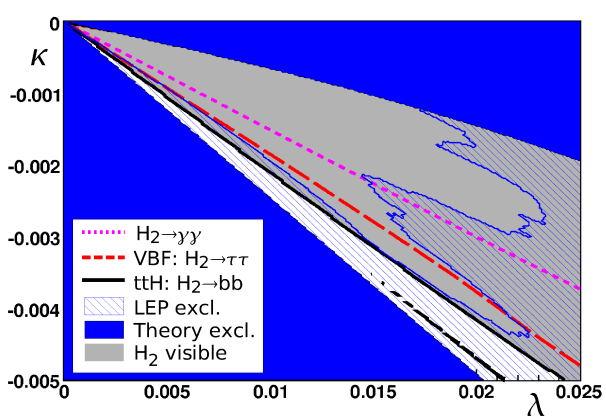

Fig. 60: 5σ discovery contours of the H_2 in the λ-κ plane for the *Reduced Couplings Scenario*

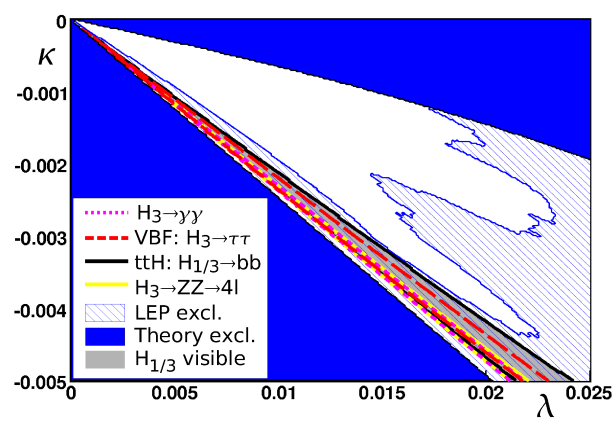

Fig. 61: 5σ discovery contours of the H_1 and H_3 in the λ-κ plane for the *Reduced Couplings Scenario*

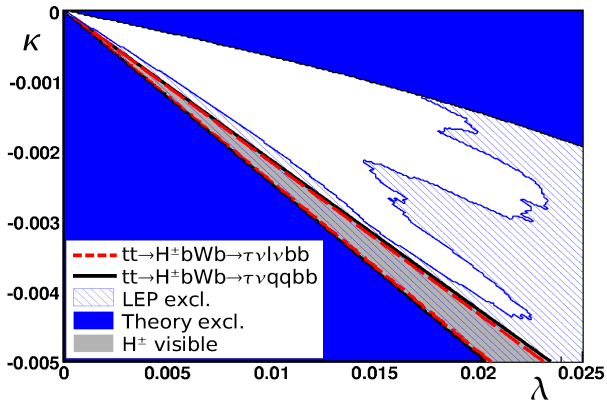

Fig. 62: 5σ discovery contours of the $H^{\pm}$ in the λ-κ plane for the *Reduced Couplings Scenario*

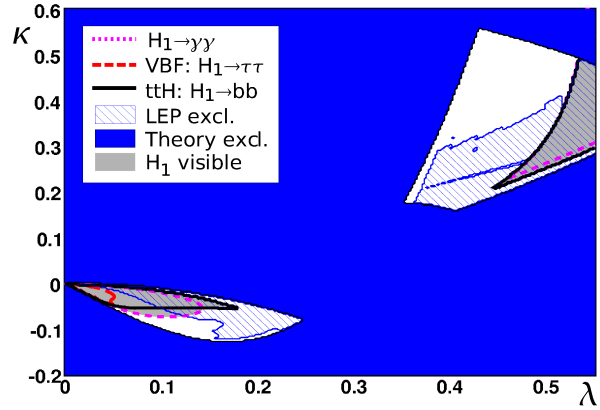

Fig. 63: 5σ discovery contours of the H_1 in the λ-κ plane for the *Light A_1 Scenario*

VBF, $H_3 \to \tau\tau$; ttH, $H_{1/3} \to b\bar{b}$ and GGF, $H_3 \to ZZ \to 4l$ contribute in a region ruled out by LEP (Fig.61). Since the charged Higgs boson is lighter than the top quark in the same region, it can be detected via the $t\bar{t} \to H^{\pm}bW^{\pm}b \to \tau\nu l\nu b\bar{b}$ and $t\bar{t} \to H^{\pm}bW^{\pm}b \to \tau\nu q\bar{q}b\bar{b}$ searches only in the LEP excluded region also (Fig.62). All other Higgs bosons have highly reduced gauge couplings and are therefore unobservable.

20.52 The Light A_1 Scenario

In this scenario, the H_1 has a mass of about 120 GeV and SM-like gauge couplings. Since the A_1 is light, $H_1 \to A_1 A_1$ decays are kinematically possible and often dominant. In the upper right unexcluded region, the branching ratio of $H_1 \to A_1 A_1$ is larger than 90%. Here, the H_1 cannot be observed (see Fig.63). The branching ratio of $H_1 \to A_1 A_1$ drops for small λ and κ. Therefore, a discovery via the inclusive and associated $H_1 \to \gamma\gamma$; VBF, $H_1 \to \tau\tau$ and ttH, $H_1 \to b\bar{b}$ modes is possible in that region (Fig.64). The outermost discovery contour of $H_1 \to \gamma\gamma$ follows approximately the 60% line of the branching ratio of $H_1 \to A_1 A_1$. The H_2 has contributions from the channels $H_2 \to \gamma\gamma$; VBF, $H_2 \to WW$; GGF, $H_2 \to ZZ \to 4l$ and GGF, $H_2 \to WW \to 2l2\nu$ in the excluded region where it is light enough to be accessible (Fig.65). All other Higgs bosons have either highly reduced couplings or are too heavy to be observed in this scenario.

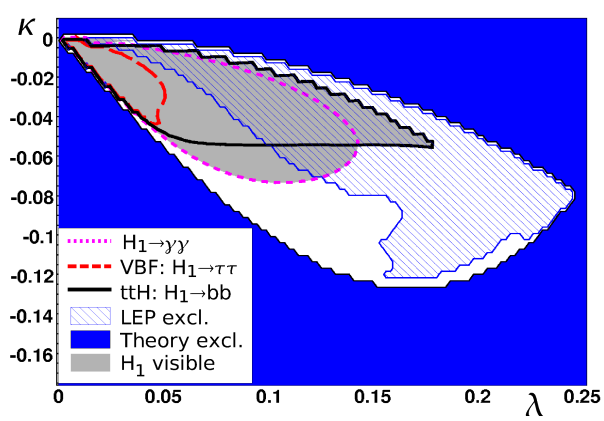

Fig. 64: 5σ discovery contours of the H_1 in the λ-κ plane for the *Light A_1 Scenario*, restricted to low λ and κ values.

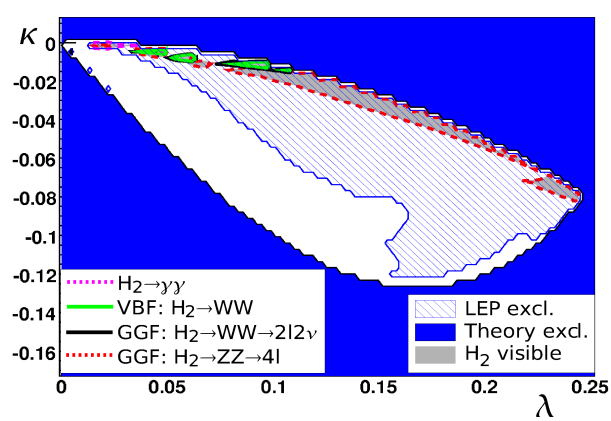

Fig. 65: 5σ discovery contours of H_2 in the λ-κ plane for the *Light A_1 Scenario*, restricted to low λ and κ values.

20.6 Conclusions

An evaluation of the ATLAS discovery potential for NMSSM Higgs bosons within two benchmark scenarios was performed. At least one Higgs boson was found to be observable in regions without a light A_1 or where the branching ratio of $H_{1/2}\rightarrow A_1 A_1$ is smaller than about 60%. In the other cases, searches for the decay chains $H_{1/2}\rightarrow A_1 A_1 \rightarrow \tau\tau b\bar{b}$ or $H_{1/2}\rightarrow A_1 A_1 \rightarrow 4\tau$ could be considered.

Acknowledements

We would like to thank U. Ellwanger, E. Gross, S. Heinemeyer, T. Plehn and M. Spira for helpful discussions. The authors thank U. Ellwanger, E. Gross, S. Heinemeyer, T. Plehn and M. Spira for helpful discussions.

21. THE $h^0 \rightarrow A^0 A^0 \rightarrow b\bar{b}\tau^+\tau^-$ SIGNAL IN VECTOR BOSON FUSION PRODUCTION AT THE LHC [39]

21.1 Motivation

In the Minimal Supersymmetric extension of the Standard Model (MSSM) at least one additional $SU(2)_L$ Higgs doublet is required compared to the SM in order to cancel gauge anomalies of the superpartners and to allow Yukawa couplings for all fermions. In order to address the fine-tuning "μ-problem" that appears in the MSSM, one can also add an extra complex singlet to these doublets. This last possibility, known in the literature as the Next-to-Minimal Supersymmetric Standard Model (NMSSM), has an interesting phenomenology (e.g. see [323]).

In the NMSSM, one of the pseudoscalar states (A^0) is the Goldstone boson of either a global $U(1)$ R-symmetry or a $U(1)$ Peccei-Quinn symmetry in some limit of the model parameters. Since low-fine tuning scenarios predict a moderate breaking of these symmetries, the mass of A^0 is expected to be relatively small compared to the mass of the lightest scalar (h^0) such that the $h^0 \rightarrow A^0 A^0$ decay is kinematically allowed. In [324], two different types of scenarios are considered, depending on if $m_{A^0} > 2m_b$ or $m_{A^0} < 2m_b$. Scenarios with $m_{A^0} > 2m_b$ are disfavored when LEP data for $Z2b$ and $Z4b$ final states are taken into account. Indeed, the simultaneous analysis of both these channels excludes at better than 99% the possibility for h^0 to be lighter than ~ 108 GeV, and a heavier h^0 in turn requires a higher fine-tuning of model parameters. On the contrary, scenarios with $m_{A^0} < 2m_b$ are favored by the same data and can even account for the 2σ excess observed in the $Z2b$ final state in the $m_{h^0} \sim 100$ GeV vicinity. As a consequence, many NMSSM related analyses focus on the $h^0 \rightarrow A^0 A^0 \rightarrow \tau^+\tau^-\tau^+\tau^-$ decay which has the most favorable branching ratio if $m_{A^0} < 2m_b$.

Nevertheless, besides the particular context of the NMSSM, many other possibilities remain open. If the MSSM scalar sector violates the CP symmetry, standard mass relations do not hold anymore and the decay of h^0 into two lighter Higgs bosons may be allowed [325]. In [326], a light A^0 (i.e., between 0.1 and a few tens of GeV) decays predominantly into pairs of photons (or gluons) thanks to a vector-like quark loop. Another possibility arises in the context of the generic two-Higgs-doublet model (2HDM). As shown in [327], a moderately light A^0 (i.e., between 10 and 100 GeV) can *naturally* satisfy the ρ parameter constraints thanks to a twisted realization of the custodial (or equivalently CP) symmetry. As emphasized in [328], a pseudoscalar in this mass range together with a moderate value of $\tan\beta$ can also account (in type II 2HDMs) for the observed discrepancy between the experimental measurement of the muon anomalous magnetic moment and the SM predictions.

Assuming $m_{A^0} > 2m_b$, and that the coupling of A^0 to fermions is proportional to the mass for down-type quarks and leptons (the up-type quark couplings being negligible for $\tan\beta \gg 1$), the main decay modes are $A^0 \rightarrow b\bar{b}$ (BR $\sim$ 0.92) and $A^0 \rightarrow \tau^+\tau^-$ (BR $\sim$ 0.08). Under the hypothesis that BR($h^0 \rightarrow A^0 A^0$)~ 1 (which is a reasonable approximation in many models), this gives a total branching

[39] Contributed by: N. E. Adam, V. Halyo, M. Herquet, and S. Gleyzer

ratio of ~ 0.85 for $h^0 \to A^0A^0 \to 4b$, ~ 0.15 for $h^0 \to A^0A^0 \to 2b2\tau$ and less than one percent for $h^0 \to A^0A^0 \to 4\tau$. Since the four τ final state signal is suppressed at least by a factor of a hundred compared to the $m_{A^0} < 2m_b$ scenario studied in Section19., the LHC discovery of h^0 and A^0 in this channel is probably difficult. On the other hand, the four b final state has a large BR, but suffers from important QCD backgrounds. This final state has been investigated in direct production mode at the Tevatron (where it is overwhelmed by the backgrounds [329]) and in W/Z associated production [307]. At the LHC, a discovery significance may still be reached in this last mode [307, 330].

In the current work, we focus on the intermediate $2b2\tau$ final state, which has a smaller but still sizable BR than the $4b$ final state, together with a much lower background. This final state has been considered in the framework of the associated production of h^0 with a W/Z boson at the Tevatron in [100, 307]. However, in this case, only a few events could be observed after a few fb^{-1} due to the cuts and b/τ tagging necessary to remove the large reducible background. Similar difficulties with the reducible background are also expected at LHC [307]. In the present study, we concentrate on the Vector Boson Fusion (VBF) production mode for h^0, which has been shown to be a promising channel at the LHC for the SM decay $h^0 \to \tau^+\tau^-$ both in parton-level analysis [113, 331] and after full detector simulation [108, 332, 333]. After the end of the redaction of this work, it has been brought to our knowledge that a study on similar lines in the context of the NMSSM, using parton shower based simulations, can be found in [293, 304].

21.2 Signal and Background

The signal and background Monte-Carlo simulation has been carried out at tree level using MADGRAPH/MADEVENT V4 [153] for the parton-level event generation.

In the framework of this preliminary analysis, some simplifying assumptions are made. The SM-like Higgs, h^0, shares all SM Higgs boson couplings plus an additional coupling to the pseudoscalar A^0 large enough to ensure BR($h^0 \to A^0A^0$) ~ 1. Its mass is fixed at 120 GeV, i.e. this is above the best LEP limit to avoid *de facto* all possible direct constraints, but is still light enough to ensure a sizable production cross-section. The light pseudoscalar mass is fixed at 50 GeV in order to lie below the $m_{h^0}/2$ threshold, while still being large enough to guarantee a good angular separation of decay products.

As mentioned in the previous section, the coupling of A^0 to fermions is assumed to be proportional to their mass for down-type quarks and charged leptons, giving a total branching ratio for $h^0 \to A^0A^0 \to 2b2\tau$ of about 0.15, which may be compared with the SM expectation BR($h^0 \to \tau^+\tau^-$) of ~ 0.08. This is only true if the coupling to up-type quarks is strongly suppressed, for example, due to an additional $\tan\beta$ factor in a type II 2HDM. If this is not the case, the considered total branching ratio can be reduced by up to a factor two.

In order to improve signal to background separation, few kinematical cuts such as minimum p_T of 10 GeV for all b-jets, 20 GeV for all non-b jets, and 10 GeV for all leptons have been applied. In addition, acceptance cuts such as the maximum pseudorapidity of 5 for jets, and of 2.5 for b-jets and leptons, and a minimal separation cut, i.e. $\Delta R > 0.3$, on all objects pairs have been applied at the parton level. Furthermore, to narrow ourselves to the particular kinematic configuration of signal events, standard VBF cuts are applied, i.e. $|\Delta\eta| > 4$ and $m_{jj} > 700$ GeV for the two forward jets. Finally, a maximum invariant mass cut, $m_{\tau\tau} < 80$ GeV, is imposed on all leptons pairs to avoid the Z peak in some backgrounds.

The signal is characterized by a final state populated with two central b jets, two central τ's and two forward jets. To avoid triggering issues, we focus on final states in which both τ's decay leptonically. The associated tree level cross-section (after τ decays and cuts) is 9.5 fb. The irreducible background, where the τ pair is coming from an off-shell photon or Z, and the b pair from a gluon splitting, is rather low, with a 1 fb cross-section. The same process with an e or μ pair replacing the τ pair has a more sizable cross section of around 8.7 fb, due to the absence of the τ branching ratio suppression. The most

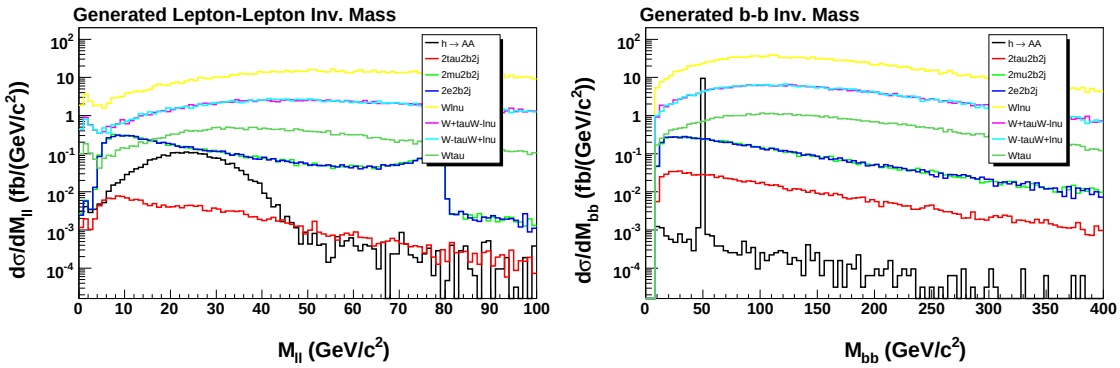

Fig. 66: Invariant mass of the final-state (oppositely charged) di-lepton pairs and di-bottom quarks before the final kinematical cuts 39. Each signal or background contribution is normalized by cross-section.

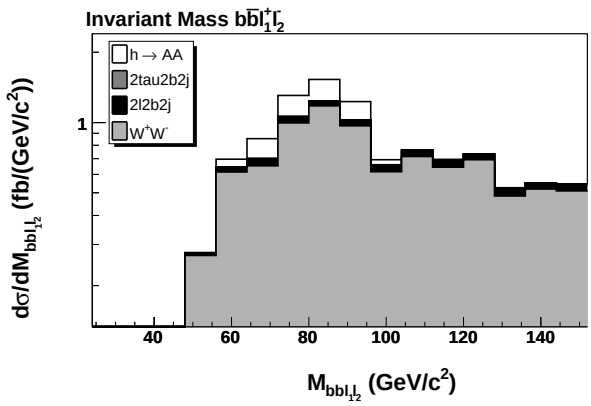

Fig. 67: Invariant mass M_{bbll} of the four-body final state. The signal and background histograms are stacked and normalized by their corresponding cross-sections.

dangerous background is $t\bar{t}$ + 2jets with fully leptonic top decays (through an intermediate τ or not). However, even though the total cross-section is almost three orders of magnitude larger than the signal (3.2 pb), the associated kinematics, and in particular the invariant mass distribution of b's and leptons, are very different.

21.3 Results

Figure 66 shows the invariant mass combination of any oppositely charged di-lepton pairs and any bottom quark pairs. Only the cuts described in the previous section have been applied.

Looking at the kinematic distributions of the signal and background samples (described in the previous section), it is evident that a cut based technique can be defined to achieve separation. The chosen selection criteria are:

$$M_{ll} \leq 30, \qquad 40 \leq M_{bb} \leq 60, \qquad \Delta R_{ll} \leq 2, \quad \text{and} \quad \Delta R_{bb} \leq 2. \tag{39}$$

Figure 67 shows the invariant mass M_{bbll}, of the four body final state after these simple cuts. The signal and the background considered are stacked and normalized by cross-section. A simple estimate of the significance around M_{bbll}, in the region $50 \leq M_{bbll} \leq 110$, yields $S/\sqrt{B} = 4$ for an integrated luminosity of 100 fb^{-1}, with approximatively 100 signal events. B-tagging efficiency will impact the

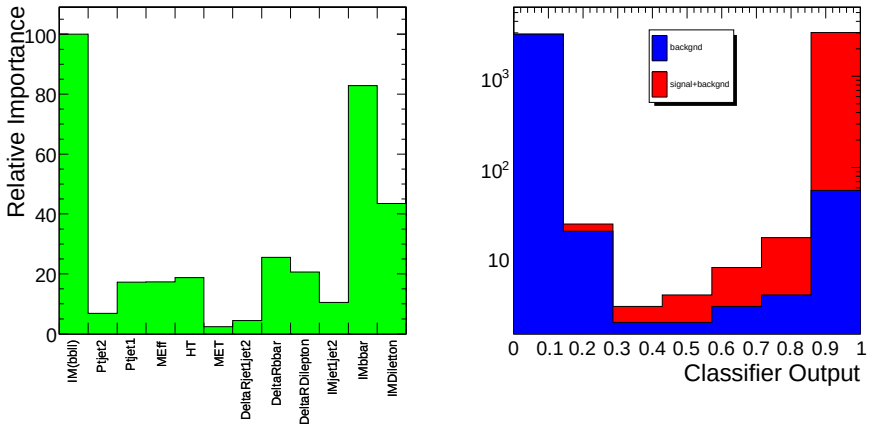

(a) (b)

Fig. 68: a) Relative importance of the various kinematic variables, as determined using the *PARADIGM* algorithm. b) The decision tree classifier output.

number of both signal and background events, and reduces this significance by a factor of ~ 2 if a b-tagging efficiency of 50% is assumed. Of course this simple generator-level estimate is merely a crude check on the feasibility of studying $h^0 \to A^0 A^0 \to b\bar{b}\tau^+\tau^-$ in VBF.

Since after reconstruction we expect the significance to decrease even further, this parton-level result motivates the use of a statistics-based multivariate approach in order to further discriminate between signal and background. Preliminary results demonstrating the discriminating power of the technique between the signal, the irreducible background and part of the $t\bar{t} + 2j$ background are shown in Figure 68.

Figure 68 (a) shows the relative contribution of the various input variables to signal and background separation. A framework for parameter space optimization, PARADIGM, is utilized for the above task [334]. The two most effective variables for signal/background separation in this decay mode are the invariant mass of the b-jets and leptons M_{bbll} and the invariant mass of the b-jets M_{bb}, as was also observed in the cut based study. Although PARADIGM allows the reduction of parameter space, we do not eliminate any of the variables since the dimensionality of the initial feature space considered is lower than the degrees of freedom of the model. Therefore, it is likely that the classifier performance can be further enhanced by the addition of more variables.

The decision tree classifier output is shown in Figure 68 (b). The measure of discrepancy between the background-only hypothesis and the background plus signal hypothesis (assuming a normal error distribution and using the classifier itself as the test statistic in a two-tailed test [335]) is found to be 0.0086 ± 0.0058 at 95% CL. This is a statistically significant result.

21.4 Conclusions

We showed that the $h^0 \to A^0 A^0 \to b\bar{b}\tau^+\tau^-$ signal in VBF production at the LHC is potentially feasible with an integrated luminosity of 100 fb^{-1}. Using a simple cut based technique, we found approximately 25 signal events and a significance of $\sim$2 for this luminosity (taking into account a 50% b-tagging efficiency) . This result motivates the use other techniques, such as a multivariate analysis, to further enhance the feasibility of this search at the LHC. A more robust multivariate analysis that includes different mass hypotheses, a full set of reducible backgrounds as well as fast detector simulation and evaluation of systematic uncertainties is envisaged by the authors.

Acknowledgments

We thank the organizers and conveners of the Les Houches workshop where this work originated. We also thank Fabio Maltoni and Simon de Visscher for useful discussion. The work of M.H. was supported by the Institute Interuniversitaire des Sciences Nucléaires and by the Belgian Federal Office for Scientific, Technical and Cultural Affairs through the Interuniversity Attraction Pole P6/11. This work was also supported in part by USDOE grant DE-FG02-91ER40671

References

[1] P. W. Higgs, *Phys. Rev. Lett.* **13** (1964) 508–509.

[2] A. Djouadi, *Phys. Rept.* **457** (2008) 1–216, [hep-ph/0503172].

[3] M. S. Carena and H. E. Haber, *Prog. Part. Nucl. Phys.* **50** (2003) 63–152, [hep-ph/0208209].

[4] R. Barate *et. al.*,, **LEP** Collaboration *Phys. Lett.* **B565** (2003) 61–75, [hep-ex/0306033].

[5] J. Alcaraz *et. al.*,, **LEP** Collaboration arXiv:0712.0929 [hep-ex].

[6] L. E. W. group, */lepewwg.web.cern.ch/LEPEWWG*.

[7] **TEVNPH Working Group** Collaboration arXiv:0712.2383 [hep-ex].

[8] M. Duhrssen *et. al.*, *Phys. Rev.* **D70** (2004) 113009, [hep-ph/0406323].

[9] S. Dawson, *Nucl. Phys.* **B359** (1991) 283–300.

[10] A. Djouadi, M. Spira, and P. M. Zerwas, *Phys. Lett.* **B264** (1991) 440–446.

[11] M. Spira, A. Djouadi, D. Graudenz, and P. M. Zerwas, *Nucl. Phys.* **B453** (1995) 17–82, [hep-ph/9504378].

[12] R. V. Harlander, *Phys. Lett.* **B492** (2000) 74–80, [hep-ph/0007289].

[13] S. Catani, D. de Florian, and M. Grazzini, *JHEP* **05** (2001) 025, [hep-ph/0102227].

[14] R. V. Harlander and W. B. Kilgore, *Phys. Rev.* **D64** (2001) 013015, [hep-ph/0102241].

[15] R. V. Harlander and W. B. Kilgore, *Phys. Rev. Lett.* **88** (2002) 201801, [hep-ph/0201206].

[16] C. Anastasiou and K. Melnikov, *Nucl. Phys.* **B646** (2002) 220–256, [hep-ph/0207004].

[17] V. Ravindran, J. Smith, and W. L. van Neerven, *Nucl. Phys.* **B665** (2003) 325–366, [hep-ph/0302135].

[18] S. Catani, D. de Florian, M. Grazzini, and P. Nason, *JHEP* **07** (2003) 028, [hep-ph/0306211].

[19] S. Moch and A. Vogt, *Phys. Lett.* **B631** (2005) 48–57, [hep-ph/0508265].

[20] E. Laenen and L. Magnea, *Phys. Lett.* **B632** (2006) 270–276, [hep-ph/0508284].

[21] A. Idilbi, X.-d. Ji, J.-P. Ma, and F. Yuan, *Phys. Rev.* **D73** (2006) 077501, [hep-ph/0509294].

[22] A. Djouadi and P. Gambino, *Phys. Rev. Lett.* **73** (1994) 2528–2531, [hep-ph/9406432].

[23] U. Aglietti, R. Bonciani, G. Degrassi, and A. Vicini, *Phys. Lett.* **B595** (2004) 432–441, [hep-ph/0404071].

[24] G. Degrassi and F. Maltoni, *Phys. Lett.* **B600** (2004) 255–260, [hep-ph/0407249].

[25] R. V. Harlander and M. Steinhauser, *JHEP* **09** (2004) 066, [hep-ph/0409010].

[26] R. V. Harlander and M. Steinhauser, *Phys. Lett.* **B574** (2003).

[27] R. Harlander and M. Steinhauser, *Phys. Rev.* **D68** (2003) 111701, [hep-ph/0308210].

[28] M. Muhlleitner and M. Spira, *Nucl. Phys.* **B790** (2008) 1–27, [hep-ph/0612254].

[29] R. Bonciani, G. Degrassi, and A. Vicini, *JHEP* **11** (2007) 095, [arXiv:0709.4227 [hep-ph]].

[30] C. Anastasiou, S. Beerli, S. Bucherer, A. Daleo, and Z. Kunszt, *JHEP* **01** (2007) 082, [hep-ph/0611236].

[31] D. de Florian, M. Grazzini, and Z. Kunszt, *Phys. Rev. Lett.* **82** (1999) 5209–5212, [hep-ph/9902483].

[32] J. M. Campbell, R. K. Ellis, and G. Zanderighi, *JHEP* **10** (2006) 028, [hep-ph/0608194].

[33] O. Brein and W. Hollik, *Phys. Rev.* **D68** (2003) 095006, [hep-ph/0305321].

[34] B. Field, S. Dawson, and J. Smith, *Phys. Rev.* **D69** (2004) 074013, [hep-ph/0311199].

[35] S. Catani, D. de Florian, and M. Grazzini, *JHEP* **01** (2002) 015, [hep-ph/0111164].

[36] C. Anastasiou, K. Melnikov, and F. Petriello, *Nucl. Phys.* **B724** (2005) 197–246, [hep-ph/0501130].

[37] C. Anastasiou, G. Dissertori, and F. Stockli, *JHEP* **09** (2007) 018, [arXiv:0707.2373 [hep-ph]].

[38] S. Catani and M. Grazzini, *Phys. Rev. Lett.* **98** (2007) 222002, [hep-ph/0703012].

[39] M. Grazzini, arXiv:0801.3232 [hep-ph].

[40] U. Langenegger, M. Spira, A. Starodumov, and P. Trueb, *JHEP* **06** (2006) 035, [hep-ph/0604156].

[41] C. Balazs and C. P. Yuan, *Phys. Lett.* **B478** (2000) 192–198, [hep-ph/0001103].

[42] E. L. Berger and J.-w. Qiu, *Phys. Rev.* **D67** (2003) 034026, [hep-ph/0210135].

[43] A. Kulesza, G. Sterman, and W. Vogelsang, *Phys. Rev.* **D69** (2004) 014012, [hep-ph/0309264].

[44] G. Bozzi, S. Catani, D. de Florian, and M. Grazzini, *Phys. Lett.* **B564** (2003) 65–72, [hep-ph/0302104].

[45] G. Bozzi, S. Catani, D. de Florian, and M. Grazzini, *Nucl. Phys.* **B737** (2006) 73–120, [hep-ph/0508068].

[46] G. Bozzi, S. Catani, D. de Florian, and M. Grazzini, *Nucl. Phys.* **B791** (2008) 1–19, [arXiv:0705.3887 [hep-ph]].

[47] V. Ravindran, J. Smith, and W. L. Van Neerven, *Nucl. Phys.* **B634** (2002) 247–290, [hep-ph/0201114].

[48] C. J. Glosser and C. R. Schmidt, *JHEP* **12** (2002) 016, [hep-ph/0209248].

[49] C. Balazs, M. Grazzini, J. Huston, A. Kulesza, and I. Puljak, hep-ph/0403052.

[50] A. Djouadi, M. Spira, J. J. van der Bij, and P. M. Zerwas, *Phys. Lett.* **B257** (1991) 187–190.

[51] G. Degrassi and F. Maltoni, *Nucl. Phys.* **B724** (2005) 183–196, [hep-ph/0504137].

[52] G. Passarino, C. Sturm, and S. Uccirati, *Phys. Lett.* **B655** (2007) 298–306, [arXiv:0707.1401 [hep-ph]].

[53] M. Steinhauser, hep-ph/9612395.

[54] T. Binoth, J. P. Guillet, E. Pilon, and M. Werlen, *Eur. Phys. J.* **C16** (2000) 311–330, [hep-ph/9911340].

[55] Z. Bern, L. J. Dixon, and C. Schmidt, *Phys. Rev.* **D66** (2002) 074018, [hep-ph/0206194].

[56] M. Dittmar and H. K. Dreiner, *Phys. Rev.* **D55** (1997) 167–172, [hep-ph/9608317].

[57] C. Anastasiou, G. Dissertori, F. Stoeckli, and B. R. Webber, arXiv:0801.2682 [hep-ph].

[58] G. Davatz, G. Dissertori, M. Dittmar, M. Grazzini, and F. Pauss, *JHEP* **05** (2004) 009, [hep-ph/0402218].

[59] L. J. Dixon, Z. Kunszt, and A. Signer, *Phys. Rev.* **D60** (1999) 114037, [hep-ph/9907305].

[60] J. M. Campbell and R. K. Ellis, *Phys. Rev.* **D60** (1999) 113006, [hep-ph/9905386].

[61] M. Grazzini, *JHEP* **01** (2006) 095, [hep-ph/0510337].

[62] S. Frixione and B. R. Webber, *JHEP* **06** (2002) 029, [hep-ph/0204244].

[63] S. Frixione, P. Nason, and B. R. Webber, *JHEP* **08** (2003) 007, [hep-ph/0305252].

[64] T. Binoth, M. Ciccolini, N. Kauer, and M. Kramer, *JHEP* **03** (2005) 065, [hep-ph/0503094].

[65] M. Duhrssen, K. Jakobs, J. J. van der Bij, and P. Marquard, *JHEP* **05** (2005) 064, [hep-ph/0504006].

[66] W. Bernreuther, A. Brandenburg, Z. G. Si, and P. Uwer, *Phys. Rev. Lett.* **87** (2001) 242002, [hep-ph/0107086].

[67] N. Kauer and D. Zeppenfeld, *Phys. Rev.* **D65** (2002) 014021, [hep-ph/0107181].

[68] R. Frederix and M. Grazzini, arXiv:0801.2229 [hep-ph].

[69] A. Bredenstein, A. Denner, S. Dittmaier, and M. M. Weber, *Phys. Rev.* **D74** (2006) 013004, [hep-ph/0604011].

[70] A. Bredenstein, A. Denner, S. Dittmaier, and M. M. Weber, *JHEP* **02** (2007) 080, [hep-ph/0611234].

[71] T. Han, G. Valencia, and S. Willenbrock, *Phys. Rev. Lett.* **69** (1992) 3274–3277, [hep-ph/9206246].

[72] T. Figy, C. Oleari, and D. Zeppenfeld, *Phys. Rev.* **D68** (2003) 073005, [hep-ph/0306109].

[73] T. Figy and D. Zeppenfeld, *Phys. Lett.* **B591** (2004) 297–303, [hep-ph/0403297].

[74] E. L. Berger and J. Campbell, *Phys. Rev.* **D70** (2004) 073011, [hep-ph/0403194].

[75] M. Ciccolini, A. Denner, and S. Dittmaier, *Phys. Rev. Lett.* **99** (2007) 161803, [arXiv:0707.0381 [hep-ph]].

[76] M. Ciccolini, A. Denner, and S. Dittmaier, *Phys. Rev.* **D77** (2008) 013002, [arXiv:0710.4749 [hep-ph]].

[77] V. Del Duca, W. Kilgore, C. Oleari, C. Schmidt, and D. Zeppenfeld, *Nucl. Phys.* **B616** (2001) 367–399, [hep-ph/0108030].

[78] V. Del Duca *et. al.*, *JHEP* **10** (2006) 016, [hep-ph/0608158].

[79] J. Campbell and R. K. Ellis, *Phys. Rev.* **D65** (2002) 113007, [hep-ph/0202176].

[80] C. Oleari and D. Zeppenfeld, *Phys. Rev.* **D69** (2004) 093004, [hep-ph/0310156].

[81] B. Jager, C. Oleari, and D. Zeppenfeld, *JHEP* **07** (2006) 015, [hep-ph/0603177].

[82] S. Dittmaier, P. Uwer, and S. Weinzierl, *Phys. Rev. Lett.* **98** (2007) 262002, [hep-ph/0703120].

[83] S. Dittmaier, M. Kramer, and M. Spira, *Phys. Rev.* **D70** (2004) 074010, [hep-ph/0309204].

[84] S. Dawson, C. B. Jackson, L. Reina, and D. Wackeroth, *Phys. Rev.* **D69** (2004) 074027, [hep-ph/0311067].

[85] S. Dawson, C. B. Jackson, L. Reina, and D. Wackeroth, *Phys. Rev. Lett.* **94** (2005) 031802, [hep-ph/0408077].

[86] S. Dawson, C. B. Jackson, L. Reina, and D. Wackeroth, *Mod. Phys. Lett.* **A21** (2006) 89–110, [hep-ph/0508293].

[87] R. V. Harlander and W. B. Kilgore, *Phys. Rev.* **D68** (2003) 013001, [hep-ph/0304035].

[88] J. Campbell, R. K. Ellis, F. Maltoni, and S. Willenbrock, *Phys. Rev.* **D67** (2003) 095002, [hep-ph/0204093].

[89] J. Campbell *et. al.*, hep-ph/0405302.

[90] C. Buttar *et. al.*, hep-ph/0604120.

[91] S. Dittmaier, M. Kramer, A. Muck, and T. Schluter, *JHEP* **03** (2007) 114, [hep-ph/0611353].

[92] F. Boudjema and L. D. Ninh, arXiv:0711.2005 [hep-ph].

[93] S. Dawson and C. B. Jackson, *Phys. Rev.* **D77** (2008) 015019, [arXiv:0709.4519 [hep-ph]].

[94] W. Beenakker *et. al.*, *Phys. Rev. Lett.* **87** (2001) 201805, [hep-ph/0107081].

[95] W. Beenakker *et. al.*, *Nucl. Phys.* **B653** (2003) 151–203, [hep-ph/0211352].

[96] S. Dawson, L. H. Orr, L. Reina, and D. Wackeroth, *Phys. Rev.* **D67** (2003) 071503, [hep-ph/0211438].

[97] S. Dawson, C. Jackson, L. H. Orr, L. Reina, and D. Wackeroth, *Phys. Rev.* **D68** (2003) 034022, [hep-ph/0305087].

[98] *CMS Physics, Technical Design Report, Vol. II Physics Performance* [report CERN/LHCC 2006-021].

[99] A. Belyaev and L. Reina, *JHEP* **08** (2002) 041, [hep-ph/0205270].

[100] U. Aglietti *et. al.*, hep-ph/0612172.

[101] T. Han and S. Willenbrock, *Phys. Lett.* **B273** (1991) 167–172.

[102] R. Hamberg, W. L. van Neerven, and T. Matsuura, *Nucl. Phys.* **B359** (1991) 343–405.

[103] O. Brein, A. Djouadi, and R. Harlander, *Phys. Lett.* **B579** (2004) 149–156, [hep-ph/0307206].

[104] M. L. Ciccolini, S. Dittmaier, and M. Kramer, *Phys. Rev.* **D68** (2003) 073003, [hep-ph/0306234].

[105] http://theory.fi.infn.it/grazzini/codes.html.

[106] A. D. Martin, R. G. Roberts, W. J. Stirling, and R. S. Thorne, *Phys. Lett.* **B604** (2004) 61–68, [hep-ph/0410230].

[107] S. Catani and B. R. Webber, *JHEP* **10** (1997) 005, [hep-ph/9710333].

[108] S. Asai *et. al.*, *Eur. Phys. J.* **C32S2** (2004) 19–54.

[109] S. Abdullin *et. al.*, *Eur. Phys. J.* **C39S2** (2005) 41–61.

[110] V. Hankele, G. Klamke, D. Zeppenfeld, and T. Figy, *Phys. Rev.* **D74** (2006) 095001, [hep-ph/0609075].

[111] V. D. Barger, R. J. N. Phillips, and D. Zeppenfeld, *Phys. Lett.* **B346** (1995) 106–114, [hep-ph/9412276].

[112] D. L. Rainwater and D. Zeppenfeld, *JHEP* **12** (1997) 005, [hep-ph/9712271].

[113] D. L. Rainwater, D. Zeppenfeld, and K. Hagiwara, *Phys. Rev.* **D59** (1999) 014037, [hep-ph/9808468].

[114] D. L. Rainwater and D. Zeppenfeld, *Phys. Rev.* **D60** (1999) 113004, [hep-ph/9906218].

[115] M. Spira, *Fortsch. Phys.* **46** (1998) 203–284, [hep-ph/9705337].

[116] M. Bähr *et. al.*, http://www-itp.particle.uni-karlsruhe.de/~vbfnloweb/.

[117] M. Spira, http://people.web.psi.ch/spira/vv2h.

[118] S. Eidelman *et. al.*,, **Particle Data Group** Collaboration *Phys. Lett.* **B592** (2004) 1.

[119] A. Denner, S. Dittmaier, M. Roth, and L. H. Wieders, *Nucl. Phys.* **B724** (2005) 247–294, [hep-ph/0505042].

[120] D. Y. Bardin, A. Leike, T. Riemann, and M. Sachwitz, *Phys. Lett.* **B206** (1988) 539–542.

[121] F. Jegerlehner, hep-ph/0105283.

[122] J. Pumplin *et. al.*, *JHEP* **07** (2002) 012, [hep-ph/0201195].

[123] S. Catani, Y. L. Dokshitzer, and B. R. Webber, *Phys. Lett.* **B285** (1992) 291–299.

[124] G. C. Blazey *et. al.*, hep-ex/0005012.

[125] R. N. Cahn and S. Dawson, *Phys. Lett.* **B136** (1984) 196.

[126] D. A. Dicus and S. S. D. Willenbrock, *Phys. Rev.* **D32** (1985) 1642.

[127] G. Altarelli, B. Mele, and F. Pitolli, *Nucl. Phys.* **B287** (1987) 205–224.

[128] T. Plehn, D. L. Rainwater, and D. Zeppenfeld, *Phys. Rev. Lett.* **88** (2002) 051801, [hep-ph/0105325].

[129] E. L. Berger and J. Campbell, *Phys. Rev.* **D70** (2004) 073011, [hep-ph/0403194].

[130] V. Del Duca, A. Frizzo, and F. Maltoni, *JHEP* **05** (2004) 064, [hep-ph/0404013].

[131] F. Wilczek, *Phys. Rev. Lett.* **39** (1977) 1304.

[132] J. R. Andersen and J. M. Smillie, *Phys. Rev.* **D75** (2007) 037301, [hep-ph/0611281].

[133] J. R. Andersen, T. Binoth, G. Heinrich, and J. M. Smillie, arXiv:0709.3513 [hep-ph].

[134] T. Binoth, J. P. Guillet, and G. Heinrich, *Nucl. Phys.* **B572** (2000) 361–386, [hep-ph/9911342].

[135] T. Binoth, J. P. Guillet, G. Heinrich, E. Pilon, and C. Schubert, *JHEP* **10** (2005) 015, [hep-ph/0504267].

[136] T. Binoth, M. Ciccolini, N. Kauer, and M. Kramer, *JHEP* **12** (2006) 046, [hep-ph/0611170].

[137] T. Binoth, S. Karg, N. Kauer, and R. Ruckl, *Phys. Rev.* **D74** (2006) 113008, [hep-ph/0608057].

[138] T. Binoth, J. P. Guillet, and F. Mahmoudi, *JHEP* **02** (2004) 057, [hep-ph/0312334].

[139] L. J. Dixon and Y. Sofianatos,. in preparation.

[140] W. T. Giele and E. W. N. Glover, *Phys. Rev.* **D46** (1992) 1980–2010.

[141] W. T. Giele, E. W. N. Glover, and D. A. Kosower, *Nucl. Phys.* **B403** (1993) 633–670, [hep-ph/9302225].

[142] W.-M. Yao *et. al.*, *Journal of Physics G* **33** (2006).

[143] J. R. Forshaw and M. Sjodahl, *JHEP* **09** (2007) 119, [arXiv:0705.1504 [hep-ph]].

[144] J. R. Andersen and C. D. White, arXiv:0802.2858 [hep-ph].

[145] G. Klamke and D. Zeppenfeld, *JHEP* **04** (2007) 052, [hep-ph/0703202].

[146] V. D. Barger, R. J. N. Phillips, and D. Zeppenfeld,.

[147] V. S. Fadin, E. A. Kuraev, and L. N. Lipatov, *Phys. Lett.* **B60** (1975) 50–52.

[148] V. Del Duca, W. Kilgore, C. Oleari, C. R. Schmidt, and D. Zeppenfeld, *Phys. Rev.* **D67** (2003) 073003, [hep-ph/0301013].

[149] V. Del Duca, http://arXiv.org/abs/hep-ph/9503226.

[150] M. Ciafaloni, *Nucl. Phys.* **B296** (1988) 49.

[151] S. Catani, F. Fiorani, and G. Marchesini, *Phys. Lett.* **B234** (1990) 339.

[152] J. Kwiecinski, A. D. Martin, and P. J. Sutton, *Z. Phys.* **C71** (1996) 585–594, [hep-ph/9602320].

[153] J. Alwall *et. al.*, arXiv:0706.2334 [hep-ph].

[154] J. R. Andersen, *Phys. Lett.* **B639** (2006) 290–293, [hep-ph/0602182].

[155] J. M. Butterworth, J. P. Couchman, B. E. Cox, and B. M. Waugh, *Comput. Phys. Commun.* **153** (2003) 85–96, [hep-ph/0210022].

[156] V. Hankele, G. Klamke, and D. Zeppenfeld, hep-ph/0605117.

[157] B. Mele, P. Nason, and G. Ridolfi, *Nucl. Phys.* **B357** (1991) 409–438.

[158] J. Ohnemus, *Phys. Rev.* **D50** (1994) 1931–1945, [hep-ph/9403331].

[159] D. A. Dicus, C. Kao, and W. W. Repko, *Phys. Rev.* **D36** (1987) 1570.

[160] E. W. N. Glover and J. J. van der Bij, *Nucl. Phys.* **B321** (1989) 561.

[161] T. Matsuura and J. J. van der Bij, *Z. Phys.* **C51** (1991) 259–266.

[162] C. Zecher, T. Matsuura, and J. J. van der Bij, *Z. Phys.* **C64** (1994) 219–226, [hep-ph/9404295].

[163] T. Hahn and M. Perez-Victoria, *Comput. Phys. Commun.* **118** (1999) 153–165, [hep-ph/9807565].

[164] T. Hahn, *Comput. Phys. Commun.* **140** (2001) 418–431, [hep-ph/0012260].

[165] F. A. Berends, R. Pittau, and R. Kleiss, *Nucl. Phys.* **B424** (1994) 308–342, [hep-ph/9404313].

[166] N. Kauer, *Phys. Rev.* **D67** (2003) 054013, [hep-ph/0212091].

[167] L. J. Dixon, Z. Kunszt, and A. Signer, *Nucl. Phys.* **B531** (1998) 3–23, [hep-ph/9803250].

[168] http://hepsource.sf.net/programs/GG2ZZ/.

[169] E. Boos *et. al.*, hep-ph/0109068.

[170] J. Alwall *et. al.*, *Comput. Phys. Commun.* **176** (2007) 300–304, [hep-ph/0609017].

[171] D. Futyan, D. Fortin, and D. Giordano, *J. Phys.* **G34** (2007) N315–N342.

[172] T. Sjostrand, P. Eden, C. Friberg, L. Lonnblad, G. Miu, S. Mrenna, and E. Norrbin, *Computer Physics Communications* **135** (2001) 238.

[173] F. Maltoni and T. Stelzer, *JHEP* **02** (2003) 027, [hep-ph/0208156].

[174] P. Bartalini *et. al.*,. CERN-CMS-NOTE-2006-130.

[175] T. Plehn, D. L. Rainwater, and D. Zeppenfeld, *Phys. Rev.* **D61** (2000) 093005, [hep-ph/9911385].

[176] C. Foudas, A. Nikitenko, and M. Takahashi,. CERN-CMS-NOTE-2006-088.

[177] N. Ilina, V. Gavrilov, and A. Krokhotin,. CERN-CMS-INTERNAL NOTE-2004-040.

[178] G. Davatz, M. Dittmar, and A.-S. Giolo-Nicollerat,. CERN-CMS-NOTE-2006-047.

[179] Y. L. Dokshitzer, V. A. Khoze, and T. Sjostrand, *Phys. Lett.* **B274** (1992) 116–121.

[180] M. L. Mangano, M. Moretti, F. Piccinini, R. Pittau, and A. D. Polosa, *JHEP* **07** (2003) 001, [hep-ph/0206293].

[181] M. L. Mangano, M. Moretti, F. Piccinini, and M. Treccani, *JHEP* **01** (2007) 013, [hep-ph/0611129].

[182] S. Hoche *et. al.*, hep-ph/0602031.

[183] T. Sjostrand, S. Mrenna, and P. Skands, *JHEP* **05** (2006) 026, [hep-ph/0603175].

[184] D. Acosta *et. al.*,. CERN-CMS-NOTE-2006-067.

[185] K. A. Assamagan *et. al.*,, **Higgs Working Group** Collaboration hep-ph/0406152.

[186] M. L. Mangano, M. Moretti, F. Piccinini, R. Pittau, and A. D. Polosa, *Phys. Lett.* **B556** (2003) 50–60, [hep-ph/0210261].

[187] E. Gabrielli *et. al.*, *Nucl. Phys.* **B781** (2007) 64–84, [hep-ph/0702119].

[188] A. Djouadi, J. Kalinowski, and M. Spira, *Comput. Phys. Commun.* **108** (1998) 56–74, [hep-ph/9704448].

[189] H. L. Lai *et. al.*,, **CTEQ** Collaboration *Eur. Phys. J.* **C12** (2000) 375–392, [hep-ph/9903282].

[190] F. Abe *et. al.*,, **CDF** Collaboration *Phys. Rev.* **D56** (1997) 3811–3832.

[191] V. L. Korotkikh and A. M. Snigirev, *Phys. Lett.* **B594** (2004) 171–176, [hep-ph/0404155].

[192] E. Cattaruzza, A. Del Fabbro, and D. Treleani, *Phys. Rev.* **D72** (2005) 034022, [hep-ph/0507052].

[193] M. Spira, A. Djouadi, D. Graudenz, and P. M. Zerwas, *Phys. Lett.* **B318** (1993) 347–353.

[194] R. V. Harlander and W. B. Kilgore, *JHEP* **10** (2002) 017, [hep-ph/0208096].

[195] C. Anastasiou and K. Melnikov, *Phys. Rev.* **D67** (2003) 037501, [hep-ph/0208115].

[196] V. Ravindran, *Nucl. Phys.* **B746** (2006) 58–76, [hep-ph/0512249].

[197] V. Ravindran, *Nucl. Phys.* **B752** (2006) 173–196, [hep-ph/0603041].

[198] S. Dawson, A. Djouadi, and M. Spira, *Phys. Rev. Lett.* **77** (1996) 16–19, [hep-ph/9603423].

[199] R. V. Harlander and F. Hofmann, *JHEP* **03** (2006) 050, [hep-ph/0507041].

[200] M. S. Carena, S. Heinemeyer, C. E. M. Wagner, and G. Weiglein, *Eur. Phys. J.* **C26** (2003) 601–607, [hep-ph/0202167].

[201] A. Djouadi, hep-ph/0503173.

[202] J. R. Ellis, M. K. Gaillard, and D. V. Nanopoulos, *Nucl. Phys.* **B106** (1976) 292.

[203] M. A. Shifman, A. I. Vainshtein, M. B. Voloshin, and V. I. Zakharov, *Sov. J. Nucl. Phys.* **30** (1979) 711–716.

[204] B. Badelek *et. al.*,, **ECFA/DESY Photon Collider Working Group** Collaboration *Int. J. Mod. Phys.* **A19** (2004) 5097–5186, [hep-ex/0108012].

[205] M. M. Muhlleitner and P. M. Zerwas, *Acta Phys. Polon.* **B37** (2006) 1021–1038, [hep-ph/0511339].

[206] M. M. Muhlleitner, M. Kramer, M. Spira, and P. M. Zerwas, *Phys. Lett.* **B508** (2001) 311–316, [hep-ph/0101083].

[207] M. M. Muhlleitner, hep-ph/0008127.

[208] D. M. Asner, J. B. Gronberg, and J. F. Gunion, *Phys. Rev.* **D67** (2003) 035009, [hep-ph/0110320].

[209] P. Niezurawski, A. F. Zarnecki, and M. Krawczyk, hep-ph/0507006.

[210] M. Spira, P. Niezurawski, M. Krawczyk, and A. F. Zarnecki, *Pramana* **69** (2007) 931–936, [hep-ph/0612369].

[211] M. Kramer, E. Laenen, and M. Spira, *Nucl. Phys.* **B511** (1998) 523–549, [hep-ph/9611272].

[212] M. S. Carena, A. Menon, and C. E. M. Wagner, *Phys. Rev.* **D76** (2007) 035004, [arXiv:0704.1143 [hep-ph]].

[213] M. S. Carena, S. Mrenna, and C. E. M. Wagner, *Phys. Rev.* **D60** (1999) 075010, [hep-ph/9808312].

[214] D. Dicus, T. Stelzer, Z. Sullivan, and S. Willenbrock, *Phys. Rev.* **D59** (1999) 094016, [hep-ph/9811492].

[215] F. Maltoni, Z. Sullivan, and S. Willenbrock, *Phys. Rev.* **D67** (2003) 093005, [hep-ph/0301033].

[216] O. Brein and W. Hollik, *Phys. Rev.* **D76** (2007) 035002, [arXiv:0705.2744 [hep-ph]].

[217] M. S. Carena, D. Garcia, U. Nierste, and C. E. M. Wagner, *Nucl. Phys.* **B577** (2000) 88–120, [hep-ph/9912516].

[218] L. J. Hall, R. Rattazzi, and U. Sarid, *Phys. Rev.* **D50** (1994) 7048–7065, [hep-ph/9306309].

[219] J. Guasch, P. Hafliger, and M. Spira, *Phys. Rev.* **D68** (2003) 115001, [hep-ph/0305101].

[220] M. Carena, M. Olechowski, S. Pokorski, and C. E. M. Wagner, *Nucl. Phys.* **B426** (1994) 269–300, [hep-ph/9402253].

[221] H. E. Haber *et. al.*, *Phys. Rev.* **D63** (2001) 055004, [hep-ph/0007006].

[222] O. Brein and W. Hollik, arXiv:0710.4781 [hep-ph].

[223] H. P. Nilles, *Phys. Rept.* **110** (1984) 1.

[224] H. E. Haber and G. L. Kane, *Phys. Rept.* **117** (1985) 75.

[225] R. Barbieri, *Riv. Nuovo Cim.* **11N4** (1988) 1–45.

[226] **LEP Higgs Working Group for Higgs boson searches** Collaboration hep-ex/0107031.

[227] **LEP Higgs Working Group for Higgs boson searches** CollaborationP. Lutz, ,, 2007.

[228] **LEP Higgs Working Group for Higgs boson searches** Collaboration. in preparation.

[229] A. Abulencia *et. al.*,, **CDF** Collaboration *Phys. Rev. Lett.* **96** (2006) 042003, [hep-ex/0510065].

[230] ATLAS Collaboration,, **ATLAS** Collaboration. CERN-LHCC-99-14 and CERN-LHCC-99-15.

[231] M. S. Carena, S. Heinemeyer, C. E. M. Wagner, and G. Weiglein, *Eur. Phys. J.* **C45** (2006) 797–814, [hep-ph/0511023].

[232] J. A. Aguilar-Saavedra *et. al.*,, **ECFA/DESY LC Physics Working Group** Collaboration hep-ph/0106315.

[233] K. Ackermann *et. al.*,. prepared for 4th ECFA / DESY Workshop on Physics and Detectors for a 90-GeV to 800-GeV Linear e+ e- Collider, Amsterdam, The Netherlands, 1-4 Apr 2003. DESY-PROC-2004-01.

[234] T. Abe *et. al.*,, **American Linear Collider Working Group** Collaboration hep-ex/0106056.

[235] K. Abe *et. al.*,, **ACFA Linear Collider Working Group** Collaboration hep-ph/0109166.

[236] S. Heinemeyer *et. al.*, *ECONF* **C0508141** (2005) ALCPG0214, [hep-ph/0511332].

[237] M. Hashemi *et. al.*,. in preparation.

[238] M. Baarmand, M. Hashemi, and A. Nikitenko,. CMS Note 2006/056.

[239] T. Stelzer and W. F. Long, *Comput. Phys. Commun.* **81** (1994) 357–371, [hep-ph/9401258].

[240] R. Kinnunen,. CMS Note 2006/100.

[241] J. Alwall and J. Rathsman, *JHEP* **12** (2004) 050, [hep-ph/0409094].

[242] R. Hempfling, *Phys. Rev.* **D49** (1994) 6168–6172.

[243] S. Gennai *et. al.*, *Eur. Phys. J.* **C52** (2007) 383–395, [arXiv:0704.0619 [hep-ph]].

[244] T. Plehn, *Phys. Rev.* **D67** (2003) 014018, [hep-ph/0206121].

[245] E. L. Berger, T. Han, J. Jiang, and T. Plehn, *Phys. Rev.* **D71** (2005) 115012, [hep-ph/0312286].

[246] S. Heinemeyer, W. Hollik, and G. Weiglein, *Comput. Phys. Commun.* **124** (2000) 76–89, [hep-ph/9812320].

[247] S. Heinemeyer, W. Hollik, and G. Weiglein, *Eur. Phys. J.* **C9** (1999) 343–366, [hep-ph/9812472].

[248] G. Degrassi, S. Heinemeyer, W. Hollik, P. Slavich, and G. Weiglein, *Eur. Phys. J.* **C28** (2003) 133–143, [hep-ph/0212020].

[249] M. Frank *et. al.*, *JHEP* **02** (2007) 047, [hep-ph/0611326].

[250] J. Malmgren and K. Johansson, *Nucl. Inst. Methods A* **403** (1998) 481.

[251] T. Sjostrand, L. Lonnblad, S. Mrenna, and P. Skands, hep-ph/0308153.

[252] S. Jadach, J. H. Kuhn, and Z. Was, *Comput. Phys. Commun.* **64** (1990) 275–299.

[253] P. Golonka *et. al.*, *Comput. Phys. Commun.* **174** (2006) 818.

[254] J. S. Conway *et. al.*, in *Proceedings of the Workshop on Physics at Run II – Supersymmetry/Higgs*, p. 39, Fermilab, 1998. hep-ph/0010338.

[255] J. Alwall, C. Biscarat, S. Moretti, J. Rathsman, and A. Sopczak, *Eur. Phys. J.* **C39S1** (2005) 37–39, [hep-ph/0312301].

[256] V. M. Abazov *et. al.*, *DØ note 4879-CONF* (2005).

[257] K. A. Assamagan and Y. Coadou, *Acta Phys. Polon.* **B33** (2002) 707–720.

[258] S. Hesselbach, S. Moretti, J. Rathsman, and A. Sopczak, arXiv:0708.4394 [hep-ph].

[259] D. P. Roy, *Phys. Lett.* **B277** (1992) 183–189.

[260] S. Raychaudhuri and D. P. Roy, *Phys. Rev.* **D53** (1996) 4902–4908, [hep-ph/9507388].

[261] D. P. Roy, *Phys. Lett.* **B459** (1999) 607–614, [hep-ph/9905542].

[262] A. Beneke *et. al.*, *hep-ph/0003033* (2000).

[263] B. Mohn, M. Flechl, and J. Alwall,. ATL-PHYS-PUB-2007-006.

[264] C. Biscarat and M. Dosil, *ATL-PHYS-2003-038* (2003).

[265] S. Abdullin *et. al.*, *CMS Note 2003/033* (2003).

[266] K. A. Assamagan and N. Gollub, *SN-ATLAS-2004-042* (2004).

[267] R. Kinnunen, *CMS Note 2000/039* (2000).

[268] P. Salmi, R. Kinnunen, and N. Stepanov, *CMS Note 2002/024* (2002).

[269] S. Lowette, J. Heyninck, and P. Vanlaer, *CMS Note 2004/017* (2004).

[270] S. Schael *et. al.*,, **ALEPH** Collaboration *Eur. Phys. J.* **C47** (2006) 547–587, [hep-ex/0602042].

[271] D. K. Ghosh, R. M. Godbole, and D. P. Roy, *Phys. Lett.* **B628** (2005) 131–140, [hep-ph/0412193].

[272] J. S. Lee *et. al.*, *Comput. Phys. Commun.* **156** (2004) 283–317, [hep-ph/0307377].

[273] M. Beneke *et. al.*, hep-ph/0003033.

[274] M. Della Negra, L. Fo, A. Herve, and A. Petrilli,, *CMS physics Technical Design Report*. Technical Design Report CMS. CERN, Geneva, 2006.

[275] S. D. Ellis and D. E. Soper, *Phys. Rev.* **D48** (1993) 3160–3166, [hep-ph/9305266].

[276] S. Agostinelli *et. al.*,, **GEANT4** Collaboration *Nucl. Instrum. Meth.* **A506** (2003) 250–303.

[277] *CMS Physics Technical Design Report, volume-I* **CERN/LHCC/2006-001**.

[278] H.P. Nilles, M. Srednicki and D. Wyler, Phys. Lett. B **120** (1983) 346; J.M. Frere, D.R. Jones and S. Raby, Nucl. Phys. B **222** (1983) 11; J.R. Ellis, J.F. Gunion, H.E. Haber, L. Roszkowski and F. Zwirner, Phys. Rev. D **39** (1989) 844; M. Drees, Int. J. Mod. Phys. A **4** (1989) 3635; U. Ellwanger, M. Rausch de Traubenberg and C.A. Savoy, Phys. Lett. B **315** (1993) 331; S.F. King and P.L. White, Phys. Rev. D **52** (1995) 4183.

[279] For a recent review, see E. Accomando et al., arXiv:hep-ph/0608079.

[280] J. F. Gunion and C. Hugonie, JHEP **0507** (2005) 041 [arXiv:hep-ph/0503203].

[281] U. Ellwanger and C. Hugonie, Comput. Phys. Commun. **177** (2007) 399; http://www.th.u-psud.fr/NMHDECAY/nmssmtools.html.

[282] E. Boos, A. Djouadi and A. Nikitenko, Phys. Lett. B **578** (2004) 384 [arXiv:hep-ph/0307079].

[283] A. Djouadi *et. al.*, `arXiv:0801.4321 [hep-ph]`.

[284] A. Djouadi, arXiv:hep-ph/0503172 and arXiv:hep-ph/0503173, Phys. Repts. in press.

[285] I. Rottlander, M. Schumacher et al, to appear.

[286] S. Lehti, S. Nikitenko et al., to appear.

[287] H. P. Nilles, M. Srednicki, and D. Wyler, *Phys. Lett.* **B120** (1983) 346.

[288] J. M. Frere, D. R. T. Jones, and S. Raby, *Nucl. Phys.* **B222** (1983) 11.

[289] J. P. Derendinger and C. A. Savoy, *Nucl. Phys.* **B237** (1984) 307.

[290] J. R. Ellis, J. F. Gunion, H. E. Haber, L. Roszkowski, and F. Zwirner, *Phys. Rev.* **D39** (1989) 844.

[291] M. Drees, *Int. J. Mod. Phys.* **A4** (1989) 3635.

[292] F. Franke and H. Fraas, *Int. J. Mod. Phys.* **A12** (1997) 479–534, [`hep-ph/9512366`].

[293] U. Ellwanger, J. F. Gunion, C. Hugonie, and S. Moretti, `hep-ph/0401228`.

[294] D. J. Miller and S. Moretti, `hep-ph/0403137`.

[295] U. Ellwanger, J. F. Gunion, and C. Hugonie, *JHEP* **07** (2005) 041, [`hep-ph/0503203`].

[296] A. Djouadi *et. al.*,. These proceedings.

[297] U. Ellwanger and C. Hugonie, *Mod. Phys. Lett.* **A22** (2007) 1581–1590, [`hep-ph/0612133`].

[298] U. Ellwanger, J. F. Gunion, and C. Hugonie, *JHEP* **02** (2005) 066, [`hep-ph/0406215`].

[299] U. Ellwanger and C. Hugonie, *Comput. Phys. Commun.* **175** (2006) 290–303, [`hep-ph/0508022`].

[300] F. Domingo and U. Ellwanger, *JHEP* **12** (2007) 090, [`arXiv:0710.3714 [hep-ph]`].

[301] J. F. Gunion, H. E. Haber, and T. Moroi, `hep-ph/9610337`.

[302] U. Ellwanger, J. F. Gunion, and C. Hugonie, `hep-ph/0111179`.

[303] G. Azuelos *et. al.*, `hep-ph/0204031`.

[304] U. Ellwanger, J. F. Gunion, C. Hugonie, and S. Moretti, `hep-ph/0305109`.

[305] G. Weiglein *et. al.*,, **LHC/LC Study Group** Collaboration *Phys. Rept.* **426** (2006) 47–358, [hep-ph/0410364].

[306] S. Moretti, S. Munir, and P. Poulose, *Phys. Lett.* **B644** (2007) 241–247, [hep-ph/0608233].

[307] M. Carena, T. Han, G.-Y. Huang, and C. E. M. Wagner, arXiv:0712.2466 [hep-ph].

[308] S. Baffioni, talk presented at "GdR Supersymétrie 2004", 5–7 July 2004, Clermont-Ferrand, France.

[309] *ATLAS detector and physics performance Technical Design Report*. CERN, Geneva, 1999.

[310] M. Schumacher, hep-ph/0410112.

[311] K. Cranmer, B. Mellado, W. Quayle, and S. L. Wu, hep-ph/0401088.

[312] J. Cammin and M. Schumacher, Tech. Rep. ATL-PHYS-2003-024.

[313] T. M. Trefzger and K. Jakobs, Tech. Rep. ATL-PHYS-2000-015.

[314] J. Thomas, Tech. Rep. ATL-PHYS-2003-003.

[315] D. Cavalli and G. Negri, Tech. Rep. ATL-PHYS-2003-009.

[316] S. González, E. Ros, and M. A. Vos, Tech. Rep. ATL-PHYS-2002-021.

[317] D. Cavalli and P. Bosatelli, Tech. Rep. ATL-PHYS-2000-001.

[318] K. A. Assamagan, Y. Coadou, and A. Deandrea, *Eur. Phys. J. direct* **C4** (2002) 9.

[319] C. Biscarat and M. Dosil, Tech. Rep. ATL-PHYS-2003-038.

[320] D. J. Miller, R. Nevzorov, and P. M. Zerwas, *Nucl. Phys.* **B681** (2004) 3–30.

[321] W. A. Rolke and A. M. Lopez, physics/0606006.

[322] E. Gross,. Several talks. Source code can be obtained from M. Schumacher.

[323] E. Accomando *et. al.*, hep-ph/0608079.

[324] R. Dermisek and J. F. Gunion, *Phys. Rev. Lett.* **95** (2005) 041801, [hep-ph/0502105].

[325] M. S. Carena, J. R. Ellis, S. Mrenna, A. Pilaftsis, and C. E. M. Wagner, *Nucl. Phys.* **B659** (2003) 145–178, [hep-ph/0211467].

[326] B. A. Dobrescu, G. L. Landsberg, and K. T. Matchev, *Phys. Rev.* **D63** (2001) 075003, [hep-ph/0005308].

[327] J. M. Gerard and M. Herquet, *Phys. Rev. Lett.* **98** (2007) 251802, [hep-ph/0703051].

[328] M. Krawczyk, hep-ph/0103223.

[329] T. Stelzer, S. Wiesenfeldt, and S. Willenbrock, *Phys. Rev.* **D75** (2007) 077701, [hep-ph/0611242].

[330] K. Cheung, J. Song, and Q.-S. Yan, *Phys. Rev. Lett.* **99** (2007) 031801, [hep-ph/0703149].

[331] T. Plehn, D. L. Rainwater, and D. Zeppenfeld, *Phys. Lett.* **B454** (1999) 297–303, [hep-ph/9902434].

[332] D. Cavalli *et. al.*, `hep-ph/0203056`.

[333] M. Klute, *ATLAS Note* **ATL-PHYS-2002-018** (2002).

[334] S. Gleyzer and H. Prosper, *See: http://cern.ch/sergei/paradigm.pdf for details* (2007).

[335] J. Freund, *Prentice-Hall, Englewood Cliffs, New Jersey* (1984) 289.